ACTUATOR SELECTION AND PLACEMENT FOR LINEAR FEEDBACK CONTROL OF COMPRESSIBLE FLOWS

BY

MAHESH NATARAJAN

DISSERTATION

Submitted in partial fulfillment of the requirements
for the degree of Doctor of Philosophy in Aerospace Engineering
in the Graduate College of the
University of Illinois at Urbana-Champaign, 2017

Urbana, Illinois

Doctoral Committee:

Associate Professor Daniel J. Bodony, Chair and Director of Research
Professor Jonathan B. Freund, Co-Chair and Co-Director of Research
Professor J. Craig Dutton
Assistant Professor Kai James

Abstract

Actuator and sensor placement for active control of high-Reynolds number flows is largely based on experience and trial-and-error because of the system's large dimensionality and complexity. A novel strategy for estimating how to select and place a linear feedback control system using co-located actuator(s)/sensor(s) suitable for affecting the dynamics of compressible, viscous flows is developed. The methodology uses the flow's gain and receptivity information from the forward and adjoint global modes of the baseflow obtained from direct/large eddy simulations. The baseflow can be an equilibrium (steady-state) or a time-averaged solution of the compressible Navier-Stokes equations. The method uses structural sensitivity arguments to determine regions of the flow-field with high dynamical sensitivity, and a search procedure determines effective actuator/sensor locations. The control algorithm is flexible, and different types of control and feedback can be considered. The efficacy of the method is demonstrated with three different flow control problems: flow stabilization in a Mach 0.65 diffuser, noise reduction of an axisymmetric Mach 1.5 jet, and noise reduction of a turbulent Mach 0.9 jet. For the diffuser, global stabilization is achieved for low Reynolds numbers resulting in complete suppression of vortex shedding. For longer domains and higher Reynolds number flows in the diffuser, although significant reduction in growth rates of the unstable modes was achieved, complete stabilization could not be attained. For the axisymmetric Mach 1.5 jet, equilibrium and time-averaged configurations are compared to examine the differences in global stability. The jet's optimal transient response that leads to the largest pressure fluctuations away from the jet is used to relate the global modes needed for the control methodology to the radiated sound. The spectrum also contains modes that are hydrodynamically bound to the jet, without significant sound field contributions. Direct numerical simulations using the control show significant noise reduction, with additional reduction with increase in control gain. Eigenanalysis of the controlled mean flows reveal fundamental changes in the spectrum at frequencies lower than that used by the control, with the quieter flows having unstable eigenvalues that correspond to eigenfunctions without significant support in the acoustic field. Analysis of the mean flow quantities shows that the control-induced mean flow changes only become obvious beyond 15 radii from the nozzle. Reduced order analysis using Proper Orthogonal Decomposition (POD) shows flow regularization in the quieter flows. The active

control strategy is then applied to a Mach 0.9 turbulent jet. The global analysis of the time-and-azimuthal averaged baseline flow showed that the flow supports acoustically efficient super-directive and multi-directive global modes. Significant noise reduction was obtained and, similar to the axisymmetric case, the global analysis of the time-and-azimuthal averaged flow for the quiet jet show the existence of an unstable mode at a low Strouhal number, that lacks any significant sound-field support. The variation of mean quantities at the centerline and the lipline for the loud and quiet jets also showed trends similar to the axisymmetric case.

To Amma and Appa

Acknowledgements

I express my heartfelt gratitude to my advisors, Professor Daniel Bodony and Professor Jonathan Freund, for their support and patience in guiding me over the years. Their insightful comments and suggestions have been extremely valuable in the completion of this work, and in my growth as a researcher. Their courses on Aeroacoustics and Inviscid Flow have also been very helpful in my graduate studies. I am extremely grateful to Professor J Craig Dutton and Professor Kai James for being part of my defense committee. I would also like to thank Professor Joanna Austin, who served on my preliminary examination committee.

This work was supported by the Rolls-Royce (North America) Corporation with Dr. Jack Sokhey as the program manager and the Office of Naval Research, with technical monitors Dr. Joseph Doychak and Dr. Knox Millsaps. Support from Dr. Brenda Henderson, deputy manager for the Jet Noise Reduction project, is also gratefully acknowledged. Computational support has been provided by the National Science Foundation, through TeraGrid and XSEDE resources, under grant TG-CTS090004.

Special thanks to all my colleagues – Mahesh Sucheendran, Christopher Ostoich, Jeonglae Kim, Qi Zhang, Nishan Jain, Ashish Mishra, Revathi Jambunathan, Nek Sharan, Wentao Zhang, Shakti Saurabh, Ramanathan Vishnampet, Jaeseung Byun, Fabian Dettenrieder, Cory Mikida, Bryson Sullivan, Shreyas Bidadi, Nishanth Lingala, Sushilkumar Koundinyan, Jyothi Sadhu, Amal Sahai and Mohammad Mehrabadi – I have learned a lot from you all.

Big thanks to my first friends in Urbana-Champaign – Ravi Tumkur and Praveen Nakshatrala, for all the fun times they spent with me on dinners, movies and at the ARC. Later, in 2011-2013, common interests in food, movies and Cricket earned me some really good friends here. Cricket matches at the engineering quad and the south quad were real fun and will never forget them. My sincere thanks to Nishanth, Sushil, Jyothi, Sohan, Gokul (Jerusalem food (thanks, Hameed!) and chats, Aurora and Chicago trips!), Purusho, Vishal, Krishna, and all the random players who made the fun times possible.

2014 – I meet the American Junction. Since then, I seldom missed an opportunity that I got to hangout with them. The fun-filled gatherings for tea, birthdays, anniversaries and festivals, will be terribly missed. They have treated me with really good food umpteen times, and I have always felt at home whenever

I visited them. I would like to express my heartfelt gratitude to Maneesha and Sandeep, Rachana and Kishor, Sandhya and Santhosh, Raghavi and Madhu, Sangeetha, Kini, Sinduja, Krishna, Anjali, Koshy, Suraj, Jacob, Manu, Sarath, Sebastian and Anand. The badminton games at the ARC with Sarath, Daman, Kishor, Madhu, Santhosh and Anand were real fun and much needed stress busters which helped me rewind myself from the stress of academics. The city of Bloomington became an indispensable part of our life here, with frequent trips to enjoy good South Indian food (special thanks to Mayuri (Signature India)), watch Tamil and Hindi movies (thanks Sushil and Daman), and once in a while movie screening by our Malayali friends (Jishnuram, Anoop and others – thanks a ton!) there. Good movies have compelled us to drive to Chicago a few times, and each of those one day trips were total fun, and I really hope I get to do that some day, again! The Onam and Christmas celebrations of the Champaign-Urbana Malayali Association, with good food, cultural programmes and games were really memorable – thanks to Vipin Raj, Bobby, Paul, Bijoy, and others, for their sincere efforts.

Finally, I would like to thank the most important people in my life – my parents and my brother, for their unconditional love and support, and for everything they have done for me.

Table of Contents

List of Figures

Chapter 1

Introduction

Flow control is a rapidly evolving and active field of research that can have significant impact on aircraft performance (by drag minimization, lift increase, mixing enhancement in combustors) and attractiveness (by making them sufficiently quiet to satisfy regulations). Passive and active flow control strategies have been developed and improved for a variety of flows. But developing efficient flow control strategies is not straightforward. Rigorous testing of the strategies is iterative and involves labor and cost-intensive equipment and experiments. Hence, computational tools are attractive for developing strategies for flow control. The present work focusses on the development of an active control strategy for compressible flows.

Two different flow control problems are addressed in this dissertation: (1) flow stabilization in diffusers and (2) noise reduction in compressible jets. Section 1.1 reviews the use of global modes. Section 1.2 summarize the use of adjoint methods for flow control. Numerical methods for large scale eigenvalue problem computation are reviewed in Section 1.3. Section 1.4 and Section 1.5 summarize current understanding and practice of flow control in diffusers and noise reduction in jets. Accomplishments are summarized in Section 1.6, and the structure of the dissertation appears in Section 1.7.

1.1 Review of Global Modes

The term 'global instability analysis' was introduced by Joseph (1966) as a methodology that monitors perturbation energy at all times and establishes bounds on its growth. Chomaz *et al.* (1988) used the term 'global instability' to describe those flows where the disturbance remains at, or propagates upstream and/or downstream, from its point of introduction. The development in time and space of small-amplitude perturbations superposed upon a given flow can be described by the linearized Navier-Stokes, continuity, and energy equations. The forward linearized disturbance equations, $\partial \boldsymbol{Q}'/\partial t = \boldsymbol{L}\boldsymbol{Q}'$, using the global mode assumption $\boldsymbol{Q}' \equiv \widehat{\boldsymbol{Q}} e^{\omega t}$ gives rise to the eigenvalue problem (EVP) $\boldsymbol{L}\widehat{\boldsymbol{Q}} = \omega \widehat{\boldsymbol{Q}}$, where $\boldsymbol{L}$ is the linearized Navier-Stokes operator. The solution of this EVP permits identification of global instability characteristics of eigenmodes of a given basic state, such as temporal amplification rates and their frequency spatial structure.

A recent article by Theofilis (2011) reviews extensively global linear instability. As mentioned earlier the term global instability analysis was introduced by Joseph (1966); it was used by Homsy (1973) and Reddy & Voyé (1988) for 1D basic flows. A more general global instability approach evolved during the 1980s towards the analysis of two-dimensional basic states. Two and three dimensional instabilities of a spatially periodic shear layer were studied by Pierrehumbert & Widnall (1982). Eriksson & Rizzi (1985) introduced time-stepping and spectral transformation to the stability analysis of inhomogeneous steady and time-periodic flows. Pierrehumbert (1986) investigated short-wavelength elliptic instability in inviscid vortex flows. The first viscous global analysis were reported by Jackson (1987) and Zebib (1987), who studied the instability of flow around a cylinder.

The distinction between convective and absolute (global) fluid dynamic instabilities was discussed by Briggs (1964). Huerre & Monkewitz (1990) further discussed this approach for the hydrodynamic stability theory of spatially developing flows pertaining to local and global instability concepts. They suggested the concept of a self-excited, low-amplitude "wavemaker" region based on local instability, that acts as a source for the downstream instability waves for spatially developing flows according to the Ginzburg-Landau model. Using a Ginzburg-Landau model, Chomaz *et al.* (1988) showed that self-sustained resonances may appear via a Hopf bifurcation when the system exhibits a region of local absolute instability that is sufficiently large.

In another annual review, Chomaz (2005) assessed stability analysis approaches to understand the dynamics of open flows such as mixing layers, jets, wakes, separation bubbles and boundary layers. He emphasized how the fully global theory accounts for the amplification of noise and the onset of a global mode. Theofilis (2011) introduced the terms BiGlobal and TriGlobal analysis to describe the analysis of 2D and 3D basic states. The first TriGlobal analysis — spheroid at an angle of attack by the solution of 3D EVP — was done by Tezuka & Suzuki (2006). Brès & Colonius (2008) investigated the three dimensional instabilities in compressible cavity flows for a range of conditions and cavity aspect ratios. The global stability of a jet in cross-flow by Bagheri *et al.* (2009) constituted the first simulation-based global stability analysis of a fully three-dimensional base flow. Rodríguez Álvarez & Theofilis (2010) studied the structural changes in laminar separation bubbles in which the composite flow fields were reconstructed by linear superposition of a two-dimensional boundary layer flow with an embedded laminar separation bubble and its leading three-dimensional global eigenmodes.

1.2 Adjoint-based Methods for Control

An obvious desire of flow control is to actuate a flow where the flow is most sensitive, or receptive, to small disturbances. The solution of the adjoint problem $\boldsymbol{L}^\dagger\widehat{\boldsymbol{Q}^\dagger} = \omega\widehat{\boldsymbol{Q}^\dagger}$ provides information of the spatial location of maximum receptivity of the system (Schmid & Henningson (2000)). However, the location of maximum receptivity does not necessarily imply that the flow control will be effective. Adjoint-based methods that involve a spatial overlap of the forward and adjoint global modes of the system have been used to obtain the optimal location of control. Giannetti & Luchini (2007) defined a "wavemaker" region, defined as the part of the domain $\mathcal{D}$ where $\zeta(x,y) \equiv \frac{||\widehat{\boldsymbol{Q}}(x,y)||\ ||\widehat{\boldsymbol{Q}^\dagger}(x,y)||}{\int_{\mathcal{D}} \widehat{\boldsymbol{Q}}\cdot\widehat{\boldsymbol{Q}}^\dagger\, d\mathcal{S}}$ has a large magnitude, given a global mode $\widehat{\boldsymbol{Q}}$ and adjoint mode $\widehat{\boldsymbol{Q}^\dagger}$ to show that, in this region, a change in the linearized operator $\boldsymbol{L}$ creates the largest possible change in the corresponding eigenvalue ω. The wavemaker region indicates a region of high dynamical sensitivity (Chomaz (2005)), where an actuator could have powerful influence on the flow, and localized feedback may be effective. Research in global mode-based flow control has been done for incompressible and compressible regimes as discussed in the following sections.

Adjoint-based methods for flow control were used by Hill (1992) to suppress the vortex shedding from a cylinder by placing a small cylinder in the wake of a larger one. Giannetti & Luchini (2007) used both direct and adjoint global modes of an incompressible flow past a cylinder near the critical Reynolds numbers to identify the spatial regions of the flow most sensitive to momentum forcing and mass injection. The analysis showed that the maximum of the perturbation envelope amplitude was reached downstream of the separation bubble, but the highest receptivity was attained in the near wake of the cylinder, close to the cylinder. The large difference between the spatial structure of the direct and adjoint modes suggested that the instability mechanism cannot be identified from the study of either eigenfunctions separately. Giannetti *et al.* (2010) subsequently investigated the sensitivity of the three-dimensional secondary instability of a circular-cylinder wake by identifying the region of maximum coupling between the velocity components was localized by using the most unstable Floquet mode and its adjoint mode. Henningson & Åkervik (2008) used global modes to perform flow control for two-dimensional disturbances in the Blasius boundary layer and a globally unstable boundary-layer flow along a shallow cavity. The global modes of the system were shown to be a good starting point for reduced order models to control growing disturbances. Marquet *et al.* (2008) used adjoint-based methods to study the sensitivity analysis of the unstable eigenmode responsible for vortex shedding from a cylinder. They demonstrated how this can be used to identify regions of the baseflow that contribute to the onset of vortex shedding. Chen & Rowley (2011) developed an H_2 optimal controller for the control of a supercritical, infinite-domain formulation of a system based on the linearized

complex Ginzburg-Landau equation (which is a model for the evolution of small fluid perturbations, such as in a bluff body wake). Their optimal results were very close to those given by the "wavemaker" theory, which utilizes the forward and adjoint global modes of a system for optimal actuator placement for their model. Qadri *et al.* (2013) investigated the spiral mode which develops during vortex breakdown with a linear global stability analysis around the steady bubble and its wake. The linear direct and adjoint global modes of the linearized Navier-Stokes equations were overlapped to obtain the structural sensitivity of the spiral mode, which identifies the wavemaker region. The concept of operator structural sensitivity was used by Sipp *et al.* (2010) and applied to a variety of flows.

Relatively less research has been carried out in global instabilities and control of compressible fluids. Much of the research has been devoted to understanding the underlying instability mechanisms and not control. Open-loop control using adjoint based methods for compressible afterbody flows has been investigated by Meliga *et al.* (2010). They evaluated the sensitivity of one particular eigenvalue to forcing by resolution of adjoint equations and showed that the oscillating mode of the baseflow can be stabilized by a steady blowing at the wall – the so-called base-bleed control. Meliga & Chomaz (2011) used adjoint global modes and sensitivity analysis to identify the regions of an impinging jet suitable for different kinds of actuation, and (passive) control of the flow is observed when a small airfoil is placed in the flow in the specific locations identified by the analysis. Nichols & Lele (2011) performed global analysis of a cold supersonic jet and found that in addition to Kelvin-Helmholtz modes, the jet supported upstream-propagating modes that could not be resolved by previous analyses of parabolized stability equations (PSE). Continuous and discrete adjoint methods in the low Mach number regime have been investigated by Chandler *et al.* (2012) for a low-density jet. A low Mach number formulation was used, and they formulated a discrete adjoint method consistent with the continuous adjoint method. The most unstable global mode calculated with the discrete-adjoint had exactly the same eigenvalue as the corresponding forward global mode, but had numerical artifacts near the inlet of the jet. The continuous-adjoint global mode showed no numerical artifacts but had a slightly different eigenvalue.

1.3 Numerical Methods for Global Mode Computation

The computation of forward and adjoint global modes of the linearized Navier-Stokes equations involves solving large eigenvalue problems. The size of the matrix is $(N_g \times N_v)^2$, where N_g is the number of grid points and N_v is the number of variables per grid point. At present, there are open source libraries that can solve such eigenvalue problems. In general, the aim is to recover the part of the eigenspectrum which

contains the most interesting dynamics from a physical point of view — here, the most unstable/least stable global linear eigenmodes. The following two packages are popular among researchers:

- ARPACK (**AR**noldi **PACK**age) by Lehoucq *et al.* (1997)
- SLEPc (**S**calable **L**ibrary for **E**igenvalue **P**roblem **C**omputation) by Hernandez *et al.* (2005)

Eigenvalue algorithms like the Arnoldi method and its variants (Hernandez *et al.* (2007)) are widely used. ARPACK uses the IRAM (Implicitly Restarted Arnoldi Method) but presents implementation challenges. SLEPc, on the other hand, is more coding-friendly and has an implementation of the Krylov-Schur method, which is IRAM with a very effective restarting technique. The computation of eigenvalues involves solving linear systems of equations, using either direct solvers or iterative ones with Krylov subspace methods like GMRES with preconditioners. Using an iterative linear solver makes the overall solution process less robust but permits larger problem sizes. Direct solvers that involve an LU factorization are more accurate, and the factorization needs to be done just once. MUMPS (**MU**ltifrontal **M**assively **P**arallel **S**olver (Amestoy *et al.* (2001)) is an open source package capable of LU factorization of large sparse matrices.

1.4 Flow Control in Diffusers

Curved subsonic diffusers are a common feature in tactical aircraft where it is advantageous to bury the engine within the airframe to hide it from exterior view. One consequence of this approach is that the large duct curvature and the adverse pressure gradient felt by the incoming boundary layers lead to unwanted flow conditions caused by massive separation that induce performance loss (drag increase and total pressure loss to the engine) and unsteady loads on the engine fan. Improving the flow quality at the engine fan face through flow control enables more aggressive S-duct designs that may yield enhanced aircraft performance.

Previous experimental studies have shown that large adverse pressure gradients in a diffuser cause flow separation. Reneau *et al.* (1967) categorized stall regimes for a planar diffuser geometry. Experimental studies have shown that the control of the large scale vortex shedding can significantly improve the pressure recovery in diffusers. For example, Rao (1971) used radial splitter vanes in conical diffusers to obtain a steady exit flow in the diffuser. Steady mass injection using vortex generator jets was employed in conical diffusers by Nishi *et al.* (1998) and Nicoll & Ramaprian (1970). Control was achieved in wide angled conical diffusers using a star-tail pipe by Welsh (1976). Tennant (1973) used rotating cylinders to provide moving walls for separation control. Active feedback control was used by Kwong & Dowling (1994), in which the air supplied through the wall jets is modulated in response to the unsteady pressures within the diffuser. Seifert *et al.* (1996) carried out experiments using periodic mass injection for airfoil stall delay. They found that

the control flow depends on many parameters, such as the location of the blowing slot and the frequency of imposed oscillations. Separation control in a two-dimensional serpentine duct was obtained by Amitay *et al.* (2002) using an array of synthetic jets. Experiments using multiple frequency excitation to affect the formation and interaction of large-scale vortices was used by Narayanan & Banaszuk (2003) for separation control in planar diffuser geometries. Suzuki *et al.* (2004) developed a reduced-order model for large-scale unsteadiness in a two-dimensional diffuser to show how periodic mass injection near the separation point reduces stagnation pressure loss.

1.5 Noise Reduction in Compressible Jets

Noise levels in tactical jet aircraft have increased as the jet exit velocity and airflow from these engines have increased to produce added thrust. Their noise levels can exceed 150 dB, which can lead to hearing loss, and which are beyond the ability of currently-available hearing protection to attenuate the noise to safe levels (Bowes *et al.*, 2009). Noise reduction is also a major concern for the design of supersonic commercial aircraft. Supersonic aircraft are typically powered by low-bypass turbofan engines so that noise reduction techniques used in high-bypass subsonic commercial aircraft are not useful. Higher exit velocities and the presence of shock cells in low-bypass engine exhausts cause jet noise to be the dominant component of the overall aircraft noise.

Since the 1960s, there has been a continuous effort to describe the dynamics of far-field jet noise using linear instability theory. The current thinking is that the noise producing modes identified using linear analyses are, in general, best characterized as wavepackets, which are intermittent, advecting disturbances correlated over distances that exceed the integral scales of turbulence. The earliest work that detected wavepacket behavior in the acoustic fields of jets was by Mollo-Christensen (1963, 1967), who identified long correlation distances for the large eddies in a turbulent jet and attempted to reconstruct the pressure fluctuations with a model emitter, using simple functions which had similar behavior. Large-scale, coherent structures were observed by Crow & Champagne (1971) for an incompressible turbulent jet. Similar large-scale structures, which advect at nearly constant speed were identified in plane turbulent mixing layers by Brown *et al.* (1974). Experiments on low-Reynolds-number axisymmetric supersonic jets by McLaughlin *et al.* (1975) showed that acoustic radiation generated by the dominant instability was primarily due to Mach waves. Moore (1977) found that a significant increase in jet noise can be produced by low amplitude shear layer instability excitation at the nozzle at the correct Strouhal number. The acoustic measurements of Morrison & McLaughlin (1979) and Troutt & McLaughlin (1982) showed that the major portion of the

sound radiated by low Reynolds number supersonic jets was produced by the saturation and disintegration of the large-scale instability that occurs near the end of the potential core. Experiments on low-Mach-number jets by Laufer & Yen (1983) showed that acoustic sources were associated with the nonlinear saturation of the unstable wave amplitudes of the shear layer occurring at the vortex-pairing locations. The modal distributions of coherent structures in the near-nozzle region of an axisymmetric jet were investigated by Cohen & Wygnanski (1987), and a linear model was developed to predict the spectral distribution of the jet velocity perturbations.

There were considerable theoretical efforts to describe noise generation in supersonic jets using instability wave theory. Tam (1971) developed a theory based on instabilities of the shear layer at the boundary of the jet close to the nozzle. Crighton & Gaster (1976) modelled coherent axisymmetric structures in a turbulent jet as linear instability modes of the mean velocity profile. Michalke (1984) reviewed the theoretical results for jet instability of axisymmetric jets including effects of nozzle-jet interactions. A mathematical model for tone-excited jets was developed by Tam & Morris (1985), who described the excitation of the intrinsic jet instabilities by the upstream tones and their interaction with the jet mean flow. The effects of these instabilities on the broadband noise were also discussed. Tam & Hu (1989) analytically identified three families of instability waves in high-speed jets, which had been experimentally observed by Oertel (1979). Tam & Chen (1994) extended the instability wave solution of Tam & Burton (1984) and developed a stochastic instability wave theory for turbulent mixing noise of supersonic jets. More recently, Goldstein & Leib (2005) solved the relevant acoustic equations for a weakly non-parallel mean flow and demonstrated that linear instability waves must be accounted for in order to construct a proper causal solution to the jet noise problem. Other recent efforts in instability related noise generation include that by Samanta & Freund (2008) in which a model was developed using the Wiener-Hopf method for the scattering of vortical disturbances into upstream propagating acoustic modes at a shrouded-jet exit. Samanta & Freund (2015) used a similar approach to quantify the far-field directivity to evaluate the acoustic efficiency of different instability modes in a similar configuration.

Until the late 1990s, experiments were the major benchmark for confirming instability based jet noise theories. Later, direct numerical simulations came into prominence enabling precise predictions of jet noise. The sound field of a perfectly expanded, Mach 1.92 turbulent jet was computed by Freund *et al.* (2000) and mechanisms of noise generation in a low Reynolds number Mach 0.9 jet were investigated by Freund (2001). Bodony & Lele (2005) used large eddy simulations to predict jet noise from cold and heated turbulent jets. Detailed reviews of both approaches in the context of jet noise are presented by Wang *et al.* (2006) and Bodony & Lele (2008). Early attempts in computing the acoustic characteristics of instability waves include

those by Balakumar (1998) and Yen & Messersmith (1999), in which Parabolized Stability Equations (PSE) were used to compute the instability waves inside the jet and computed the far-field noise radiated from these jets. Linear and nonlinear evolution of disturbances in an axisymmetric, supersonic, low Reynolds number jet were studied using the PSE method by Malik & Chang (2000), and good agreement was obtained with the experimental data of Morrison & McLaughlin (1980). Piot *et al.* (2006) also used the PSE method for supersonic axisymmetric jets and obtained good agreement for the levels of acoustic radiation with those from large eddy simulations. Cheung *et al.* (2007) used a hybrid nonlinear PSE-acoustic analogy approach and found that the method can capture the near-field hydrodynamics and the far-field acoustic radiation for supersonic jets. Cheung & Lele (2009) used the PSE method to examine the effects of heating on two-dimensional compressible mixing layers. Pressure fluctuations associated with large-scale structures are modeled with the PSE method by Gudmundsson & Colonius (2009) for linear disturbances on heated and unheated turbulent mean flows. This technique was extended by Sinha *et al.* (2014), in conjunction with Proper Orthogonal Decomposition (POD) of the turbulent mean flow for prediction of far-field jet noise, and the results suggested that linear wavepackets are responsible for the loudest portion of the acoustic field. Cavalieri *et al.* (2011) modelled the sound field from direct numerical simulations using simplified wavepacket models. PSE analysis has also been used to educe wavepackets in the velocity fields of high Reynolds number, subsonic jets from time-resolved PIV measurements by Cavalieri *et al.* (2013).

For control, prior noise reduction work has been entirely experience-based. The most successful noise reduction strategies to date are chevrons or vortex generators (Samimy *et al.*, 1993) for passive control and arc filament actuators (Samimy *et al.*, 2007) for active control. Computationally, adjoint-based methods have shown good promise in controlling far-field noise. Wei & Freund (2006) used an adjoint-based optimization procedure and achieved 11 dB noise reduction of far-field sound with internal energy control for a two-dimensional compressible shear layer. Using a similar approach, Kim *et al.* (2014) obtained a reduction of ≈ 3.5 dB for a Mach 1.3 turbulent jet. The suggested mechanism of control in their simulations was the disruption of the coherence of acoustically efficient axisymmetric flow structures. Vishnampet *et al.* (2015) demonstrated a discrete-adjoint based optimization procedure for aeroacoustic control of a turbulent mixing layer. They showed that the continuous-adjoint suffers exponential error growth in (reverse) time and hence could potentially affect the noise reduction obtained in past efforts. In the context of the wavepacket-based description of jet noise, Jordan & Colonius (2013) reviewed the literature on wavepacket modelling of jet noise using PSE, POD and global modes. The global modes are more reliable than PSE analysis as they do not invoke any approximations of the flow field. Nichols & Lele (2011) used the global mode analysis to obtain the optimal transient response of a cold, supersonic jet and identified upstream-propagating modes

which could not be resolved by the earlier PSE analyses. However, there have not been efforts directed towards utilizing the information in the linear wavepackets, in the context of global modes, for developing strategies for active jet noise control.

1.6 Contributions

The main contributions of this dissertation are the following:

1. A novel active control strategy based on global linear modes has been developed for designing effective co-located actuator(s)/sensor(s) for linear feedback control of compressible flows. The developed methodology is generic and flexible. It can be used to determine effective actuator(s)/sensors(s) for any combination of control and feedback variables.

2. The control strategy was successfully applied to stabilize a low Reynolds number separated boundary layer in a Mach 0.65 diffuser. In certain cases, it was shown that the developed controller could attain complete global stabilization and complete suppression of vortex shedding. For higher Reynolds numbers and longer domains, although complete stabilization could not be attained, significant reduction in the growth rate ($\sim 50\%$) of the most unstable eigenvalue was observed.

3. The flow control strategy was successful in determining effective controllers for noise reduction in an axisymmetric Mach 1.5 jet and a turbulent Mach 0.9 jet. For the axisymmetric jet, at the target surface at $r/R = 15$, a maximum reduction of ~ 4.5 dB was obtained at an angle of $\approx 30^0$, and for the turbulent jet, at the target surface at $r/D = 7$, a consistent reduction of 3-4 dB was obtained for all angles $> 40^0$, with a maximum reduction of approximately 4 dB at 90^0.

4. In both the Mach 1.5 and Mach 0.9 jet noise reduction studies, the control action destabilized a very low frequency global mode whose dynamical importance grew relative to the uncontrolled jet. Such a mode does not appear to have been studied before and its importance to jet noise reduction warrants future investigation.

1.7 Dissertation Structure

The thesis is organized as follows:

- *Chapter 2* describes the elements of the active control strategy we employ from a general point of view. Flowcharts of the flow control procedure are provided and a general formulation is described.

- *Chapter 3* addresses flow stabilization of a separated boundary layer in a Mach 0.65 diffuser. The governing equations and the formulation of the global eigenvalue problem in generalized coordinates is described, and different test cases for the verification of the eigenvalue solver are detailed. The details of the steady baseflow, control development, controlled simulations and analysis are presented.

- *Chapter 4* addresses noise reduction of an axisymmetric Mach 1.5 jet. The governing equations and numerical methods are discussed, and the flow solutions (equilibrium and time-averaged) and their eigenanalysis are presented. The control development, results and analysis of noise controlled flows are described in detail.

- *Chapter 5* is devoted to noise reduction of a Mach 0.9 turbulent jet. The flow conditions and details of the LES numerics for the baseflow computation are presented. The eigenanalysis of the baseline flow, control development, results and analysis of controlled simulations are given in detail.

- *Chapter 6* discusses the conclusions and the shortcomings of the current strategy, and directions are provided to overcome them.

- *Appendices A-G* provide derivation of the linearized equations, test cases for verification, and details of the numerical methods.

Chapter 2

Flow Control Formulation

The simulation-based control approach has the five basic elements shown in Fig. 2.1. First, the to-be-improved baseline flow is computed using direct numerical simulations, large eddy simulations, RANS etc. We define a control objective (reduction of noise, drag, stagnation pressure loss) and a linear feedback control strategy informed by structural sensitivity analysis is developed. Simulations are performed using the control to assess its performance, and the baseline and controlled flows are analyzed to identify possible mechanisms of control using flow visualization and other linear and non-linear methods of analysis.

In the present work, we focus on active flow control of compressible flows. The two major questions posed by an active flow control strategy are: (1) where to sense and where to control? and (2) what to sense and what to control?. We utilize the global (temporal) modes of the flow-field to answer the questions posed in (1) and (2).

The general control strategy is described in this chapter. The detailed formulation specific to the governing equations employed are described in Chapter 3 (generalized coordinates) and Chapter 4 (axisymmetric coordinates).

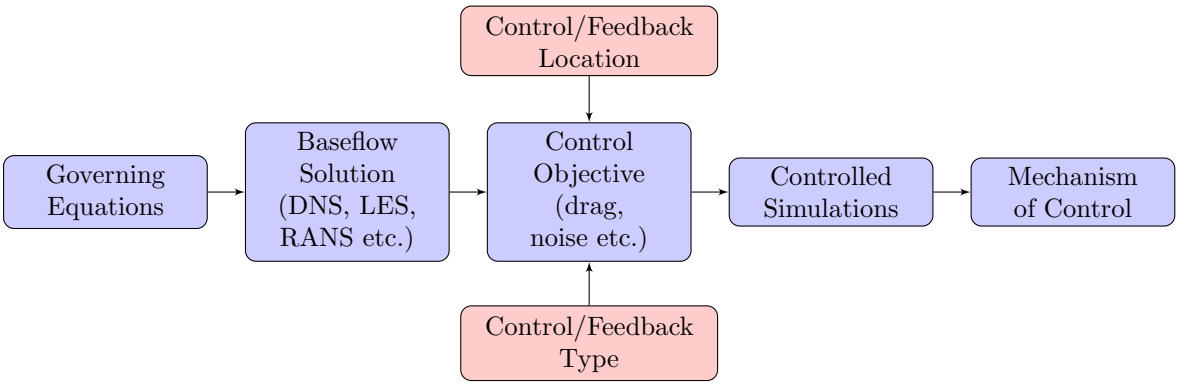

Figure 2.1: Basic flowchart of an active flow control strategy.

2.1 Baseflow Solution

In general, the discretized flow equations are written as

$$\frac{\mathrm{d}\boldsymbol{Q}}{\mathrm{d}t} = \tilde{\boldsymbol{R}}(\boldsymbol{Q}), \tag{2.1}$$

where $\boldsymbol{Q}$ is the vector of unknowns and $\tilde{\boldsymbol{R}}$ is the discretized right hand side, including all boundary conditions. Details of $\tilde{\boldsymbol{R}}$ are given in Chapters 3 and 4. Two types of baseflow solutions can be used to perform the eigenanalysis – a true equilibrium flow ($\tilde{\boldsymbol{R}}(\boldsymbol{Q}) \to 0$) and a time-average solution. For globally unstable equilibrium solutions, the method of Selective Frequency Damping (Åkervik *et al.* (2006)) may be used to numerically converge on the baseflow. This involves adding a dissipative relaxation term proportional to the high-frequency content of the fluctuations of the corresponding variable being solved for to the right hand side of the NS equations,

$$\begin{aligned} \frac{d\boldsymbol{Q}}{dt} &= \tilde{\boldsymbol{R}}(\boldsymbol{Q}) - \chi(\boldsymbol{Q} - \bar{\boldsymbol{Q}}) \\ \frac{d\bar{\boldsymbol{Q}}}{dt} &= (\boldsymbol{Q} - \bar{\boldsymbol{Q}})/\Delta, \end{aligned}$$

where $\bar{\boldsymbol{Q}}$ is the temporally filtered solution. The filter width (Δ) and gain (χ) are parameters to be chosen. The equations are simultaneously advanced in time and a judicious choice of the parameters χ and Δ will force the solution ($\boldsymbol{Q}$) and the filtered solution ($\bar{\boldsymbol{Q}}$) to a steady state solution of the Navier-Stokes equations. As $\boldsymbol{Q} \to \bar{\boldsymbol{Q}}$, $\tilde{\boldsymbol{R}}(\boldsymbol{Q}) \to 0$. The cut-off frequency $\omega_c = 1/\Delta$ should be less than the lowest frequency of instabilities at which the growth rate is expected and $\chi \approx$ twice the growth rate of the dominant disturbance (Åkervik *et al.* (2006)). An eigenanalysis of the unsteady flow can be used to estimate the values of the SFD parameters, χ and Δ.

2.2 Global Eigenvalue Problem

2.2.1 Flow Equations

Linearization of (2.1) for small perturbation $\boldsymbol{Q}'$ to baseflow $\bar{\boldsymbol{Q}}$ yields

$$\frac{\mathrm{d}\boldsymbol{Q}'}{\mathrm{d}t} = \boldsymbol{L}(\bar{\boldsymbol{Q}})\boldsymbol{Q}', \tag{2.2}$$

where $\boldsymbol{L}$ is the discrete right hand side operator evaluated about the baseflow $\bar{\boldsymbol{Q}}$. The eigenvalue problem we consider is based on a modal decomposition of the form

$$\boldsymbol{Q}'(\boldsymbol{x},t) = \widehat{\boldsymbol{Q}}(\boldsymbol{x})e^{\omega t}, \tag{2.3}$$

where m is the azimuthal mode number, ω is the eigenvalue and $\widehat{\boldsymbol{Q}}$ is the eigenmode. In general the equations lead to a generalized eigenvalue problem

$$\boldsymbol{L}\widehat{\boldsymbol{Q}} = \omega \boldsymbol{M}\widehat{\boldsymbol{Q}}. \tag{2.4}$$

The matrix $\boldsymbol{M}$ is diagonal but not invertible.

2.2.2 Adjoint Eigenvalue Problem

We have the forward eigenvalue problem given by (2.4)

$$\omega \boldsymbol{M}\widehat{\boldsymbol{Q}} = \boldsymbol{L}(\bar{\boldsymbol{Q}})\widehat{\boldsymbol{Q}},$$

where $\boldsymbol{L}(\bar{\boldsymbol{Q}})$ is the linearized Navier-Stokes operator. The discrete adjoint formulation of Giannetti & Luchini (2007) considers the left eigenvectors of $\boldsymbol{L}(\bar{\boldsymbol{Q}})$ as the adjoint eigenmodes of the system, which is inconsistent since it does not take into account the definition of the inner product to define the adjoint system for the Navier-Stokes equations. We use the volume correction formulation as in Chandler *et al.* (2012), which is consistent with the formulation of the continuous adjoint problem. The inner product is defined as

$$\langle \widehat{\boldsymbol{Q}^\dagger}, \widehat{\boldsymbol{Q}} \rangle = \frac{1}{\mathcal{V}} \oint_{\mathcal{V}} \widehat{\boldsymbol{Q}^\dagger}^H \widehat{\boldsymbol{Q}} \, \mathrm{d}\mathcal{V},$$

where $\mathcal{V}$ is the volume of the domain. $\widehat{\boldsymbol{Q}^\dagger}^H \widehat{\boldsymbol{Q}} = \sum_i \widehat{\boldsymbol{Q}^\dagger}_i^* \widehat{\boldsymbol{Q}}_i$ where '*' denotes the complex conjugate and where the superscript 'H' denotes a complex conjugate transpose. Using this definition of the inner product, we have

$$\oint_{\mathcal{V}} \widehat{\boldsymbol{Q}^\dagger}^H \omega \boldsymbol{M}\widehat{\boldsymbol{Q}} \, \mathrm{d}\mathcal{V} = \oint_{\mathcal{V}} \widehat{\boldsymbol{Q}^\dagger}^H \boldsymbol{L}(\bar{\boldsymbol{Q}})\widehat{\boldsymbol{Q}} \, \mathrm{d}\mathcal{V} \tag{2.5}$$

Discretization of (2.5) using the trapezoidal rule gives

$$\widehat{\boldsymbol{Q}^\dagger}^H \omega \boldsymbol{M}\boldsymbol{D}\widehat{\boldsymbol{Q}} = \widehat{\boldsymbol{Q}^\dagger}^H \boldsymbol{D}\boldsymbol{L}\widehat{\boldsymbol{Q}}, \tag{2.6}$$

where $\boldsymbol{D} = \mathrm{diag}(v_1/V, v_2/V, \ldots, v_n/V)$ is a diagonal matrix in which V is the volume of the domain, and v_i is the volume associated with the i^{th} grid point. (2.6) can be rearranged to give

$$(\omega^* \boldsymbol{M}\boldsymbol{D}\widehat{\boldsymbol{Q}^\dagger})^H \widehat{\boldsymbol{Q}} = (\boldsymbol{L}^H \boldsymbol{D}^H \widehat{\boldsymbol{Q}^\dagger})^H \widehat{\boldsymbol{Q}}.$$

Since the above is true for arbitrary $\widehat{\boldsymbol{Q}}$, we obtain the discrete adjoint eigenvalue problem as

$$\omega^* \boldsymbol{M}\boldsymbol{D}\widehat{\boldsymbol{Q}^\dagger} \quad = \quad \boldsymbol{L}^H \boldsymbol{D}^H \widehat{\boldsymbol{Q}^\dagger}, \tag{2.7}$$

which can be written as

$$\omega^* \boldsymbol{M}\widehat{\boldsymbol{Q}^\dagger} \quad = \quad \boldsymbol{D}^{-1}\boldsymbol{L}^H \boldsymbol{D}\widehat{\boldsymbol{Q}^\dagger}.$$

Hence, the discrete adjoint matrix can be written as

$$\boldsymbol{L}^\dagger = \boldsymbol{D}^{-1}\boldsymbol{L}^{\mathrm{T}}\boldsymbol{D},$$

since $\boldsymbol{L}$ is a real matrix and, hence, $\boldsymbol{L}^H = \boldsymbol{L}^{\mathrm{T}}$. Since this is a similarity transformation for $\boldsymbol{L}^{\mathrm{T}}$, it can be seen that the eigenspectrum of the forward eigenvalue problem (defined by $(\boldsymbol{L}, \boldsymbol{M})$) and the discrete adjoint eigenvalue problem (defined by $(\boldsymbol{L}^\dagger, \boldsymbol{M})$) are exactly the same whereas the eigenmodes will differ, and therefore, corresponding to every eigenvalue, we obtain a forward-adjoint pair of eigenmodes.

2.2.3 Eigenvalue Solver

The eigenvalue solver addresses the forward and adjoint systems (2.4) and (2.7). The solver uses PETSc (Balay *et al.*, 2012*b*,*a*, 1997) for the matrix construction and SLEPc (Hernandez *et al.*, 2005) to solve the global eigenvalue problem. The Krylov-Schur implementation of the Implicitly Restarted Arnoldi Method (IRAM), in conjunction with the shift-and-invert spectral transformation and MUMPS (Amestoy *et al.*, 2001) for the LU factorization of the linearized Navier-Stokes operator, is used to obtain the eigenvalues that are closest to a specified target in absolute value in the complex plane and the corresponding eigenmodes.

2.2.4 Shift-and-Invert

A spectral transformation is used for computing internal eigenvalues and to obtain accelerated convergence. It transforms the original problem by mapping the eigenvalues to a new position while eigenvectors remain

unchanged. The shift-and-invert spectral transformation is used to accelerate the convergence of eigenvalues in the neighborhood of a given target eigenvalue. Consider the standard eigenvalue problem,

$$\boldsymbol{A}\boldsymbol{x} = \lambda \boldsymbol{x}. \tag{2.8}$$

In the shift-and-invert case, with a target value of ω, the method solves the following eigenvalue problem,

$$(\boldsymbol{A} - \omega \boldsymbol{\mathcal{I}})^{-1}\boldsymbol{x} = \theta \boldsymbol{x} \tag{2.9}$$

where θ denotes the eigenvalues of the shifted operator $(\boldsymbol{A} - \omega\boldsymbol{\mathcal{I}})^{-1}$. The eigenvectors remain unchanged and the relation between the eigenvalues of problems (2.8) and (2.9) is

$$\lambda = \omega + \frac{1}{\theta}. \tag{2.10}$$

2.2.5 Structural Sensitivity Analysis

We have the generalized forward eigenvalue problem given by,

$$\boldsymbol{L}\widehat{\boldsymbol{Q}} = \omega \boldsymbol{M}\widehat{\boldsymbol{Q}}$$

Now, let us perturb the equation with a change of operator given by $\delta\boldsymbol{L}$,

$$(\boldsymbol{L} + \delta\boldsymbol{L})(\widehat{\boldsymbol{Q}} + \delta\widehat{\boldsymbol{Q}}) = (\omega + \delta\omega)\boldsymbol{M}(\widehat{\boldsymbol{Q}} + \delta\widehat{\boldsymbol{Q}})$$
$$\boldsymbol{L}\widehat{\boldsymbol{Q}} + \boldsymbol{L}\delta\widehat{\boldsymbol{Q}} + \delta\boldsymbol{L}\widehat{\boldsymbol{Q}} + \delta\boldsymbol{L}\delta\widehat{\boldsymbol{Q}} = \omega\boldsymbol{M}\widehat{\boldsymbol{Q}} + \omega\boldsymbol{M}\delta\widehat{\boldsymbol{Q}} + \delta\omega\boldsymbol{M}\widehat{\boldsymbol{Q}} + \delta\omega\boldsymbol{M}\delta\widehat{\boldsymbol{Q}}$$

Using the definitions of the forward eigenvalue problem, and ignoring higher order terms, we can simplify as,

$$\begin{aligned} \cancel{\boldsymbol{L}\widehat{\boldsymbol{Q}}} + \boldsymbol{L}\delta\widehat{\boldsymbol{Q}} + \delta\boldsymbol{L}\widehat{\boldsymbol{Q}} + \cancelto{\boldsymbol{H.O.T}}{\delta\boldsymbol{L}\delta\widehat{\boldsymbol{Q}}} &= \cancel{\omega\boldsymbol{M}\widehat{\boldsymbol{Q}}} + \omega\boldsymbol{M}\delta\widehat{\boldsymbol{Q}} + \delta\omega\boldsymbol{M}\widehat{\boldsymbol{Q}} + \cancelto{\boldsymbol{H.O.T}}{\delta\omega\boldsymbol{M}\delta\widehat{\boldsymbol{Q}}} \\ \boldsymbol{L}\delta\widehat{\boldsymbol{Q}} + \delta\boldsymbol{L}\widehat{\boldsymbol{Q}} &= \omega\boldsymbol{M}\delta\widehat{\boldsymbol{Q}} + \delta\omega\boldsymbol{M}\widehat{\boldsymbol{Q}} \end{aligned}$$

Multiplying by the discrete adjoint, we get,

$$\widehat{\boldsymbol{Q}^\dagger}^T \boldsymbol{D}\boldsymbol{L}\delta\widehat{\boldsymbol{Q}} + \widehat{\boldsymbol{Q}^\dagger}^T \boldsymbol{D}\delta\boldsymbol{L}\widehat{\boldsymbol{Q}} = \widehat{\boldsymbol{Q}^\dagger}^T \boldsymbol{D}\omega\boldsymbol{M}\delta\widehat{\boldsymbol{Q}} + \widehat{\boldsymbol{Q}^\dagger}^T \omega\boldsymbol{D}\boldsymbol{M}\widehat{\boldsymbol{Q}}.$$

Using the definition of the adjoint eigenvalue problem, we have $\widehat{\boldsymbol{Q}^\dagger}^T \boldsymbol{D}\boldsymbol{L} = \omega\widehat{\boldsymbol{Q}^\dagger}^T \boldsymbol{D}\boldsymbol{M}$. This gives

$$\begin{aligned} \cancel{\widehat{\boldsymbol{Q}^\dagger}^T \boldsymbol{D}\boldsymbol{L}\delta\widehat{\boldsymbol{Q}}} + \widehat{\boldsymbol{Q}^\dagger}^T \boldsymbol{D}\delta\boldsymbol{L}\widehat{\boldsymbol{Q}} &= \cancel{\widehat{\boldsymbol{Q}^\dagger}^T \boldsymbol{D}\omega\boldsymbol{M}\delta\widehat{\boldsymbol{Q}}} + \widehat{\boldsymbol{Q}^\dagger}^T \delta\omega\boldsymbol{D}\boldsymbol{M}\widehat{\boldsymbol{Q}} \\ \widehat{\boldsymbol{Q}^\dagger}^T \boldsymbol{D}\delta\boldsymbol{L}\widehat{\boldsymbol{Q}} &= \widehat{\boldsymbol{Q}^\dagger}^T \delta\omega\boldsymbol{M}\boldsymbol{D}\widehat{\boldsymbol{Q}}. \end{aligned}$$

Hence, we obtain the discrete structural sensitivity as,

$$\delta\omega = \frac{\widehat{\boldsymbol{Q}^\dagger}^T \boldsymbol{D}\delta\boldsymbol{L}\widehat{\boldsymbol{Q}}}{\widehat{\boldsymbol{Q}^\dagger}^T \boldsymbol{D}\boldsymbol{M}\widehat{\boldsymbol{Q}}}.$$

2.2.6 Linear Feedback Control

The framework developed for the global eigenanalysis is utilized to develop a control strategy using co-located linear feedback, where the feedback sensing is based on the difference between the instantaneous value of the flow variable from that of the baseflow. The Navier-Stokes equations with the control forcing terms is given by,

$$\frac{\mathrm{d}\boldsymbol{Q}}{\mathrm{d}t} = \tilde{\boldsymbol{R}}(\boldsymbol{Q}) + \underbrace{\alpha\boldsymbol{C}(\boldsymbol{Q} - \bar{\boldsymbol{Q}})}_{\text{Forcing } \boldsymbol{F}(\boldsymbol{x},t)}, \tag{2.11}$$

where $\boldsymbol{Q} \equiv (\rho, \rho u, \rho v, \rho w, \rho E)$, α is the control gain and the $\boldsymbol{C}$ is a Gaussian supported control matrix designed to alter the eigensystem of the linearized operator. For example, for a ρw (control) - ρu (feedback) pair, we have

$$\boldsymbol{C} = \underbrace{\begin{bmatrix} 0 & 0 & 0 & 0 & 0 \\ 0 & 0 & 0 & 0 & 0 \\ 0 & 0 & 0 & 0 & 0 \\ 0 & 1 & 0 & 0 & 0 \\ 0 & 0 & 0 & 0 & 0 \end{bmatrix}}_{\tilde{\boldsymbol{C}}} \times e^{-(x-x_0)^2/\ell_x^2 - (y-y_0)^2/\ell_y^2 - (z-z_0)^2/\ell_z^2}, \tag{2.12}$$

where (x_0, y_0, z_0) is the center of the actuator and (ℓ_x, ℓ_y, ℓ_z) is the support in the x, y and z directions respectively. For this linear system, the control gain α is a free parameter that can be varied to change the strength of the control. A discrete structural sensitivity analysis gives the eigenspectrum shift due to the control as

$$\delta\omega = \alpha \frac{\widehat{\boldsymbol{Q}^{\dagger}}^T \boldsymbol{D}\boldsymbol{C}\widehat{\boldsymbol{Q}}}{\widehat{\boldsymbol{Q}^{\dagger}}^T \boldsymbol{D}\boldsymbol{M}\widehat{\boldsymbol{Q}}}. \tag{2.13}$$

The objective we pursue is to optimize the movement of the chosen target eigenvalue. The optimization seeks, for the case of stabilization, the solution

$$\boldsymbol{C}^* \stackrel{\text{def}}{\equiv} \underset{\boldsymbol{C}, ||\tilde{\boldsymbol{C}}||=1}{\text{argmin}} \ \text{Re}(\alpha^{-1}\delta\omega), \tag{2.14}$$

with respect to the parameters $\{\{c_{ij}\}_{i,j=1}^{5}, x_0, y_0, z_0, \ell_x, \ell_y, \ell_z\}$. The optimization is performed using the Trust-Region-Reflective algorithm (Han, 1977). Fig. 2.2 shows the complete flowchart for the active control strategy and analysis.

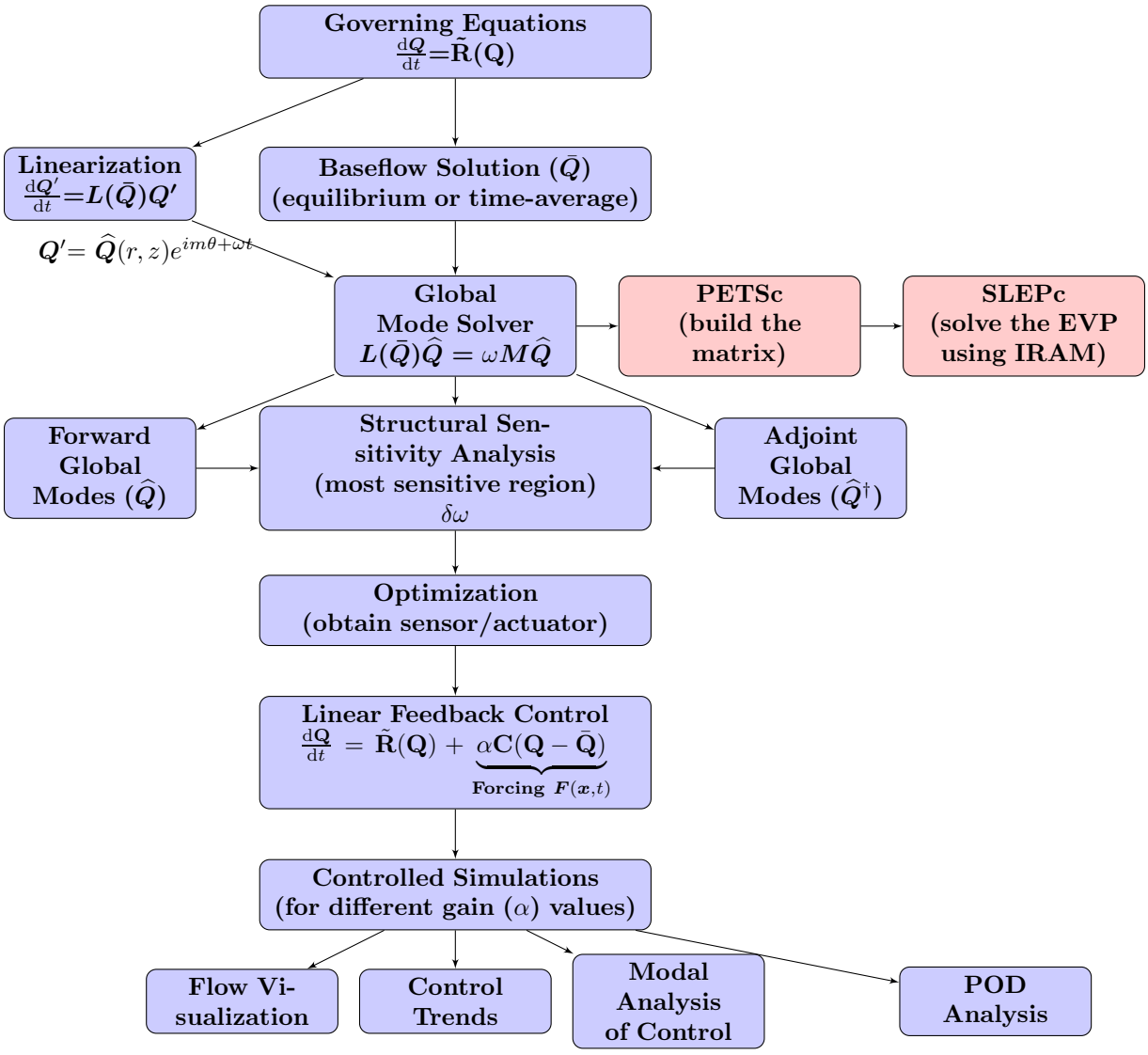

Figure 2.2: Flowchart of the present control strategy and analysis.

Chapter 3

Control of a Separated Boundary Layer in a Diffuser

The control strategy developed in Chapter 2 is applied to the control of a separated boundary layer in a Mach 0.65 diffuser. Section 3.1 describes the governing equations and the formulation of the global eigenvalue problem in generalized coordinates. The verification of the eigenvalue solver with different test cases is detailed in Section 3.2. The baseflow, control development and the controlled simulations and analysis for the Mach 0.65 diffuser are given in Section 3.3. Section 3.4 gives the details of the formulation and results of its application in stabilizing the flow within the diffuser.

3.1 Governing Equations

The compressible Navier-Stokes equations in physical coordinates are given by

$$\begin{aligned} \frac{\partial \rho}{\partial t} + \frac{\partial}{\partial x_i}(\rho u_i) &= 0 \\ \frac{\partial \rho u_i}{\partial t} + \frac{\partial}{\partial x_j}\left(\rho u_i u_j + p\delta_{ij} - \tau_{ij}\right) &= 0 \\ \frac{\partial \rho E}{\partial t} + \frac{\partial}{\partial x_j}\left[\left(\rho E + p\right) u_j + q_j - u_i \tau_{ij}\right] &= 0 \end{aligned} \tag{3.1}$$

where repeated indices are summed. We solve (3.1) on a non-uniform, non-orthogonal mesh defined by the smooth mappings

$$\boldsymbol{x} = \boldsymbol{X}(\boldsymbol{\xi}, t), \text{ with inverse } \boldsymbol{\xi} = \boldsymbol{\Xi}(\boldsymbol{x}, t)$$

where $\boldsymbol{X}^{-1} = \boldsymbol{\Xi}$ and Jacobian $J = |\partial \boldsymbol{X}/\partial \boldsymbol{\Xi}|$. It can be shown that (3.1) maps into an equivalent conservative form in the computational variables $\boldsymbol{\xi}$ (Vinokur (1974)). The time integration is performed using the fourth order Runge-Kutta method. Finite differences are used to approximate the spatial derivatives in the computational coordinates. We use the summation-by-parts operators (Strand (1994)) which, when coupled to the simultaneous-approximation-term (SAT) boundary condition (Svärd *et al.* (2007), Svärd & Nordström (2008)), yield a provably stable method which has been shown to be accurate (Bodony (2010)). The spatial

approximation to $\partial/\partial\xi$ is $\boldsymbol{P}^{-1}\boldsymbol{Q}$ where $\boldsymbol{Q}$ has the property that $\boldsymbol{Q}+\boldsymbol{Q}^T = \mathrm{diag}(-1,0,\ldots,0,1)$. Sponge zones (Colonius (2004)) are used to prevent spurious reflections from the boundaries and to maintain the flow by using a specified target state, $\boldsymbol{Q}_{\mathrm{target}}$. For the SAT formulation, which is a penalization approach, a penalty term is added to the right-hand-side of the governing equations. Following the notation in Svärd *et al.* (2007), the penalized equation with SAT and sponge terms is

$$\frac{\partial \boldsymbol{Q}}{\partial t} = \boldsymbol{R}(\boldsymbol{Q}) + \underbrace{\sigma_i \boldsymbol{P}^{-1}\boldsymbol{E}_1\boldsymbol{A}^{+}(\boldsymbol{Q}-\boldsymbol{g_i})}_{\textbf{SAT inviscid}} + \underbrace{\frac{\sigma_v}{\mathrm{Re}}\boldsymbol{P^{-1}}\boldsymbol{E_1}\mathcal{I}(\boldsymbol{Q}-\boldsymbol{g_v})}_{\textbf{SAT viscous}} - \underbrace{A_s\kappa^{n_s}(\boldsymbol{Q}-\boldsymbol{Q}_{\mathrm{target}})}_{\textbf{Sponge zone}} \tag{3.2}$$

where σ_i and σ_v are the penalty parameters for the inviscid and viscous boundary conditions, respectively, and $\boldsymbol{E_1} = (1,0,\ldots,0)^T$. Here $\boldsymbol{R}(\boldsymbol{Q})$ represents the divergence of the fluxes in the governing equations, $\boldsymbol{A}^{+}$ is a Roe matrix, and $\mathcal{I}$ is the identity matrix. It is known that $\sigma_i \leq -2$ and

$$\sigma_v \leq -\frac{1}{4p_0}\max\left(\frac{\gamma\mu}{\mathrm{Pr}\rho}, \frac{5\mu}{3\rho}\right) \tag{3.3}$$

for stability. Also, A_s is the amplitude of the sponge, n_s, the spatial strength and κ is the scaled coordinate which ranges from 0 at the interior of the sponge to 1 at the exterior.

For the present work, the two-dimensional compressible Navier-Stokes equations in generalized coordinates are solved,

$$\begin{aligned}\frac{\partial \boldsymbol{Q}}{\partial t} &= -J\left[\frac{\partial \widehat{\boldsymbol{E}}}{\partial\xi} + \frac{\partial \widehat{\boldsymbol{F}}}{\partial\eta}\right] + \frac{J}{Re}\left[\frac{\partial \widehat{\boldsymbol{E_v}}}{\partial\xi} + \frac{\partial \widehat{\boldsymbol{F_v}}}{\partial\eta}\right] \\ &+ \underbrace{\sigma_i \boldsymbol{P}^{-1}\boldsymbol{E}_1\boldsymbol{T_k}\boldsymbol{\Lambda}^{+}\boldsymbol{T_k}^{-1}(\mathcal{I}-\boldsymbol{g_i}(\boldsymbol{Q}))}_{\textbf{SAT inviscid}} + \underbrace{\frac{\sigma_v}{Re}\boldsymbol{P^{-1}}\boldsymbol{E_1}(\mathcal{I}-\boldsymbol{g_v}(\boldsymbol{Q}))}_{\textbf{SAT viscous}} - \underbrace{A_s\kappa^{n_s}(\boldsymbol{Q}-\boldsymbol{Q}_{\mathrm{target}})}_{\textbf{Sponge Zone}}\end{aligned} \tag{3.4}$$

where J is the grid Jacobian, $\widehat{\boldsymbol{E}}$ and $\widehat{\boldsymbol{F}}$ are the inviscid fluxes and $\widehat{\boldsymbol{E_v}} = \frac{1}{J}(\xi_x\boldsymbol{E_v} + \xi_y\boldsymbol{F_v})$ and $\widehat{\boldsymbol{F_v}} = \frac{1}{J}(\eta_x\boldsymbol{E_v} + \eta_y\boldsymbol{F_v})$ are the viscous fluxes with

$$\boldsymbol{Q} = \begin{bmatrix}\rho\\ \rho u\\ \rho v\\ \rho E\end{bmatrix}, \quad \boldsymbol{E_v} = \begin{bmatrix}0\\ \tau_{xx}\\ \tau_{xy}\\ f_4\end{bmatrix}, \quad \boldsymbol{F_v} = \begin{bmatrix}0\\ \tau_{xy}\\ \tau_{yy}\\ g_4\end{bmatrix},$$

and

$$\begin{aligned}
\tau_{xx} &= (2\mu+\lambda)(\xi_x u_\xi + \eta_x u_\eta) + \lambda(\xi_y v_\xi + \eta_y v_\eta) \\
\tau_{xy} &= \mu(\xi_y u_\xi + \eta_y u_\eta + \xi_x v_\xi + \eta_x v_\eta) \\
\tau_{yy} &= \lambda(\xi_x u_\xi + \eta_x u_\eta) + (2\mu+\lambda)(\xi_y v_\xi + \eta_y v_\eta) \\
f_4 &= u\tau_{xx} + v\tau_{yy} + \frac{\mu}{Pr(\gamma-1)}(\xi_x \partial_\xi a^2 + \eta_x \partial_\eta a^2) \\
g_4 &= u\tau_{xy} + v\tau_{yy} + \frac{\mu}{Pr(\gamma-1)}(\xi_y \partial_\xi a^2 + \eta_y \partial_\eta a^2).
\end{aligned}$$

The non dimensional variables used in the formulation are

$$t = \frac{t^*}{L^*/c_\infty}, \quad x_i = \frac{x_i^*}{L}, \quad \rho = \frac{\rho^*}{\rho_\infty}, \quad u_i = \frac{u_i^*}{c_\infty}, \quad p = \frac{p^*}{\rho_\infty c_\infty^2}, \quad T = \frac{T^*}{(\gamma-1)T_\infty}, \quad \mu = \frac{\mu^*}{\mu_\infty}, \quad \lambda = \frac{\lambda^*}{\lambda_\infty}$$

where '*' denotes the dimensional variables, L is an appropriate characteristic length scale of the problem and the subscript '∞' refers to the initial incoming freestream values of the variables.

To perform the linear stability analysis of the Navier-Stokes equations, we linearize (3.4) about a steady solution, $\bar{\boldsymbol{Q}}$. The linearized equations with all the boundary terms included are,

$$\begin{aligned}
\frac{\partial \boldsymbol{Q}'}{\partial t} &= -\Bigg[\underbrace{J\widehat{\boldsymbol{A}}\frac{\partial}{\partial\xi} + J\widehat{\boldsymbol{B}}\frac{\partial}{\partial\eta} + J\frac{\partial\widehat{\boldsymbol{A}}}{\partial\xi} + J\frac{\partial\widehat{\boldsymbol{B}}}{\partial\eta}}_{\textbf{Inviscid}} - \underbrace{\frac{J}{Re}\left[\frac{\partial\widehat{\boldsymbol{E_v}}'}{\partial\xi} + \frac{\partial\widehat{\boldsymbol{F_v}}'}{\partial\eta}\right]}_{\textbf{Viscous}} \\
&- \underbrace{\sigma_i \boldsymbol{P^{-1}E_1T_k\Lambda^+T_k^{-1}}(\mathcal{I} - \boldsymbol{g_i'(Q)})}_{\textbf{SAT inviscid}} - \underbrace{\frac{\sigma_v}{Re}\boldsymbol{P^{-1}E_1}(\mathcal{I} - \boldsymbol{g_v'(Q)})}_{\textbf{SAT viscous}} + \underbrace{A_s\kappa^{n_s}}_{\textbf{Sponge Zone}}\Bigg]\boldsymbol{Q}' = \mathbf{L}(\bar{\mathrm{Q}})\boldsymbol{Q}' \quad (3.5)
\end{aligned}$$

where $\boldsymbol{Q}'$ is the small perturbation to $\bar{\boldsymbol{Q}}$. The inviscid flux Jacobian matrices are given by

$$\widehat{\boldsymbol{A}} \text{ or } \widehat{\boldsymbol{B}} = \frac{1}{J}\begin{bmatrix}
k_t & k_x & k_y & 0 \\
-u\theta + k_x\phi^2 & k_t + \theta - (\gamma-2)k_x u & k_y u - (\gamma-1)k_x v & (\gamma-1)k_x \\
-v\theta + k_y\phi^2 & k_x v - (\gamma-1)k_y u & k_t + \theta - (\gamma-2)k_y v & (\gamma-1)k_y \\
\theta[2\phi^2 - \gamma\frac{\rho e}{\rho}] & k_x[\gamma\frac{\rho e}{\rho} - \phi^2] - (\gamma-1)u\theta & k_y[\gamma\frac{\rho e}{\rho} - \phi^2] - (\gamma-1)v\theta & \gamma\theta + k_t
\end{bmatrix}$$

where $\theta = k_x u + k_y v$ and $\phi^2 = 0.5(\gamma-1)(u^2+v^2)$ with $k = \xi$ for $\widehat{\boldsymbol{A}}$ and $k = \eta$ for $\widehat{\boldsymbol{B}}$. The eigenvalues of $\widehat{\boldsymbol{A}}$ and $\widehat{\boldsymbol{B}}$ are given by

$$\boldsymbol{\Lambda_k} = [U_k, U_k, U_k + c(k_x^2+k_y^2)^{\frac{1}{2}}, U_k - c(k_x^2+k_y^2)^{\frac{1}{2}}],$$

where $k = \xi$ or η for ξ = constant or η = constant boundaries, respectively, and U_k are the contravariant velocities given by $U_\xi = U = \xi_t + \xi_x\bar{u} + \xi_y\bar{v}$ and $U_\eta = V = \eta_t + \eta_x\bar{u} + \eta_y\bar{v}$. The linearization of the viscous terms is given in Appendix B.

3.1.1 Boundary Conditions

This section gives a term-by-term description of all the boundary conditions used in the formulation as shown in (3.5). The SAT rotation matrices, far-field boundary conditions (SAT and sponge zones), and inviscid and viscous wall boundary treatment are described.

Rotation Matrices (SAT)

The rotation matrices for implementing the SAT boundary conditions in (3.5) are given by Pulliam & Chaussee (1981) as,

$$\boldsymbol{T_k} = \begin{bmatrix} 1 & 0 & \alpha & \alpha \\ u & \tilde{k}_y\rho & \alpha(u+\tilde{k}_x c) & \alpha(u-\tilde{k}_x c) \\ v & -\tilde{k}_x\rho & \alpha(v+\tilde{k}_y c) & \alpha(v-\tilde{k}_y c) \\ \frac{\phi^2}{\gamma-1} & \rho(\tilde{k}_y u - \tilde{k}_x v) & \alpha\Big[\frac{\phi^2+c^2}{(\gamma-1)} + c\tilde{\theta}\Big] & \alpha\Big[\frac{\phi^2+c^2}{(\gamma-1)} - c\tilde{\theta}\Big] \end{bmatrix}$$

and

$$\boldsymbol{T_k^{-1}} = \begin{bmatrix} \Big(1-\frac{\phi^2}{c^2}\Big) & (\gamma-1)\frac{u}{c^2} & (\gamma-1)\frac{v}{c^2} & -(\gamma-1)\frac{1}{c^2} \\ -\frac{1}{\rho}(\tilde{k}_y u - \tilde{k}_x v) & \frac{1}{\rho}\tilde{k}_y & -\frac{1}{\rho}\tilde{k}_x & 0 \\ \beta(\phi^2 - c\tilde{\theta}) & \beta[\tilde{k}_x c - (\gamma-1)u] & \beta[\tilde{k}_y c - (\gamma-1)v] & \beta(\gamma-1) \\ \beta(\phi^2 + c\tilde{\theta}) & -\beta[\tilde{k}_x c + (\gamma-1)u] & -\beta[\tilde{k}_y c + (\gamma-1)v] & \beta(\gamma-1) \end{bmatrix},$$

where $\alpha = \rho/\sqrt{2}c$, $\beta = 1/\sqrt{2}c$, $\tilde{\theta} = \tilde{k}_x u + \tilde{k}_y v$ and $\tilde{k}_x = k_x/(k_x^2 + k_y^2)$.

Far-Field Boundaries

The far-field boundary condition imposes zero perturbations for all the incoming characteristic variables. Hence the penalty term is $\boldsymbol{g_i'}(\boldsymbol{Q}) \equiv 0$ in (3.5).

Inviscid Wall

The inviscid wall boundary condition in the SAT treatment will have the following penalty term in two dimensions,

$$\boldsymbol{g_i}(\boldsymbol{Q}) = \begin{bmatrix} \rho \\ \rho(\boldsymbol{u} - (\boldsymbol{u}\cdot\widehat{\boldsymbol{n}})\widehat{\boldsymbol{n}}) \\ \frac{p}{\gamma-1} + \frac{1}{2}\rho|(\boldsymbol{u} - (\boldsymbol{u}\cdot\widehat{\boldsymbol{n}})\widehat{\boldsymbol{n}})|^2 \end{bmatrix} = \begin{bmatrix} \rho \\ \rho u(1-n_x^2) - \rho v n_x n_y \\ -\rho u n_x n_y + \rho v(1-n_y^2) \\ \rho e - \frac{1}{2}\frac{(\rho u n_x + \rho v n_y)^2}{\rho} \end{bmatrix},$$

with the corresponding perturbation,

$$\boldsymbol{g_i'}(\boldsymbol{Q}) = \begin{bmatrix} 1 & 0 & 0 & 0 \\ 0 & 1-n_x^2 & -n_x n_y & 0 \\ 0 & -n_x n_y & 1-n_y^2 & 0 \\ \frac{1}{2}(un_x+vn_y)^2 & -(un_x+vn_y)n_x & -(un_x+vn_y)n_y & 1 \end{bmatrix},$$

where n_x and n_y are the components of the unit wall normal vector.

Viscous Wall

The viscous wall boundary condition in the SAT sense involves the addition of a corresponding viscous penalty term. For an isothermal wall with temperature T_w, the target vector is given by

$$\boldsymbol{g_v}(\boldsymbol{Q}) = \begin{bmatrix} \rho \\ \boldsymbol{0} \\ \frac{\rho T_w}{\gamma} \end{bmatrix}, = \begin{bmatrix} \rho \\ 0 \\ 0 \\ \frac{\rho T_w}{\gamma} \end{bmatrix},$$

with the corresponding perturbation,

$$\boldsymbol{g_v'}(\boldsymbol{Q}) = \begin{bmatrix} 1 & 0 & 0 & 0 \\ 0 & 0 & 0 & 0 \\ 0 & 0 & 0 & 0 \\ \frac{T_w}{\gamma} & 0 & 0 & 0 \end{bmatrix}.$$

Sponge Zones

For the treatment of the far field boundaries, where the perturbations decay to infinitesimal values, sponge zones (Colonius (2004)) are effective. In the linearized Navier-Stokes equations, this consists of adding a source term to the equations

$$\frac{\mathrm{d}\boldsymbol{Q}'}{\mathrm{d}t} = \boldsymbol{L}(\bar{\boldsymbol{Q}})\boldsymbol{Q}' - A_s\kappa^{n_s}(\boldsymbol{Q}' - \boldsymbol{Q}'_{\text{target}}),$$

where $\boldsymbol{Q}'_{\text{target}}$ is the target state for the sponge region. Since the target state is not dependent on the flow solution, $\boldsymbol{Q}'_{\text{target}} \equiv 0$.

3.2 Verification

To verify the implementation of the global eigenmode solver, we perform linear stability analyses for several standard test cases and compare the results with the existing literature. The following section describes the verification procedure. Inviscid and viscous test cases involving all boundary treatment terms are performed to verify the code.

3.2.1 Test Case 1 - Compressible Inviscid Wall Bounded Mixing Layer

The test case considered here is the temporal inviscid stability analysis of a streamwise periodic bounded compressible mixing layer with $\Delta u/c_1 = 1$ as shown in Fig. 3.1(a). This test case verifies the inviscid terms in the equations and the inviscid SAT wall boundary treatment. To compare the results, the problem is also solved using a one-dimensional shooting method and the eigenvalues and eigenmodes obtained from the two methods are compared. A growth rate comparison from the eigenvalue solution against that predicted by the direct numerical simulation is also used for a test of consistency.

Baseflow Profiles

A hyperbolic tangent velocity profile is chosen and the temperature is obtained from the Crocco-Busemann relation (Ragab & Wu (1989)). The pressure is assumed to be constant across the mixing layer and the

Case	Wavenumber	Eigenvalue ($\omega_r + i\omega_i$)	
	α	Local Analysis	Global Analysis
1	3	$1.0211 + 0.0764i$	$1.0234 + 0.0767i$
2	4	$1.3000 + 0.1007i$	$1.3061 + 0.1002i$
3	8	$2.1334 + 0.1838i$	$2.1085 + 0.1850i$

Table 3.1: Comparison of eigenvalues from local and global analysis for wall bounded compressible shear layer.

density is calculated from the ideal gas law. The baseflow profiles used in the present analysis are given by

$$\begin{aligned} \bar{u}(y) &= M \tanh\Big(\frac{2y}{\delta}\Big) \\ T(y) &= T_r\left(\frac{1-\bar{U}(y)}{1-U_r}\right) + \left(\frac{\bar{U}(y)-U_r}{1-U_r}\right) + (\gamma-1)M^2(1-\bar{U}(y))(\bar{U}(y)-U_r) \\ \rho(y) &= \frac{\gamma p}{(\gamma-1)T}, \end{aligned}$$

where $M = 0.5$, $T_r = T_1/T_2 = 0.7$ and $U_r = U_1/U_2 = -1.0$, $\delta = 0.05$ and the nondimensional variables are given by

$$\rho = \frac{\rho^*}{\rho_1^*}, \quad u = \frac{u^*}{c_1^*}, \quad v = \frac{v^*}{c_1^*}, \quad T = \frac{T^*}{(\gamma-1)T_1^*}, \quad p = \frac{p^*}{\rho_1^* c_1^{*2}},$$

where the '*' denotes the dimensional variables.

Global 2D Analysis

The eigenmode analysis of the baseflow was performed using the global eigenvalue solver described and the 1-D method in Appendix A. Table 3.1 shows the comparison of eigenvalues for 3 cases with different streamwise wavenumbers (α). Fig. 3.1(b)-(e) shows the comparison of the eigenmodes. A good quantitative comparison verifies the inviscid terms in the formulation and the inviscid wall boundary conditions.

Growth Rate - Direct Numerical Simulation

The growth rate test checks for the consistency of the results obtained from the global stability analysis and the nonlinear Navier-Stokes solver. The obtained perturbations from the global eigenmode solver are added to the steady baseflow and provided as an initial condition to perform a DNS. The growth rate of the perturbations obtained from the DNS are then compared with that obtained from the linear stability analysis ($\omega_r = \mathrm{Re}(\omega)$, the real part of the eigenvalue). In global stability analysis, the perturbations added

take the following form,

$$\begin{aligned}
\boldsymbol{Q'}(\boldsymbol{x},t) &= \mathrm{Re}\{\widehat{\boldsymbol{Q}}(\boldsymbol{x})e^{\omega t}\} \\
&= \mathrm{Re}\{(\widehat{\boldsymbol{Q_r}}(\boldsymbol{x}) + i\widehat{\boldsymbol{Q_i}}(\boldsymbol{x}))e^{(\omega_r + i\omega_i)t}\} \\
&= e^{\omega_r t}\Big(\widehat{\boldsymbol{Q_r}}(\boldsymbol{x})\cos(\omega_i t) - \widehat{\boldsymbol{Q_i}}(\boldsymbol{x})\sin(\omega_i t)\Big).
\end{aligned}$$

which is approximately,

$$\boldsymbol{Q'}(\boldsymbol{x},t) \approx e^{\omega_r t}\widehat{\boldsymbol{Q_r}},$$

for small times given by $\omega_i t \ll 1$.

The initial perturbation corresponds to a given streamwise wavenumber (say α). Taking the Fourier transform of the above equation and equating the Fourier amplitudes corresponding to α, we get

$$\begin{aligned}
\tilde{\boldsymbol{Q}}'(\alpha,t) &\approx e^{\omega_r t}\widetilde{\widehat{\boldsymbol{Q_r}}}(\alpha) \\
\ln(|\tilde{\boldsymbol{Q}}'(\alpha,t)|) &\approx \omega_r t + \ln(|\widetilde{\widehat{\boldsymbol{Q_r}}}(\alpha)|).
\end{aligned}$$

The above equation represents a straight line on a semilog plot for the perturbation amplitudes $|\boldsymbol{Q'}(\alpha,t)|$. The validated unstable eigenmode found from the eigenvalue analysis was added to the baseflow and the growth rate of the eigenmode was obtained from the in-house Navier-Stokes solver. Fig. 3.2 shows the growth rate comparison. A good comparison of the growth rate shows the consistency of the global eigenmode solver and the DNS.

Test Case 1 - Summary

This test case verifies the inviscid terms in the linearized equations and the inviscid boundary conditions. Good quantitative agreement of the eigenvalues can be observed from the comparison in Table 3.1 and those of the eigenmodes in Fig 3.1. The growth rate also matches well with the DNS as shown in Fig 3.2.

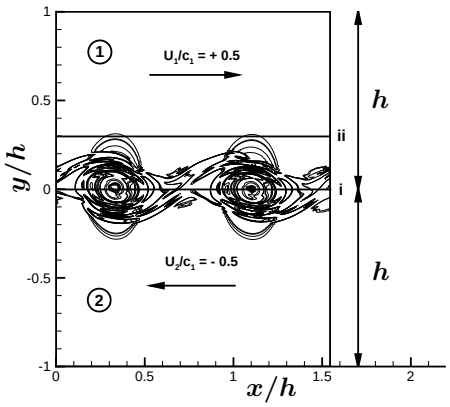

(a)

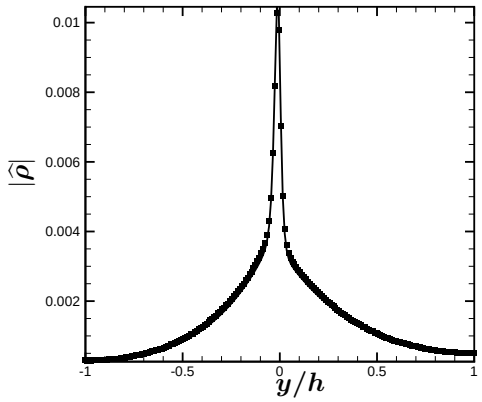

(b)

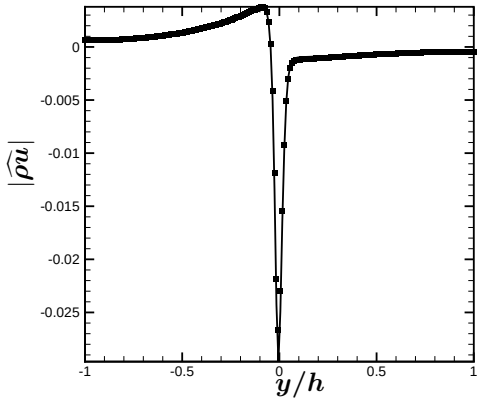

(c)

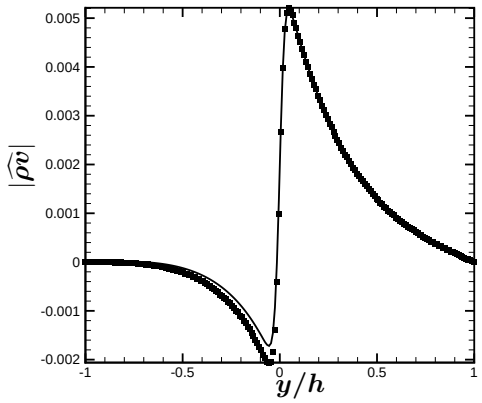

(d)

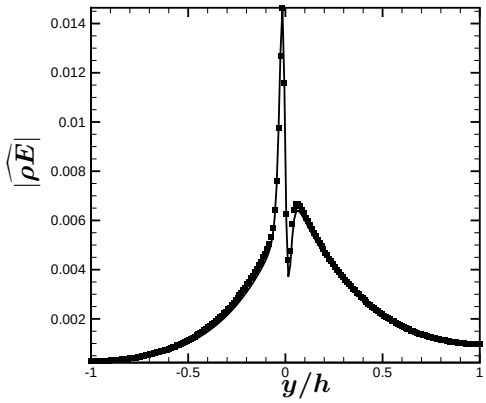

(e)

Figure 3.1: (a) Schematic of the wall bounded mixing layer; comparison of the absolute value of eigenmodes in the y direction for case 1: (b) $\widehat{\rho}$ (c) $\widehat{\rho u}$ (d) $\widehat{\rho v}$ and (e) $\widehat{\rho E}$ (1D (solid line) and 2D (symbols)).

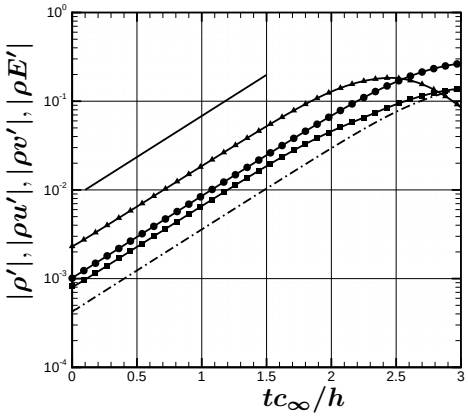

Figure 3.2: Growth rate comparison: global stability analysis (solid) and DNS: $\widehat{\rho}$ (■), $\widehat{\rho u}$ (▲), $\widehat{\rho v}$ (−.−), $\widehat{\rho e}$(●).

3.2.2 Test Case 2 - Boundary Layer

This test case considers the global viscous instability of a streamwise periodic boundary layer. The baseflow used a similarity solution of the compressible boundary layer equations. Test cases were done at two free stream Mach numbers : 0.05 and 10.0. This test case verifies all the terms in the formulation with the SAT wall boundary treatment and the SAT far-field boundary treatment. The comparison is done with the eigenvalues and eigenmodes from Malik (1990). A growth rate comparison with DNS is also tested for consistency.

Mach 0.05 Boundary Layer

The baseflow was obtained from the compressible similarity solution of the boundary layer equations at a Reynolds number (based on displacement thickness) of $Re_{\delta^*} = 2000$. Table 3.2 shows the comparison of eigenvalues. The comparison of the eigenmodes is shown in Fig. 3.3, and Fig. 3.4 shows the growth from the DNS.

Solver	$\omega_r + i\omega_i$
1D	$2.0695 \times 10^{-4} - 3.2991 \times 10^{-3} i$
Global	$2.0723 \times 10^{-4} - 3.2997 \times 10^{-3} i$

Table 3.2: Comparison of eigenvalues for the 1D temporal solver and global solver for the case of $M = 0.05$ boundary layer.

Growth Rate - Direct Numerical Simulation

The validated Tollmien-Schlichting unstable eigenmode found from the eigenvalue analysis was added to the baseflow and the growth rate of the eigenmode was obtained from the in-house Navier-Stokes solver. The growth rate comparison at $y = 0.2\delta^*$ is shown in Fig. 3.4.

Mach 10.0 Boundary Layer

The baseflow was obtained from the compressible similarity solution of the boundary layer equations at a Reynolds number (based on displacement thickness) of $Re_{\delta^*} = 31670$. Table 3.3 shows the comparison of eigenvalues for the Mach 10.0 spatially periodic boundary layer. The corresponding comparison of the eigenmodes is shown in Fig. 3.5. A growth rate comparison is not done since the baseflow is not a steady solution of the compressible boundary layer equations.

Solver	$\omega_r + i\omega_i$
1D	$0.1030 - 36.7066i$
Global	$0.1160 - 36.6241i$

Table 3.3: Comparison of the eigenvalue for the global solver with the result from Malik (1990) for the case of $M = 10.0$ boundary layer.

Test Case 2 - Summary

All the terms of the solver (inviscid, viscous and boundary terms) are verified by this test case. Good quantitative agreement of the eigenvalues and eigenmodes can be observed from the comparisons. The growth rate also matches well with the DNS as shown in Fig 3.4.

3.3 Flow Control in a Mach 0.65 Diffuser

Flow separation can lead to significant stagnation pressure loss at the diffuser exit (fan inlet) and can lead to considerable deterioration of engine performance. The vortex shedding in the diffuser also generates undesirable unsteady loads on the fan. In this section, we apply the control strategy developed in Chapter 2 to control vortex shedding in a Mach 0.65 diffuser.

3.3.1 Domain, Boundary Conditions and Flow Conditions

Fig. 3.6(a) shows the computational domain drawn to scale (δ, the boundary layer thickness of the incoming boundary layer, is the chosen length scale). The grid size was $(N_\xi, N_\eta) = (1386, 200)$. The incoming flow is

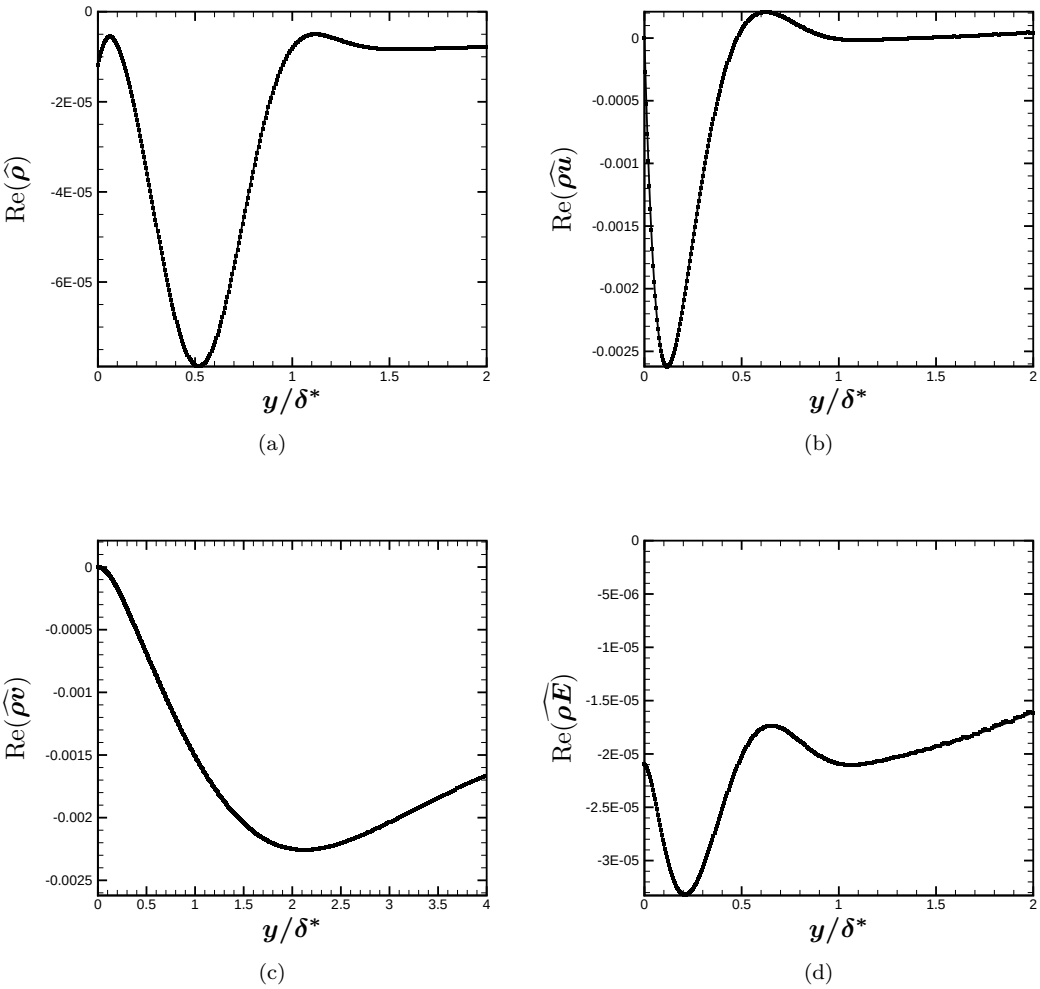

Figure 3.3: Comparison of eigenmodes for $M = 0.05$ boundary layer: 1D (solid lines) and global (symbols).

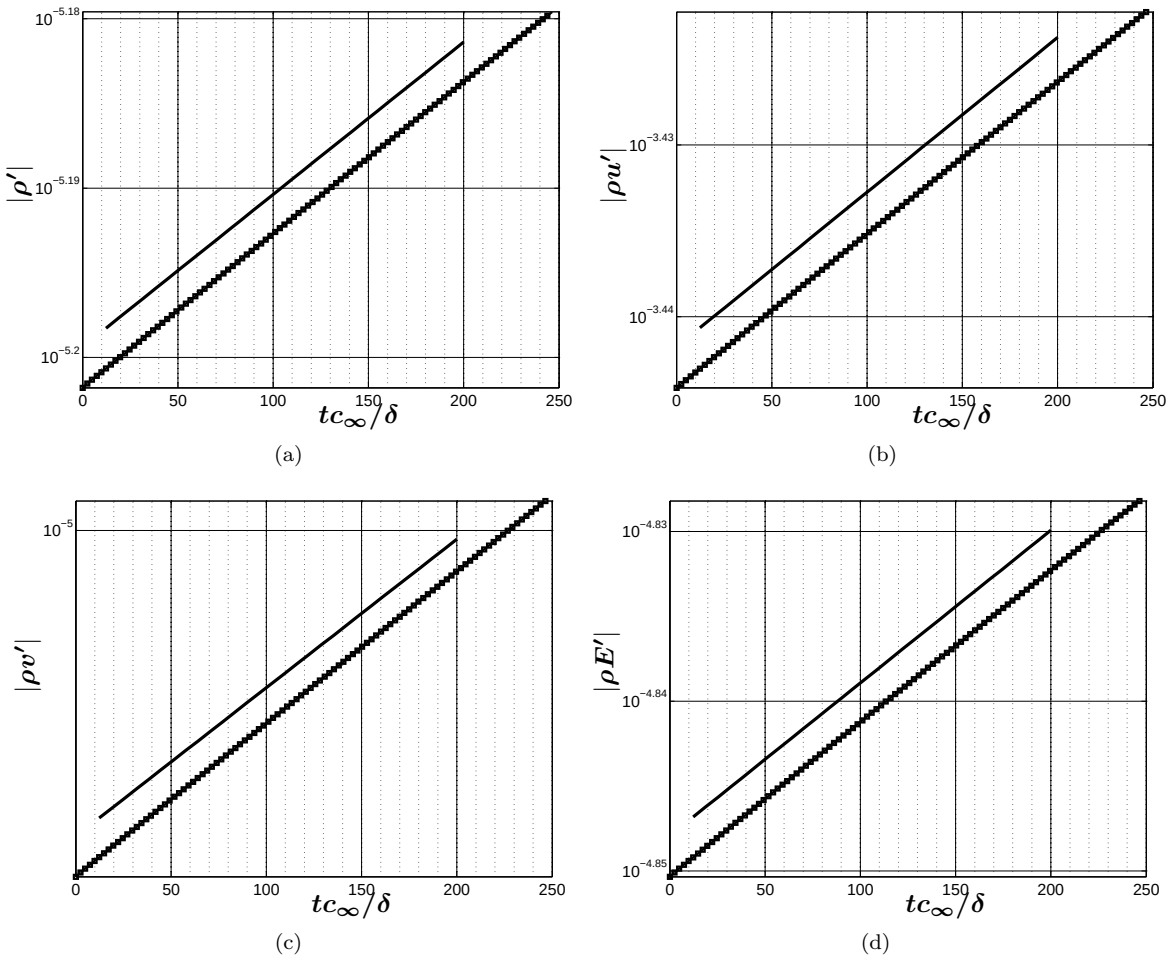

Figure 3.4: Growth rate comparison at $y = 0.2\delta^*$: (a) $|\rho'|$, (b) $|\rho u'|$, (c) $|\rho v'|$ and (d) $|\rho E'|$. The symbols denote the simulation result and the solid line shows the global stability result with slope $\omega_r = 0.000207$.

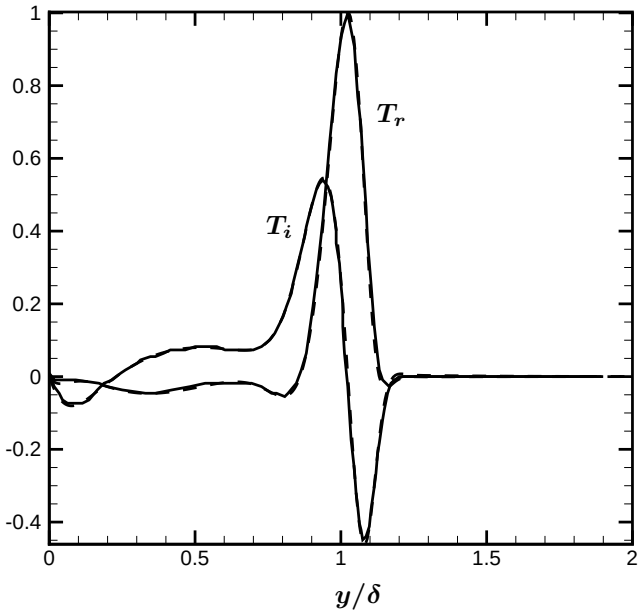

Figure 3.5: Comparison of the real and imaginary parts of the temperature eigenmode for the $M = 10.0$ flat plate boundary layer: $--$ global; — Malik (1990).

a Mach 0.65 boundary layer with $T_\infty = 300$ K and $\rho_\infty = 1.225$ kg/m^3 at a Reynolds number of $c_\infty \delta/\nu = 250$. The core properties at the outflow were calculated using the isentropic quasi-steady 1D analysis of the core flow from the inlet to the outlet. Similarity solution of the compressible boundary layer equations was used to generate the boundary layer profiles at the inflow and outflow, and the solution within the diffuser was obtained by a linear interpolation between the inflow and the outflow. The initial condition was such that mass is conserved within the domain, ie. $\dot{m}_{\text{inflow}} \approx \dot{m}_{\text{outflow}}$. Table 3.4 shows the outflow-to-inflow ratio of the flow properties. Fig. 3.6(b) shows the boundary conditions used in the simulations. SAT boundary conditions were enforced on all boundaries. The lower wall is viscous and the upper wall is inviscid. The inflow and outflow boundaries were treated as SAT far-field boundaries. Sponge (absorbing) zones were used at the inflow and outflow to prevent spurious reflections of outgoing waves into the computational domain.

Outflow/Inflow	Ratio
A_2/A_1	1.436
T_2/T_1	1.062
p_2/p_1	1.235
ρ_2/ρ_1	1.162

Table 3.4: Ratio of outflow to inflow properties (initial condition) from quasi-steady 1D analysis.

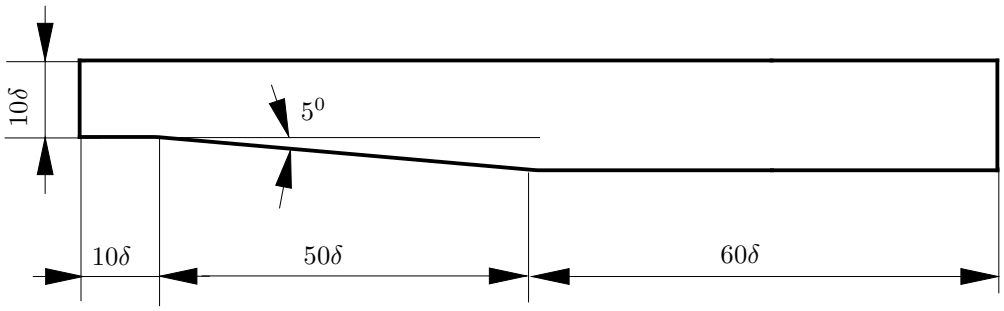

(a)

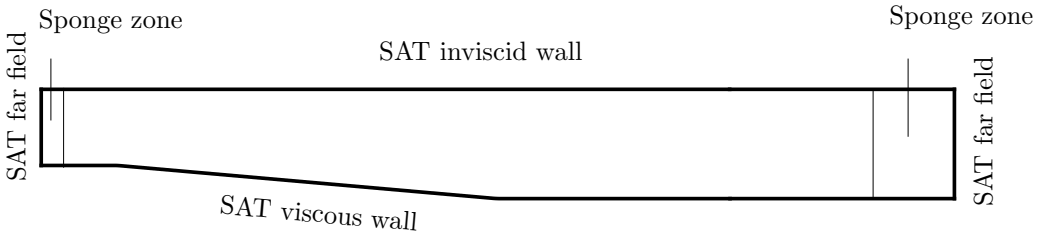

(b)

Figure 3.6: (a) Computational domain (drawn to scale, δ is the boundary layer thickness of the incoming boundary layer). (b) Boundary conditions used in the simulation.

3.3.2 Steady Baseflow for the Mach 0.65 Diffuser

The steady baseflow solution for the Mach 0.65 diffuser is computed using the Selective Frequency Damping technique described in Section 2.1. Table 3.5 shows the values of the parameters used in the SFD analysis, obtained from the eigenanalysis of an instantaneous snapshot of the unsteady flow. Fig. 3.7(a) shows the Mach number contours for the equilibrium baseflow $\boldsymbol{Q}_e$ for which the residual $||\tilde{\boldsymbol{R}}(\boldsymbol{Q}_e)||_\infty$ was reduced to 10^{-11} over time $\Delta t c_\infty/\delta = 10\ 000$. Fig. 3.7(b) shows the time history of the L_∞ norm of the right hand side of the Navier-Stokes equations for the SFD analysis. Mesh independence was established by verifying that the relevant portion of the global eigenspectrum for the steady baseflow showed very little change upon refinement (e.g., the change in the growth rate of the most unstable eigenmode was less than 0.02% upon increasing the number of grid points by a factor of 2). Further quantitative comparisons of the growth rate of the global modes, those computed directly from the simulation, and those from the linear stability analysis also showed that the simulation was well resolved (not shown).

Parameter	Value
χ (gain)	0.05
Δ (filter width)	20.0

Table 3.5: Parameters used for selective frequency damping.

3.3.3 Flow Control with Linear Feedback Forcing

This section describes the methodology for estimating the actuator type and location for flow control in high subsonic diffusers utilizing the forward ($\widehat{\boldsymbol{Q}}$) and adjoint global modes ($\widehat{\boldsymbol{Q}^\dagger}$) of the Navier-Stokes equations. We consider the case of a linear feedback forcing to affect flow control. The objective of the controller is to control the growth rate of specific global modes of the baseflow to render them less unstable, thus reducing the unsteady loads on the fan face. The verified eigenvalue solver developed can be used to compute the forward and adjoint (discrete) modes of the compressible Navier-Stokes equations. The adjoint modes give valuable information regarding the receptivity of the flow. The "wavemaker" theory uses the forward ($\widehat{\boldsymbol{Q}}$) and adjoint global modes ($\widehat{\boldsymbol{Q}^\dagger}$) to obtain an estimate of the most effective location of the controller. We extend the theory to estimate the most effective location and the shape of the controller for specific control-feedback pairs.

(a)

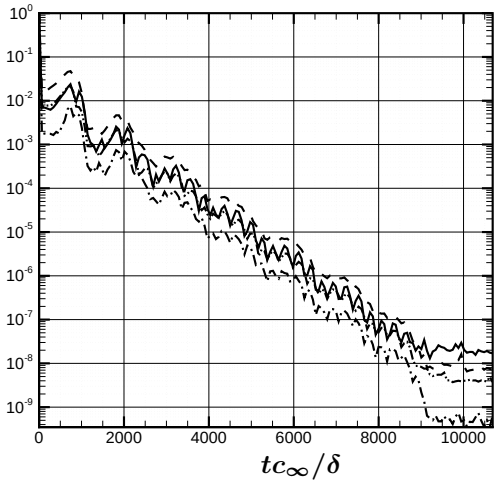

(b)

Figure 3.7: (a) Mach number contours at steady state and (b) history of DNS with SFD technique showing the change in the RHS of the Navier-Stokes equations : $\frac{||\text{RHS}||_{\text{L}_\infty}}{||\text{RHS}||_{\text{L}_\infty,t=0}}$: —ρ, — —ρu, — · —ρv, — ·· —ρE.

3.3.4 Eigenspectrum, Eigenmodes and Wavemaker

The eigenanalysis of the steady baseflow was performed to find the unstable and least stable eigenvalues and the forward and adjoint eigenmodes of the system using a shift-and-invert spectral transformation. Different target eigenvalues for ω_r in the range $\{0.02, 0.1\}$ (along the real axis) were chosen to ensure the independence of the most unstable portion of the eigenspectrum of the system. Fig. 3.8(a) shows the eigenvalue spectrum with the target eigenvalue $(\omega_r^{\text{target}}, \omega_i^{\text{target}})=(0.02, -0.1)$. Fig. 3.8(b) shows the unstable region of the eigenspectrum for three different target eigenvalues. It can be seen that the unstable portion of the eigenspectrum does not change with the change in the target, showing the independence of the desired region of the spectrum with respect to the target eigenvalue.

The eigenmodes of the adjoint system differ from the forward problem and therefore, corresponding to every eigenvalue, we obtain a forward-adjoint pair of eigenmodes. Using the forward and adjoint eigenmodes, the wavemaker can be computed for any given eigenvalue of the system. Giannetti & Luchini (2007) define

a wavemaker region as the region in space where a modification of the structure of the problem produces the largest drift in the eigenvalue of the system. The wavemaker is defined as the region where

$$\zeta(x,y) \equiv \frac{||\widehat{\boldsymbol{Q}}(x,y)||\ ||\widehat{\boldsymbol{Q}}^{\dagger}(x,y)||}{\int\limits_{\mathcal{D}} \widehat{\boldsymbol{Q}} \cdot \widehat{\boldsymbol{Q}}^{\dagger}\, d\mathcal{S}} \tag{3.6}$$

attains 'large' values, where $\widehat{\boldsymbol{Q}} \equiv \{\widehat{\rho}, \widehat{\rho u}, \widehat{\rho v}, \widehat{\rho E}\}$ and $\widehat{\boldsymbol{Q}^{\dagger}} \equiv \{\widehat{\rho^{\dagger}}, \widehat{\rho u^{\dagger}}, \widehat{\rho v^{\dagger}}, \widehat{\rho E^{\dagger}}\}$. The norm is defined by $||\widehat{\boldsymbol{Q}}|| \equiv \sqrt{|\widehat{\rho}|^2 + |\widehat{\rho u}|^2 + |\widehat{\rho v}|^2 + |\widehat{\rho E}|^2}$. The results of the wavemaker analysis for the most unstable eigenvalue for the diffuser are described in this section. Controller selection and placement for localized linear feedback control requires the solution of the optimization problem (2.14), with $\tilde{\boldsymbol{C}}$ bounded, applied to a specific eigenvalue. To demonstrate the method we target the most unstable eigenvalue in Fig. 3.9(a) whose forward and adjoint global modes are shown in Fig. 3.9(b) and (c), and wavemaker ζ in Fig. 3.9(d). Observe that the wavemaker shown in Fig. 3.9(c) suggests that the separated flow may be efficiently affected by a controller slightly downstream of the diffuser corner. However, it does not suggest which specific actuator(s)/sensor(s) pair should be examined nor does it yield a spatially precise location for actuation that is specific to the actuator(s)/sensor(s) pair.

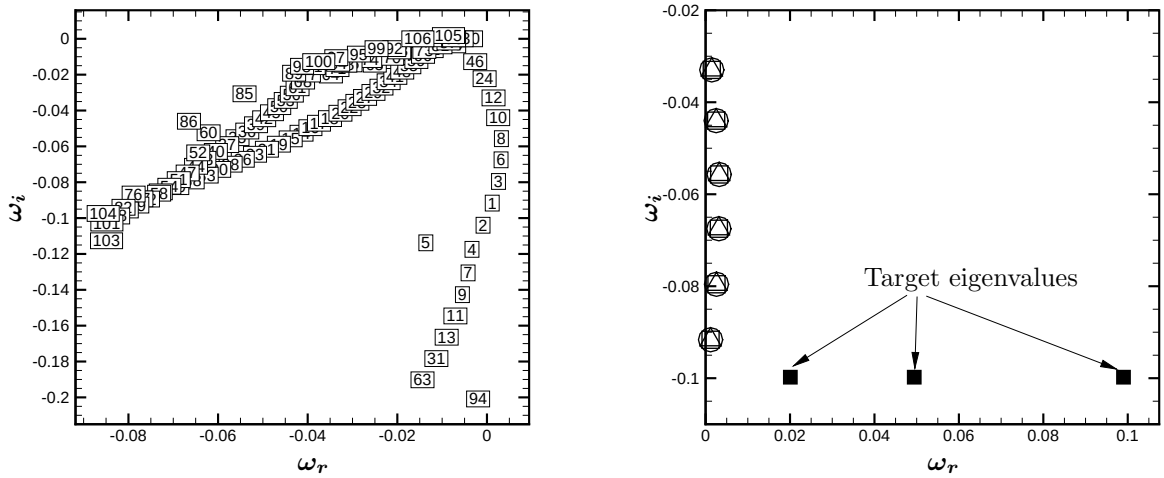

(a) (b)

Figure 3.8: (a) Eigenvalue spectrum for the diffuser obtained with a target eigenvalue of $(\omega_r, \omega_i) = (0.02, -0.1)$; (b) unstable region of the eigenspectrum obtained using different target eigenvalues $\square$ $(0.02, -0.1)$, $\triangle$ $(0.05, -0.1)$ and $\bigcirc$ $(0.1, -0.1)$.

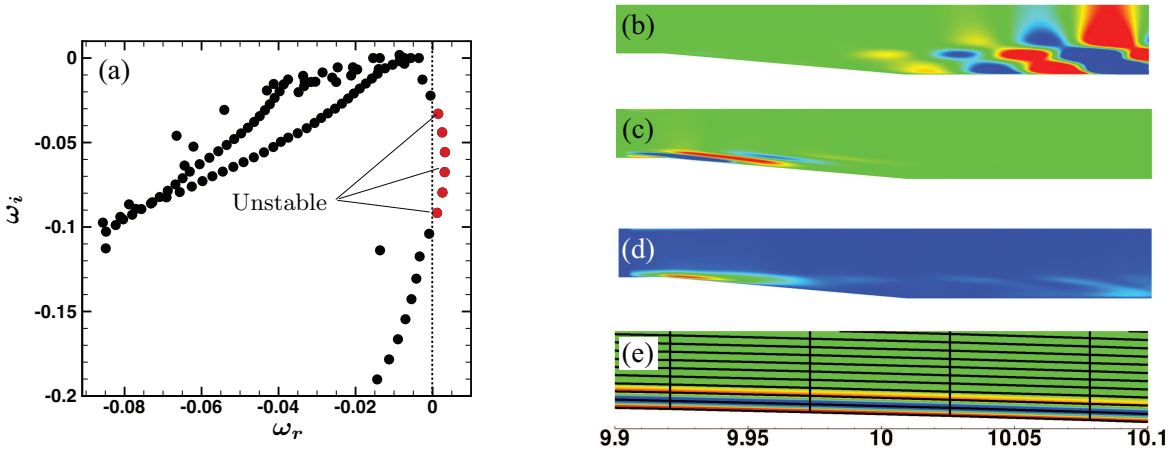

Figure 3.9: (a) The eigenspectrum for the Mach 0.65 equilibrium baseflow in the diffuser; (b) forward eigenmode, Real($\widehat{\rho u}$); (c) adjoint eigenmode, Real($\widehat{\rho u}^\dagger$); (d) wavemaker as defined by (3.6) and (e) near-wall zoom of the adjoint eigenmode.

3.3.5 Optimization

To demonstrate the optimization procedure, we consider the case of mass control with the forcing based on different feedbacks – density (ρ), streamwise momentum (ρu), cross-stream momentum (ρv) and total energy (ρE). The optimization is applied for control of the most unstable eigenmode. The objective of the optimization procedure is to minimize Re($\delta\omega$), thereby rendering the eigenmode less unstable. Figs. 3.10 (c), (d), (e) and (f) show the optimization history of the trust-region-reflective method for the different cases. The optimization procedure converged to the same final result for different initial values of the parameters. Figs. 3.10(a) and (b) show the shape and location of the actuation region for linear feedback forcing for different control-feedback pairs. This means that depending on the type of control and the feedback variable being sensed, the most effective location of actuating the flow will differ. Fig. 3.11 shows the control effectiveness (maximal shift in Re(ω)) based on the linear theory for different control-feedback pairs. It can be seen that the control effectiveness is dependent on the specific control-feedback pair chosen. But these quantities are predicted by the linear theory (omitting the effect of higher order terms) for unit amplitude ($\alpha = 1$) of control. For what range of control amplitudes the predictions are valid and how the higher order terms affect the predictions of the linear theory are described in Section 3.3.10.

3.3.6 Global Stabilization

To study the effect of increased control gain on the system, consider ρ–ρ control-feedback, as specified via $\tilde{\boldsymbol{C}}$ in (2.12). The global eigenanalysis of the closed loop system $\boldsymbol{A} + \alpha\boldsymbol{C}$ was performed with different values of

the gain α to obtain the range of values for which the system was globally stabilized (Fig. 3.12). Although the control was developed targeting the most unstable eigenvalue there is "parasitic" movement of other eigenvalues as well. In general, such a parasitic movement of eigenvalues need not be favorable. Since the estimate for the eigenvalue shift, $\delta\omega$, given by (2.13) is linear in the coefficients c_{ij} (a result that follows from assuming $\delta\boldsymbol{A} = \alpha\boldsymbol{C}$ is suitably small so that products of perturbed quantities can be neglected), the actual eigenvalue shift as $\boldsymbol{A}$ is perturbed to $\boldsymbol{A} + \alpha\boldsymbol{C}$ will begin to differ significantly from that obtained from the first order structural sensitivity analysis of (2.13); namely, the spectrum of $\boldsymbol{A} + \alpha\boldsymbol{C}$ is approximated by the spectrum of $\boldsymbol{A}$ plus a correction $\delta\omega$. It can be seen that for low values of control gain, the eigenspectrum tends to shift towards the left hand plane (LHP) and for this flow achieves complete stabilization; for further increase in α, some of the eigenvalues return to the right hand plane (RHP). Global stability is achieved for $0.105 < \alpha_{\text{stable}} < 0.108$, whereas the linear estimate for the minimum control gain for stabilizing the most unstable eigenvalue was $\alpha = 0.32$. As a consequence of this reversal of the eigenspectrum shift, there exists only a range of the control gain α for which global stabilization can be achieved even in just the linear system.

It should be noted that there are numerous actuator-sensor combinations that include single as well as multiple control(s)-feedback(s) that could be developed using the algorithm. For the present flow, other feedback combinations using mass control were analyzed as well. The root-locus diagram for the cases ρ-ρu, ρ-ρv and ρ-ρE are shown in Figs. 3.13 (a), (b) and (c) respectively. In the linear regime of structural sensitivity, the controller with maximum flexibility is the one that utilizes the full potential of the control matrix $\boldsymbol{C}$. Such an actuator can be obtained by performing an unconstrained optimization by optimizing over all coefficients c_{ij} of the control matrix $\boldsymbol{C}$. For this case, we find that the estimated best actuator is, to within a constant,

$$\tilde{\boldsymbol{C}}_{\text{unconstrained}} = \begin{bmatrix} 1 & -1 & -1 & 1 \\ -1 & 1 & 1 & -1 \\ 1 & -1 & -1 & 1 \\ -1 & 1 & -1 & -1 \end{bmatrix}. \tag{3.7}$$

The root-locus diagram for this controller is shown in Fig. 3.13(d). It can be seen that none of the above combinations could globally stabilize the system. The eigenspectrum shift, due to non-linearity, pushes some of the eigenvalues back into the unstable regime. The '$\times$' mark in Fig. 3.13, and all subsequent root-locus diagrams, indicates the location in the eigenspace at which the error between the real parts of the predicted (from structural sensitivity) and the actual computed eigenvalues for a given control gain α, reaches 1%, ie.

Simulation ID	α	Global Stability
1	0.05	Unstable
2	0.105	Stable
3	0.3	Unstable

Table 3.6: Direct numerical simulations to study the effect of control on vortex shedding.

$[(\omega_r)_{\text{predicted}} - (\omega_r)_{\text{computed}}]/(\omega_r)_{\text{predicted}} = 0.01$, where $(\omega_r)_{\text{predicted}} = (\omega_r)_{\text{uncontrolled}} + \delta\omega_{\text{structural sensitivity}}$.

3.3.7 Control of Vortex Shedding

To confirm applicability to the actual, nonlinear flow, three different simulations were conducted with the same initial condition: the equilibrium baseflow perturbed with the most unstable eigenmode with the perturbation amplitude in the non-linear regime (∼5% of maximum amplitude). The actuation used $\rho - \rho$ control-feedback. The control forcing term appears in the continuity equation as,

$$\frac{\partial \rho}{\partial t} = \tilde{\boldsymbol{R}}_\rho(\boldsymbol{Q}) + \alpha e^{-(x-x_0)^2/\ell_x^2 - (y-y_0)^2/\ell_y^2}(\rho - \rho_e), \tag{3.8}$$

where ρ_e is the steady baseflow density. The simulations performed and the observed system character corresponding to the actuator are given in Table 3.6. We define the total perturbation kinetic energy in the system as $E(t) = \frac{1}{2}\int_{\mathcal{V}}[u'(t)^2 + v'(t)^2]\, d\mathcal{V}$. The control objective, $E(t)/E(0)$, is used to quantify the deviation of the system from the baseflow. Fig. 3.14 shows the eigenspectrum and the unsteadiness quantification for the controlled flow for different values of the control gain. It can be seen that the control gain within the global stabilization window ($0.105 < \alpha < 0.108$) suppresses the vortex shedding downstream of the diffuser completely, whereas actuation with a gain value outside the stabilization window amplifies the initial perturbation energy of the system. The present Reynolds number was selected to illustrate this fundamental change of behavior. It is noteworthy that other control-feedback methods can be developed with the present algorithm; however, identifying all such combinations was not part of the present work.

3.3.8 More Challenging-to-control Configurations

The domain length and Reynolds number of the diffuser example were such that the control could completely suppress instabilities and stabilize the flow as simulated in the corresponding DNS. Of course, such efficacy is likely out of the question for higher Reynolds numbers and longer domains. Indeed the information contained with the spectrum of $\boldsymbol{A} + \alpha\boldsymbol{C}$, as a function of L_x and Re, could be used to estimate the degree to which complete stabilization could be achieved. We choose to demonstrate the effect of these parameters by

performing flow control for the following two additional cases for comparison. In the first case the Reynolds number is held fixed at $Re = 250$ but the domain length is increased 50% to $L_x = 180\delta$. In the second case the domain length remains at $L_x = 120\delta$ but the Reynolds number is increased to 350. We further show that the ability to rationally select actuator/sensor pairs, and locate them, is robust to these changes.

Longer Domain

To study the effect of the domain length, a steady baseflow was computed for the extended domain with $L_x/\delta = 180$ at $Re = 250$, and the results were compared to those from the original domain with $L_x/\delta = 120$. Fig. 3.16(a) shows that the unstable and least stable branch of the eigenspectrum is preserved for the short and long domains, but the long domain, on account of having a longer shear layer, supports more unstable modes (Fig. 3.17(a)). The controllability analysis for $\boldsymbol{A} + \alpha\boldsymbol{C}$ was performed for different values of the control gain α for the long domain using the same control-feedback ρ-ρ type with which global stabilization was observed for the short domain. Although the flow could not be globally stabilized for the longer domain, a significant reduction of the growth rate was observed for the unstable eigenvalues ($\approx 50\%$ for the most unstable eigenvalue) (Fig. 3.17(b)). It is well recognized that the global modes are sensitive to the domain size (Nichols & Lele, 2011), so we anticipate the spectrum to have changed in this case, and streamwise decorrelation makes control over the full domain by localized actuation a fundamentally more challenging problem. Still the most unstable eigenvalue targeted by the control is suppressed and the overall flow rendered less amplifying by the informed control. We note that the actuator placement is essentially unchanged, as shown in Fig. 3.16(b). Hence, the type of localized feedback control for a real, physical flow of this configuration may still depend on the type of outlet/length of the domain encountered by the flow downstream of separation.

Higher Reynolds Number

A steady baseflow was computed at $Re = 350$ for the short domain and the results were compared with the case at $Re = 250$. Fig. 3.18(a) shows the comparison of the eigenspectrum for the two baseflows. The effect of increasing the Reynolds number is qualitatively similar to that of the long domain at $Re = 250$, with more unstable eigenvalues and higher growth rates. Fig. 3.18(b) shows the effect of increase of the control gain α for the ρ–ρ control-feedback where it can be seen that the flow cannot be globally stabilized, but a significant reduction in the growth rate is obtained for all the unstable eigenvalues. The control was also performed using the actuator developed by unconstrained optimization as described in Section 3.3.6. The root-locus diagram (Fig. 3.19) shows that the reversal of the eigenspectrum shift occurs within a short range

of the control gain ($0 \leq \alpha \leq 0.02$) and hence global stabilization could not be achieved in this case as well.

The conclusion is that the complete suppression of instabilities is likely out of the question for higher Reynolds numbers and longer domains. Still, the present technique provided informed actuation that suppresses the instabilities even in these cases, though the flow is not, of course, fully stabilized.

3.3.9 Verification of Growth Rate using DNS

In this section, we verify the consistency of the global eigenvalue solver with the DNS. The steady baseflow obtained from the SFD technique was perturbed with the most unstable eigenmode of the system, and the growth rate (ω_r) from the DNS was compared with that predicted by the linear stability analysis from the eigenvalue solver. The amplitude of the initial perturbation was 10^{-7} so as to make sure that the initial growth is within the linear regime. At $t = 0$, we have $\boldsymbol{Q}'(\boldsymbol{x}, 0) = \widehat{\boldsymbol{Q}_{\boldsymbol{r}}}(\boldsymbol{x})$. The initial condition for the perturbed simulation is

$$\boldsymbol{Q}(\boldsymbol{x}, 0) = \boldsymbol{Q}_{\text{steady}}(\boldsymbol{x}) + \widehat{\boldsymbol{Q}_{\boldsymbol{r}}}(\boldsymbol{x}). \tag{3.9}$$

The simulation was carried out until nonlinear effects became significant and vortex shedding was observed downstream of the diffuser. Fig. 3.20 shows the comparison of the initial growth rate for all the conservative variables obtained from the DNS with that predicted by the linear stability analysis. The good quantitative comparison shows the consistency of the eigenvalue solver and the DNS. Fig. 3.21 shows the growth rate obtained from the DNS when nonlinear effects become significant. It can be seen that the system exhibits a linear regime until perturbations reach $\sim 10^{-2}$.

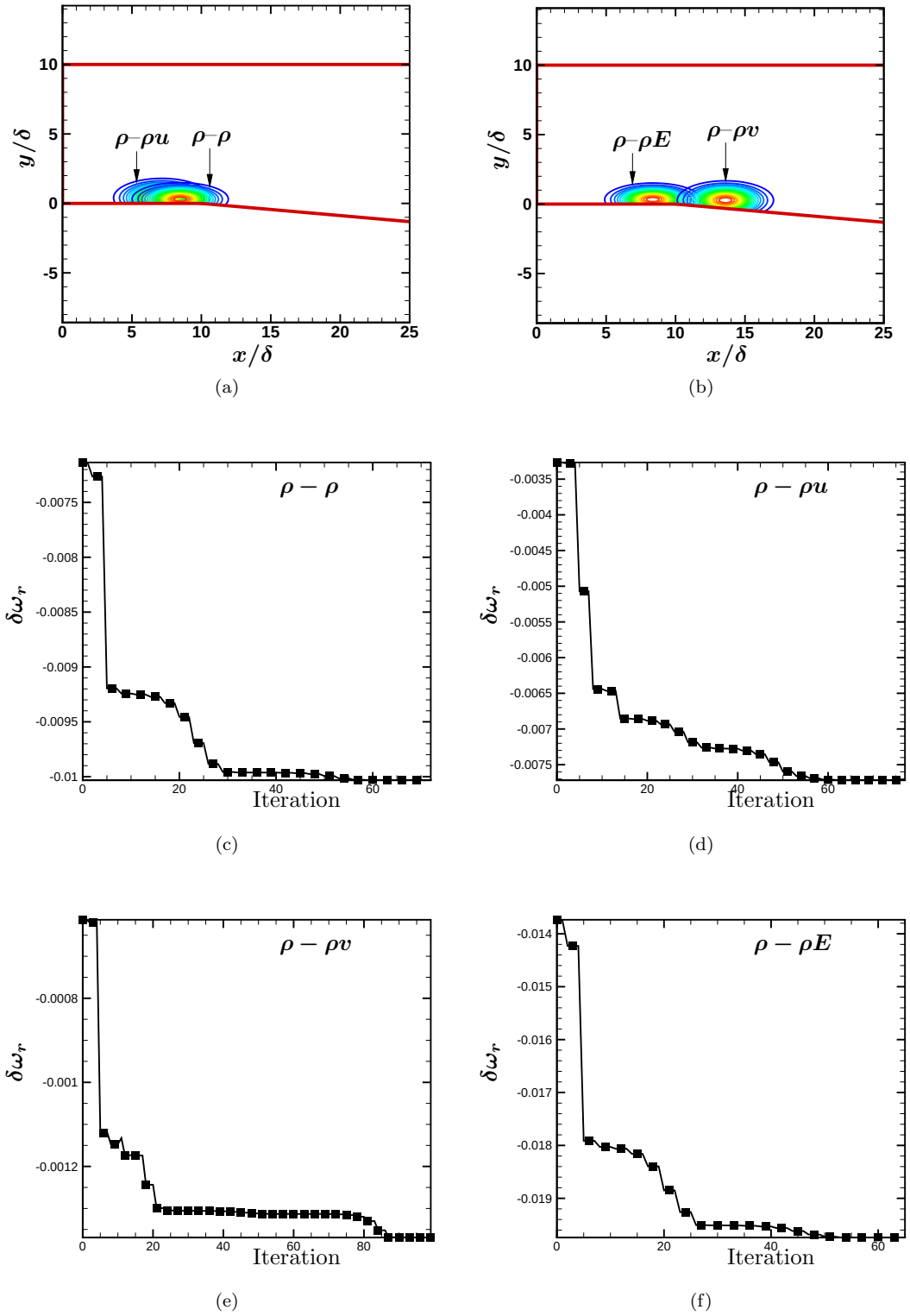

Figure 3.10: Shape and location of the wavemaker for ρ control for different control-feedback pairs: (a) $\rho-\rho$ and $\rho-\rho u$, (b) $\rho-\rho v$ and $\rho-\rho E$. Optimization history for different control-feedback pairs: (c) $\rho-\rho$, (d) $\rho-\rho u$, (e) $\rho-\rho v$ and (f) $\rho-\rho E$.

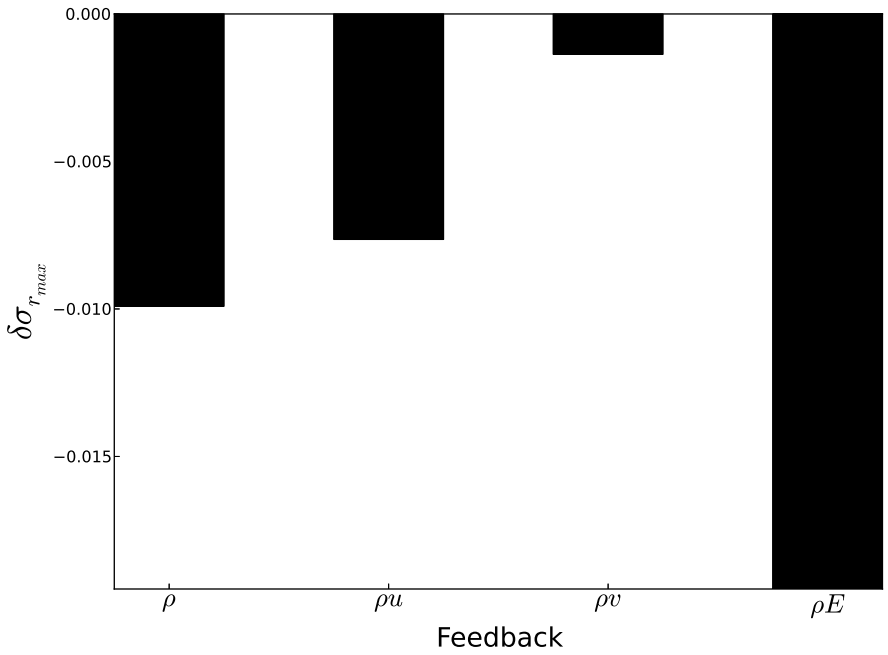

Figure 3.11: Comparison of control effectiveness based on linear theory for mass control of the most unstable eigenmode with different control-feedback pairs.

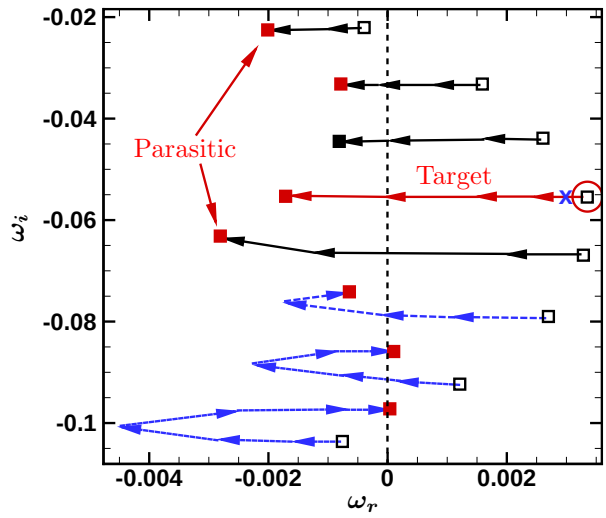

Figure 3.12: The eigenspectrum shift as a function of the control gain α: ⇢ show the locus of eigenvalues that have unfavorable shift. The arrows point in the direction of increasing control gain from $\alpha = 0.0$ to 0.108. The controlled eigenvalue is circled by ○. The open symbols (□) show the uncontrolled eigenspectrum.

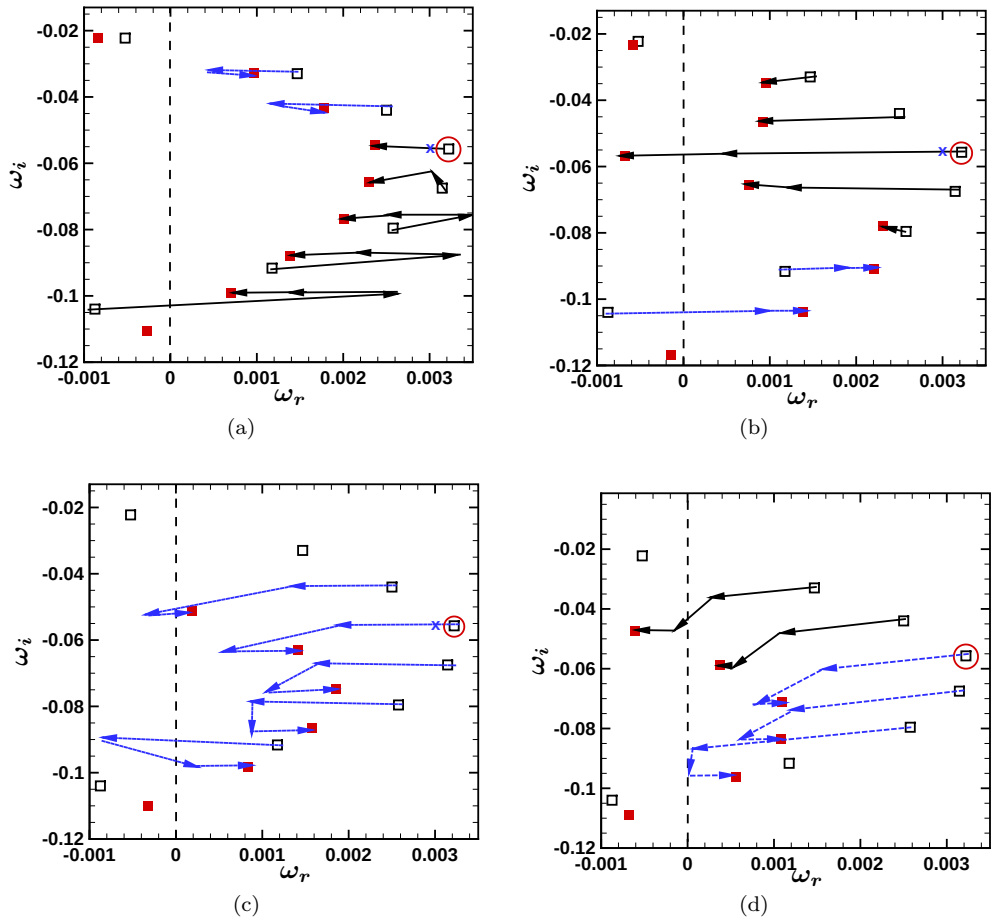

Figure 3.13: The eigenspectrum shift as a function of the control gain α for mass control with different feedback combinations: (a) $\rho - \rho u$ (b) $\rho - \rho v$ (c) $\rho - \rho E$, (d) unconstrained optimization. ⇢ show the locus of eigenvalues that have unfavorable shift. The arrows point in the direction of increasing control gain. The controlled eigenvalue is circled by ○. The open symbols (□) show the uncontrolled eigenspectrum.

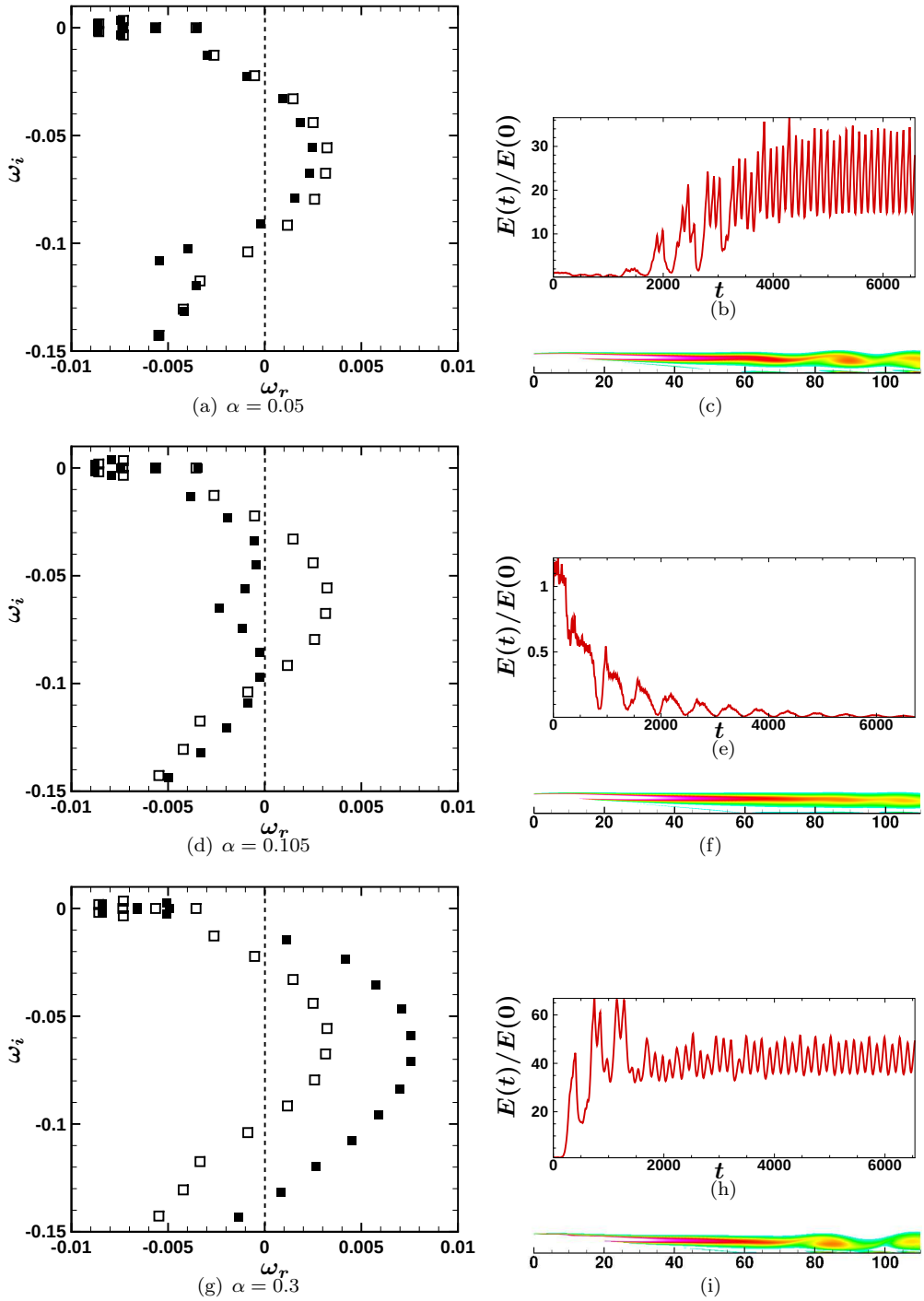

(a) $\alpha = 0.05$ (b) (c)

(d) $\alpha = 0.105$ (e) (f)

(g) $\alpha = 0.3$ (h) (i)

Figure 3.14: (a, d, g) Eigenspectrum: □ uncontrolled and ■ controlled. (c, f, i) Contours of instantaneous vorticity (b, e, h) $E(t)/E(0)$ for different control gains.

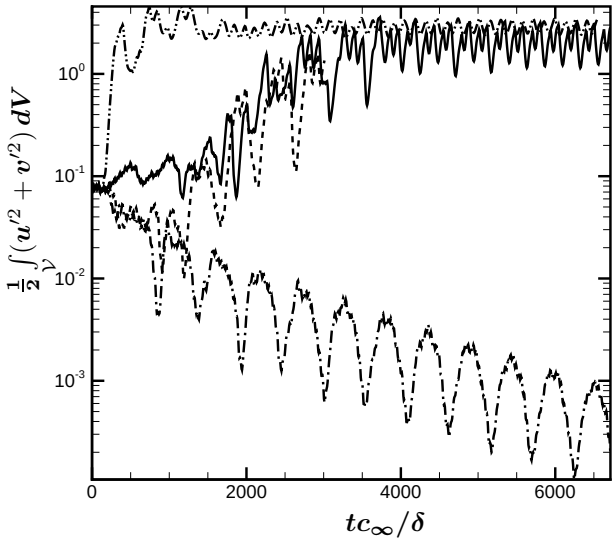

Figure 3.15: Total perturbation kinetic energy in the domain for the — baseline, −− controlled flow with α = 0.05, — · — $\alpha = 0.105$, and — ·· — $\alpha = 0.3$.

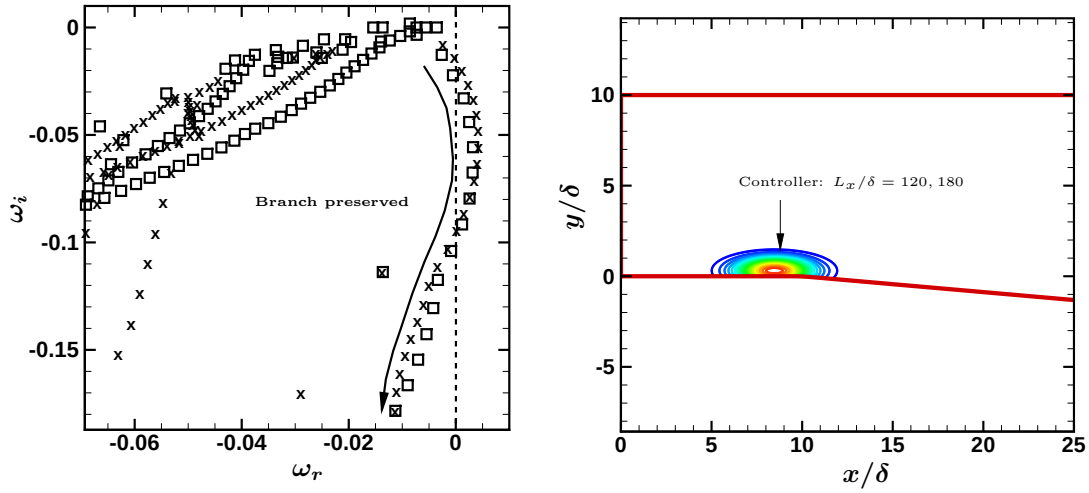

(a) (b)

Figure 3.16: (a) Eigenspectrum for the short and long domains at $Re = 250$: $L_x/\delta = 120$ (□); $L_x/\delta = 180$ (×). (b) The controller for the short and long domains almost overlap.

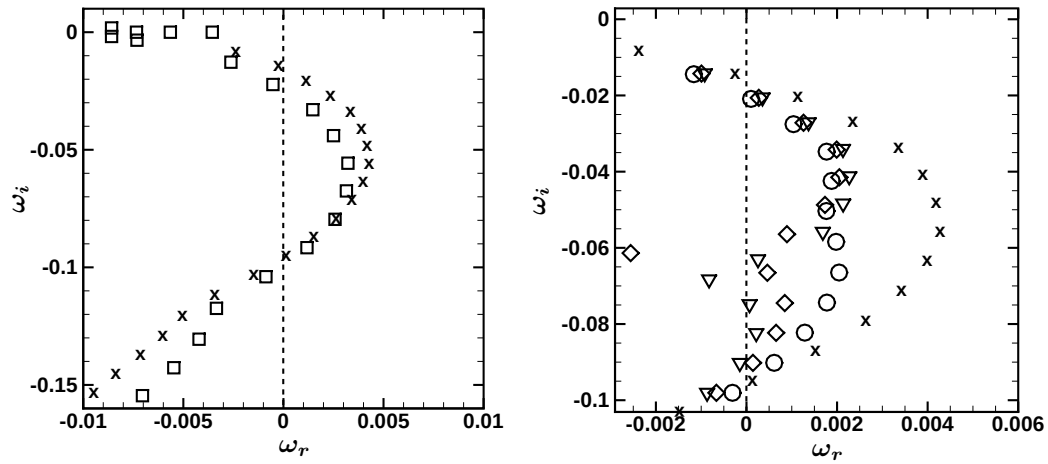

(a) (b)

Figure 3.17: (a) Eigenspectrum for the short and long domains at $Re = 250$: $L_x/\delta = 120$ ($\square$); $L_x/\delta = 180$ ($\times$). (b) Effect of the control gain (α) on the eigenspectrum with $\rho - \rho$ control-feedback for the long domain at $Re = 250$: Uncontrolled ($\times$); $\alpha = 0.105$ ($\bigtriangledown$); $\alpha = 0.11$ ($\diamond$) and $\alpha = 0.12$ ($\bigcirc$).

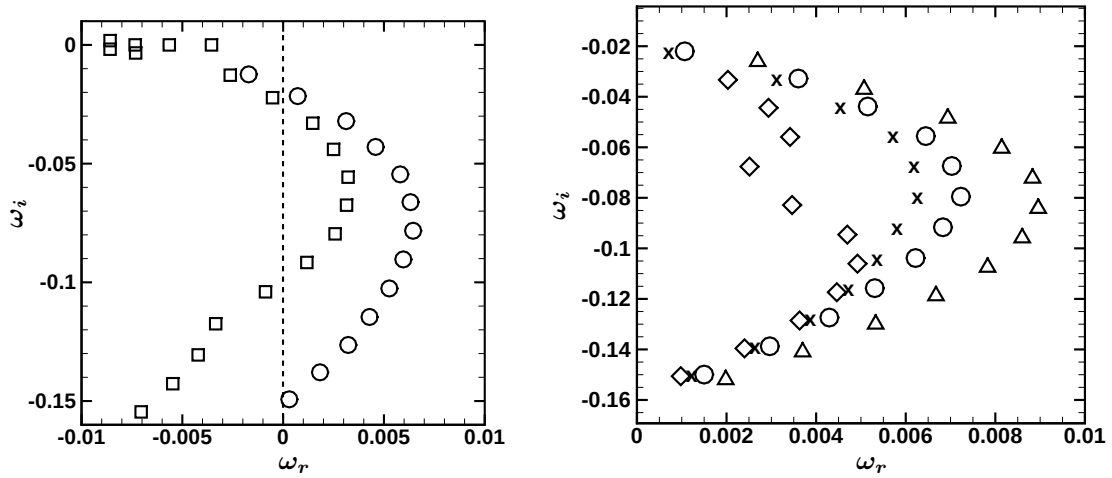

(a) (b)

Figure 3.18: Eigenspectrum for the short domain at two different Reynolds numbers: $Re = 250$ ($\square$); $Re = 350$ ($\bigcirc$). (b) Effect of the control gain (α) on the eigenspectrum with $\rho - \rho$ control-feedback for the short domain at $Re = 350$: Uncontrolled ($\bigcirc$); $\alpha = 0.05$ ($\times$); $\alpha = 0.10$ ($\diamond$) and $\alpha = 0.20$ ($\bigtriangleup$).

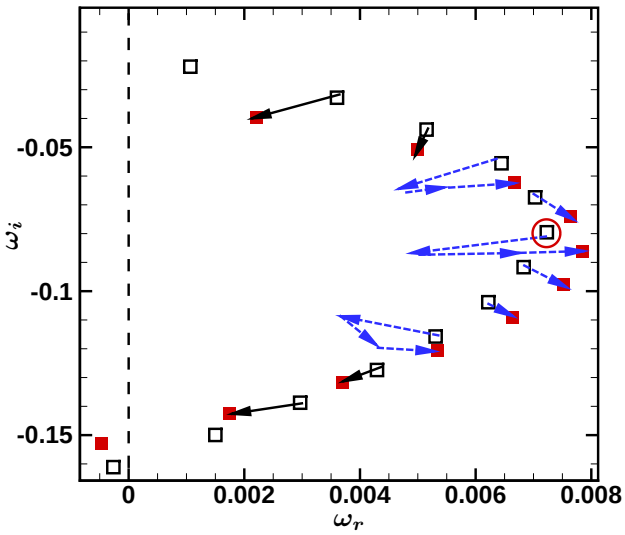

Figure 3.19: Effect of the control gain (α) on the eigenspectrum with for the unconstrained actuator for the baseflow at $Re = 350$ ($0 \leq \alpha \leq 0.02$). ⇢ show the locus of eigenvalues that have unfavorable shift. The arrows point in the direction of increasing control gain. The controlled eigenvalue is circled by ○. The open symbols (□) show the uncontrolled eigenspectrum.

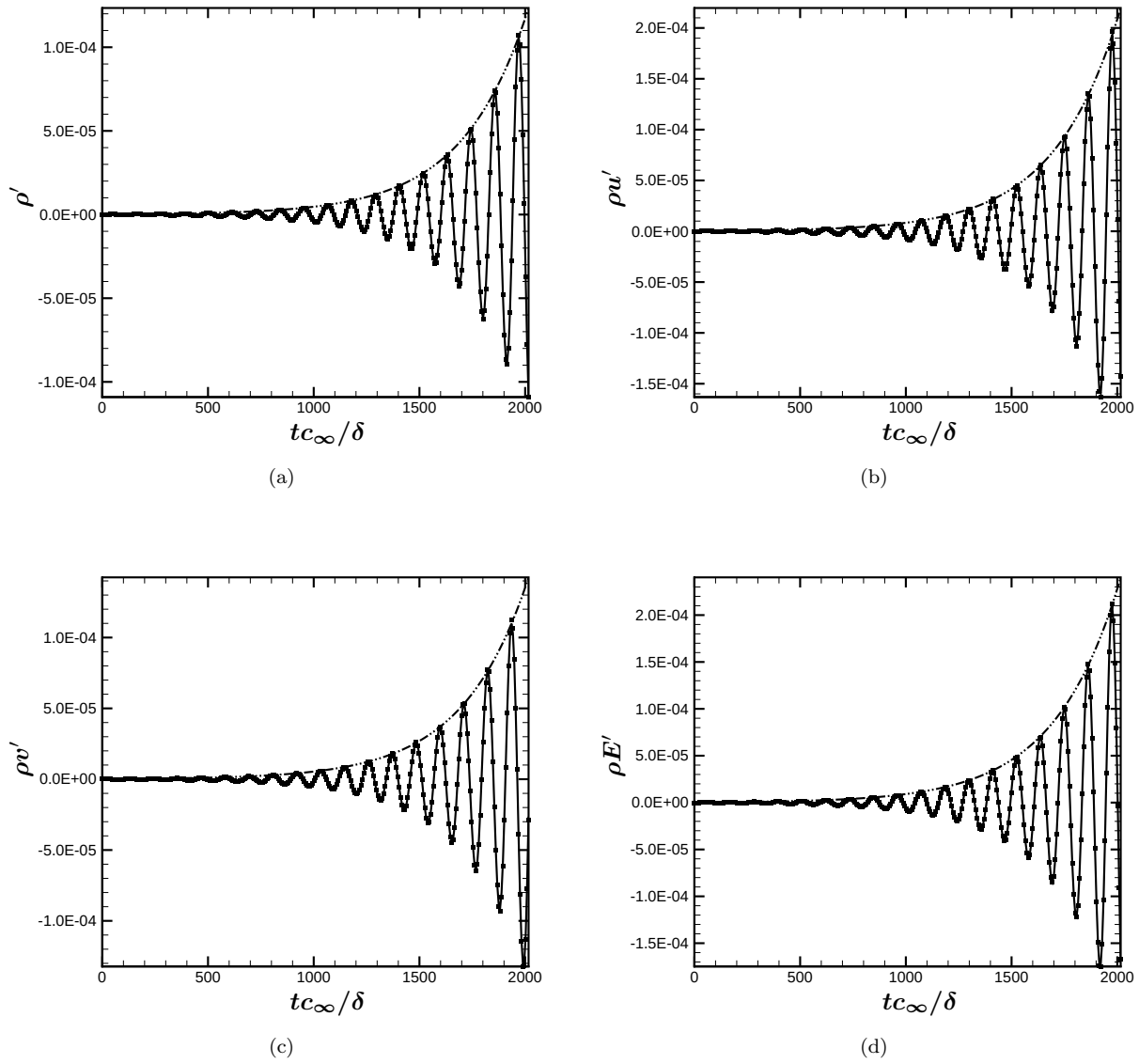

Figure 3.20: Comparison of linear theory with DNS : — linear theory, ■ DNS, — ·· — envelope from linear theory ($\omega_r = 0.00322$).

3.3.10 Effect of Second Order Terms

Since (2.13) is linear, multiplying $\delta \boldsymbol{L}$ by a constant factor (say α) can effect a shift of $\alpha \times \delta\omega$ in the eigenvalue. This would mean that linear feedback forcing could be used to shift an eigenvalue to any desired location in the complex plane by adjusting α, which is physically meaningless. Such an arbitrary movement of

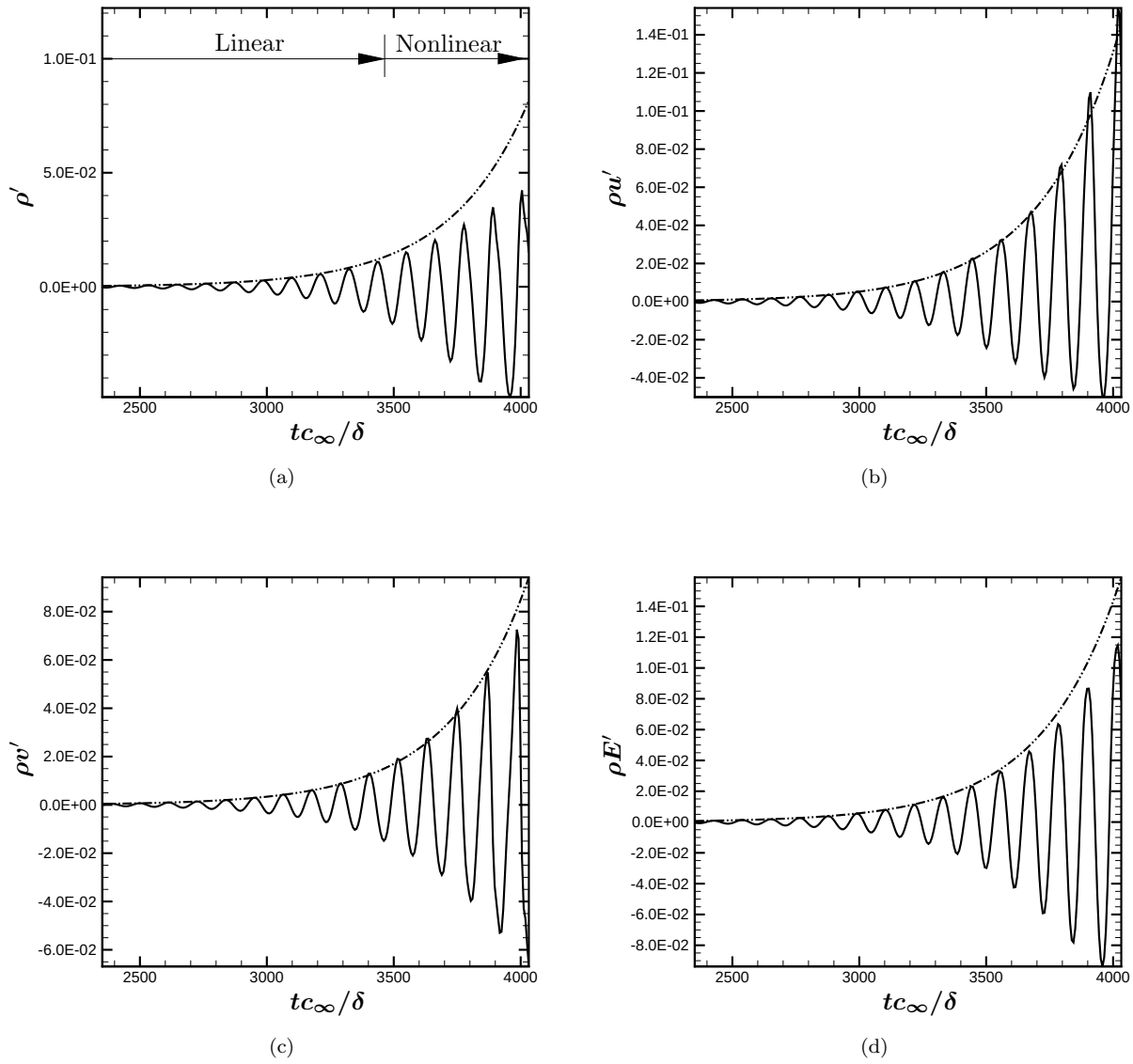

Figure 3.21: Comparison of linear theory with DNS (nonlinear regime): — DNS, — ·· — envelope from linear theory ($\omega_r = 0.00322$).

eigenvalues cannot be done since we obtained the eigenshift from

$$\widehat{\boldsymbol{Q}}^{\dagger\,\mathrm{T}}\boldsymbol{V}(\delta\boldsymbol{L}-\delta\omega\boldsymbol{I})\widehat{\boldsymbol{Q}}+\underbrace{\widehat{\boldsymbol{Q}}^{\dagger\,\mathrm{T}}\boldsymbol{V}(\delta\boldsymbol{L}-\delta\omega\boldsymbol{I})\delta\widehat{\boldsymbol{Q}}}_{\text{Second order term}}=0,$$

by discarding the second order term. As α becomes large, the nonlinear term becomes more significant and the linear analysis would no longer hold good. The actual eigenvalue, which is computed using the eigenvalue solver, tends to differ from the predicted eigenvalue. Here we analyze the error in the predicted

and computed eigenvalues to obtain an estimate of the maximum eigenshift that can be obtained for a given eigenvalue. The analysis is done for the most unstable eigenmode for mass control and different control-feedback pairs. To find the shifted eigenvalue from the eigensolver, a target eigenvalue of $\omega_{\text{target}} = \omega + \alpha\delta\omega$ is used as the guess, and the solver converges to the eigenvalue closest to the specified target. Figs. 3.22(a) and (b) show the percentage error (E) in the real and imaginary parts of the most unstable eigenvalue for different control-feedback pairs. The $E - \alpha$ plot shows a power law relationship with slope ~ 2. The error in the real part of the eigenvalue is larger compared to the imaginary part and also depends on the control-feedback pair.

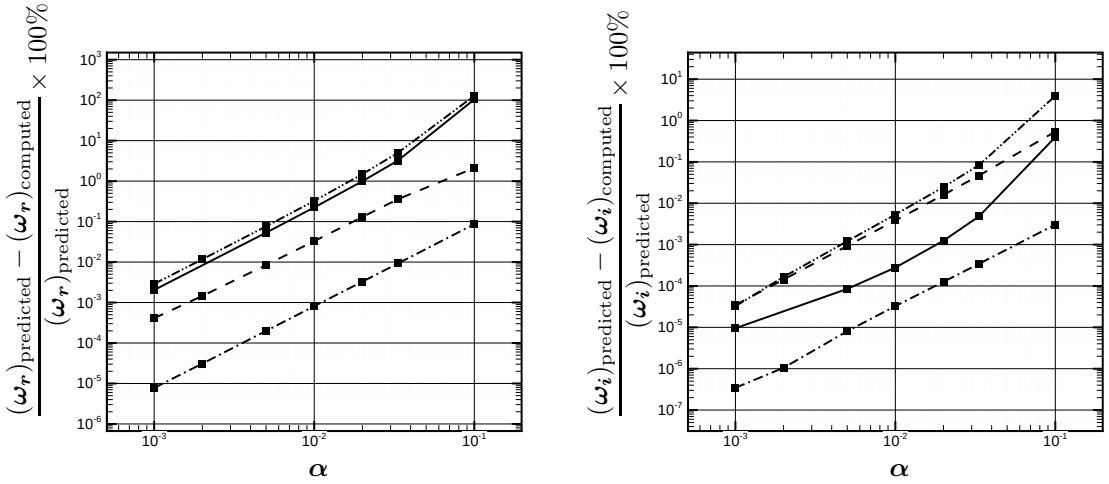

(a) (b)

Figure 3.22: Error in the predicted and computed eigenvalues with ρ control and different control-feedback pairs for the most unstable eigenmode (— $\rho-\rho$, — — $\rho-\rho u$,—·— $\rho-\rho v$, —··— $\rho-\rho E$) for (a) $\omega_r = \mathcal{R}(\omega)$ and (b) $\omega_i = \mathcal{I}(\omega)$.

3.4 Optimal Transient Growth

For a globally stable system, it is possible to obtain perturbation growth for a finite period of time by a particular superposition of the global modes. The basic idea behind optimal transient growth is to define a measure of perturbation energy $E(t)$ (Schmid & Henningson (2000), Nichols *et al.* (2009)) and to maximize the ratio $E(t)/E(t=0)$. The initial condition that produces the optimal response at a given time t can also be obtained using this procedure. The non-normality of the linear operator, which means the global modes of the system are non-orthogonal, allows us to find a set of coefficients to obtain an optimal linear superposition of the basis of the system, which is an optimal initial condition for obtaining transient growth for a finite period of time. If the system is globally stable, the growth reaches a maximum and then decays

with time.

3.4.1 Formulation

We define a measure of the perturbation energy of the system as

$$E(t) = \frac{1}{2} \int_{\mathcal{V}} (\widehat{u}(t)\widehat{u}^*(t) + \widehat{v}(t)\widehat{v}^*(t))\, dV \tag{3.10}$$

where '*' denotes the complex conjugate. In matrix form, this can be written as (N_g is total number of grid points, N_m is the number of the global modes in the chosen basis)

$$E = \frac{1}{2} \begin{bmatrix} \widehat{u}_1^*(t) \\ \widehat{v}_1^*(t) \\ \widehat{u}_2^*(t) \\ \widehat{v}_2^*(t) \\ \vdots \\ \widehat{u}_{N_g}^*(t) \\ \widehat{v}_{N_g}^*(t) \end{bmatrix}^T_{1\times 2N_g} \begin{bmatrix} (\Delta x \Delta y)_1 & & & & & & \\ & (\Delta x \Delta y)_1 & & & & & \\ & & \ldots & & & & \\ & & & (\Delta x \Delta y)_{N_g} & & & \\ & & & & (\Delta x \Delta y)_{N_g} & & \end{bmatrix}_{2N_g \times 2N_g} \begin{bmatrix} \widehat{u}_1(t) \\ \widehat{v}_1(t) \\ \widehat{u}_2(t) \\ \widehat{v}_2(t) \\ \vdots \\ \widehat{u}_{N_g}(t) \\ \widehat{v}_{N_g}(t) \end{bmatrix}_{2N_g \times 1} \tag{3.11}$$

Expanding the vectors in the above equation as a linear combination of the basis elements $M1, M2, \ldots, MN$, with the corresponding coefficients $k_1, k_2, \ldots, k_N$, we obtain

$$E = \frac{1}{2}\begin{bmatrix} k_1 e^{\omega_{M1}t} & k_2 e^{\omega_{M2}t} & \dots & k_N e^{\omega_{MN}t} \end{bmatrix}^*_{1\times N_m} \begin{bmatrix} \widehat{u}^*_{M1,1} & \widehat{v}^*_{M1,1} & \dots & \widehat{u}^*_{M1,N_g} & \widehat{v}^*_{M1,N_g} \\ \widehat{u}^*_{M2,1} & \widehat{v}^*_{M2,1} & \dots & \widehat{u}^*_{M2,N_g} & \widehat{v}^*_{M2,N_g} \\ \vdots & \vdots & \dots & \vdots & \vdots \\ \widehat{u}^*_{MN,1} & \widehat{v}^*_{MN,1} & \dots & \widehat{u}^*_{MN,N_g} & \widehat{v}^*_{MN,N_g} \\ \widehat{u}^*_{MN,1} & \widehat{v}^*_{MN,1} & \dots & \widehat{u}^*_{MN,N_g} & \widehat{v}^*_{MN,N_g} \end{bmatrix}_{N_m\times 2N_g} \tag{3.12}$$

$$\times \begin{bmatrix} (\Delta x\Delta y)_1 & & & & \\ & (\Delta x\Delta y)_1 & & & \\ & & \dots & & \\ & & & (\Delta x\Delta y)_{N_g} & \\ & & & & (\Delta x\Delta y)_{N_g} \end{bmatrix}_{2N_g\times 2N_g} \tag{3.13}$$

$$\times \begin{bmatrix} \widehat{u}_{M1,1} & \widehat{u}_{M2,1} & \dots & \widehat{u}_{MN,N_g} & \widehat{u}_{MN,N_g} \\ \widehat{v}_{M1,1} & \widehat{v}_{M2,1} & \dots & \widehat{v}_{MN,N_g} & \widehat{v}_{MN,N_g} \\ \vdots & \vdots & \dots & \vdots & \vdots \\ \widehat{u}_{M1,N_g} & \widehat{u}_{M2,N_g} & \dots & \widehat{u}_{MN,N_g} & \widehat{u}_{MN,N_g} \\ \widehat{v}_{M1,N_g} & \widehat{v}_{M2,N_g} & \dots & \widehat{v}_{MN,N_g} & \widehat{v}_{MN,N_g} \end{bmatrix}_{2N_g\times N_m} \begin{bmatrix} k_1 e^{\omega_{M1}t} \\ k_2 e^{\omega_{M2}t} \\ \vdots \\ k_3 e^{\omega_{MN}t} \end{bmatrix}_{N_m\times 1} \tag{3.14}$$

$$\tag{3.15}$$

which can be written as

$$E = \kappa^H (Q^H W Q)\kappa \tag{3.16}$$

A Cholesky decomposition of $Q^H W Q$ gives F such that

$$F^H F = Q^H W Q \tag{3.17}$$

which gives

$$E = (F\kappa)^H (F\kappa) \tag{3.18}$$

Define $G(t)$ to be the maximum amplification at time t from any initial condition q_0. Then

$$\begin{aligned} G(t) &= \max \frac{||q(t)||^2}{||q_0||^2} = \frac{||F\kappa(t)||^2}{||F\kappa_0||^2} && (3.19) \\ &= \frac{||Fe^{t\Sigma}\kappa_0||^2}{||F\kappa_0||^2} && (3.20) \\ &= \frac{||Fe^{t\Sigma}F^{-1}F\kappa_0||^2}{||F\kappa_0||^2} && (3.21) \\ &= ||Fe^{t\Sigma}F^{-1}||^2 && (3.22) \end{aligned}$$

This is the square of the largest singular eigenvalue of the matrix $Fe^{t\Sigma}F^{-1}(N_m \times N_m)$. The corresponding eigenvector $(N_m \times 1)$ will give the contribution of each of the global modes to the optimal initial condition to produce a given transient response at a given time t.

3.4.2 Optimal Initial Condition

The optimal transient growth is given by

$$\begin{aligned} G(t) = \frac{||F\kappa(t)||^2}{||F\kappa_0||^2} &= \frac{||F\kappa(t)||^H F\kappa(t)}{||F\kappa(0)||^H F\kappa(0)} && (3.23) \\ &= \frac{(Fe^{t\Sigma}\kappa(0))^H (Fe^{t\Sigma}\kappa(0))}{(F\kappa(0))^H (F\kappa(0))} && (3.24) \\ &= \frac{\kappa(0)^H (e^{t\Sigma})^H F^H F e^{t\Sigma}\kappa(0)}{(F\kappa(0))^H (F\kappa(0))} && (3.25) \end{aligned}$$

Now, we need to find the initial condition which produces the optimal response at some chosen time, T. The corresponding $\omega^2_{\max}(T) = G(T)$. ie.

$$G(T) = \frac{\kappa(0)^H (e^{T\Sigma})^H F^H F e^{T\Sigma}\kappa(0)}{(F\kappa(0))^H (F\kappa(0))} \tag{3.26}$$

From the definition of the singular eigenvalue problem, we have

$$(Fe^{T\Sigma}F^{-1})^H (Fe^{T\Sigma}F^{-1})X = \omega^2_{\max}(T)X \tag{3.27}$$

where X is the eigenvector corresponding to $\omega^2_{\max}(T)$.

If $X = F\kappa(0)$, then

$$(Fe^{T\Sigma}F^{-1})^H(Fe^{T\Sigma}F^{-1})F\kappa(0) = \omega^2_{\max}(T)F\kappa(0) \tag{3.28}$$

$$\tag{3.29}$$

Multiplying by $F\kappa(0)^H$ on both sides, we get

$$\begin{aligned}
(F\kappa(0))^H(Fe^{T\Sigma}F^{-1})^H(Fe^{T\Sigma}F^{-1})F\kappa(0) &= G(T)(F\kappa(0))^HF\kappa(0) && (3.30)\\
\kappa(0)^HF^H(F^{-1})^H(e^{T\Sigma})^HF^HFe^{T\Sigma}F^{-1}F\kappa(0) &= G(T)(F\kappa(0))^HF\kappa(0) && (3.31)\\
\kappa(0)^H(e^{T\Sigma})^HF^HFe^{T\Sigma}\kappa(0) &= G(T)(F\kappa(0))^HF\kappa(0) && (3.32)\\
& && (3.33)
\end{aligned}$$

which gives

$$\frac{\kappa(0)^H(e^{T\Sigma})^HF^HFe^{T\Sigma}\kappa(0)}{(F\kappa(0))^H(F\kappa(0))} = \omega^2_{\max}(T) = G(T) \tag{3.34}$$

$$\tag{3.35}$$

Hence, the coefficients $\kappa(0) = F^{-1}X$, where X is the eigenvector corresponding to $\omega^2_{\max}(T)$ gives $[k_1\ \ k_2\ \ \ldots\ \ k_N]$ to reconstruct the initial condition which gives the response $G(T)$ at time $t = T$.

3.4.3 Optimal Transient Growth - Steady Baseflow at $Re = 250$

The optimal transient response is computed for the steady baseflow at $Re = 250$ for the uncontrolled and controlled cases. The envelopes of the optimal transient response for the uncontrolled and controlled cases are shown in Fig. 3.23(a). Since the chosen controller globally stabilizes the flow, the optimal transient response decays after a finite period of time. Moreover, the optimal response of the controlled flow closely follows that of the uncontrolled flow but does not amplify it further.

The initial condition to obtain the optimal response at $t = 270$, which corresponds to the peak optimal response, is computed. Figs. 3.23(b) and (c) show the envelope of optimal response and the response for the chosen initial condition. Fig. 3.23(d) shows the contribution of the global modes to the optimal initial condition. The radii of the circles are proportional to the energy contribution of the corresponding global mode to the optimal initial condition. Fig. 3.24 shows the evolution of the optimal initial condition

corresponding to the optimal transient response at $t = 270$. It can be seen that the non-normal superposition of the global modes (to obtain the optimal initial condition) grows into a convective instability which travels downstream.

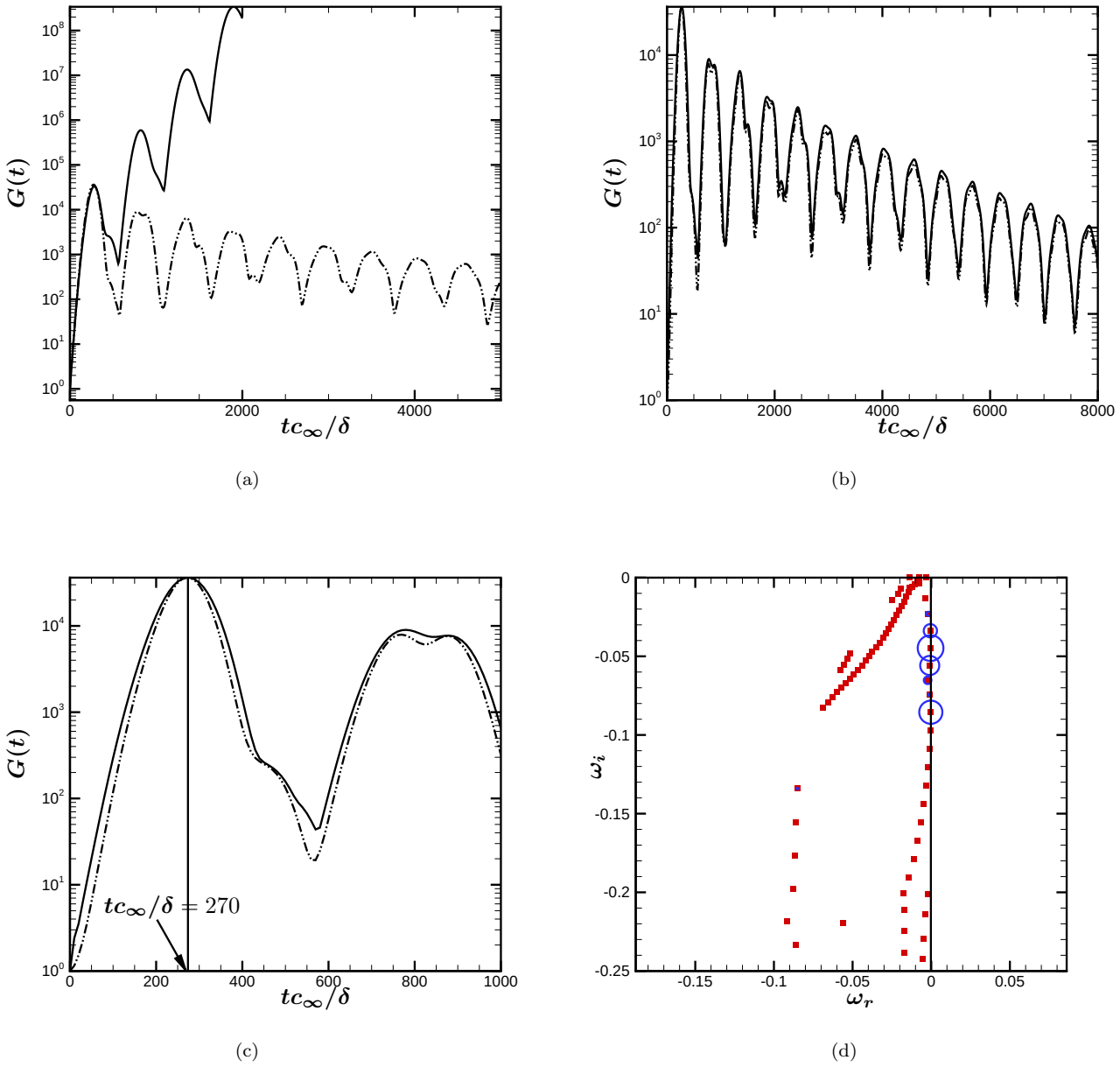

Figure 3.23: (a) Envelopes of optimal transient response at $Re = 250$ for the baseline (—) and controlled flow with $\alpha = 0.105$ (— ·· —); (b),(c) envelope (—) and optimal response (— ·· —) corresponding to $t = 100$; (d) eigenspectrum for the steady baseflow at $Re = 250$ with control ($\alpha = 0.105$) showing the contribution of different eigenmodes to the optimal initial condition to obtain optimal response at time $t = 270$ (the radii of the circles are proportional to the contribution of the corresponding eigenmode to the kinetic energy norm at $t = 0$).

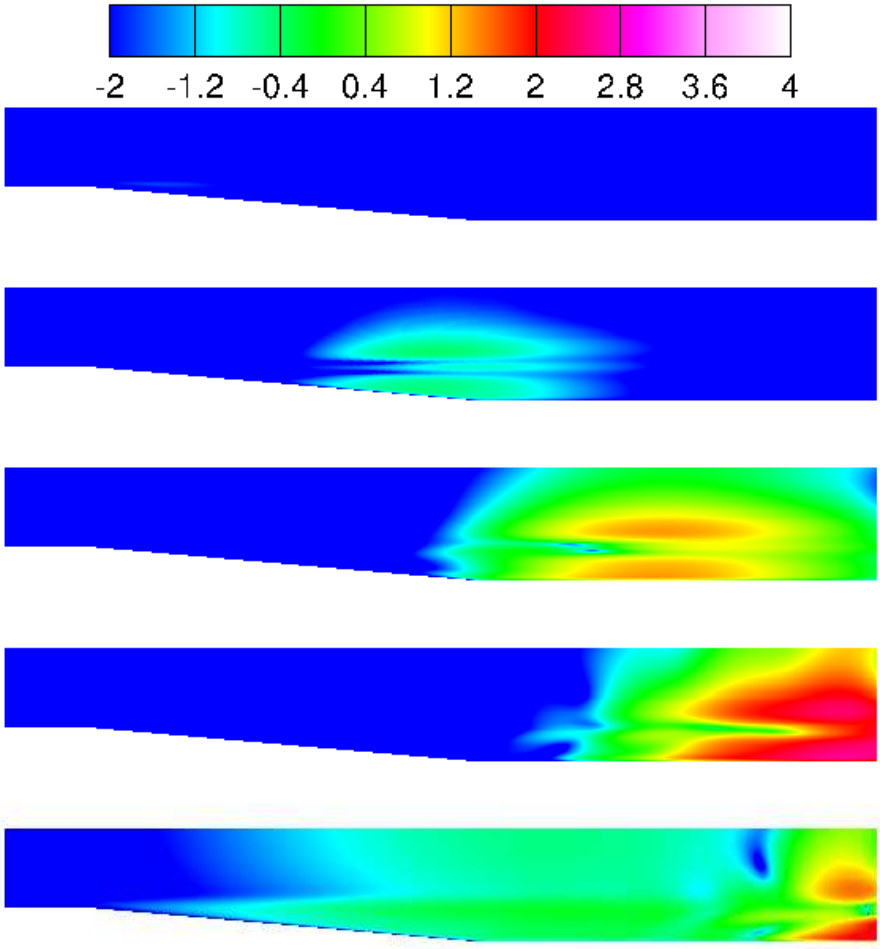

Figure 3.24: Evolution of the optimal initial condition to produce the optimal transient response at $t = 270$. Contours of $\log_{10}\left[\frac{1}{2}(u'^2 + v'^2)\right]$ are shown – top to bottom: $t = 0$, $t = 90$, $t = 180$, $t = 270$, $t = 360$.

Chapter 4

Noise Reduction of an Axisymmetric Mach 1.5 Jet

The active control strategy developed in Chapter 2 is now applied to reducing the noise of an axisymmetric Mach 1.5 jet. Section 4.1 describes the governing equations. Numerical methods are discussed in Section 4.2. The flow solutions and their eigenanalysis are detailed in Sections 4.3 and 4.4, respectively. Section 4.5 describes the projection of the flow dynamics onto the global modes, and optimal transient growth is described in Section 4.6. The controller development, results and analysis of noise controlled flows are given in Section 4.7.

4.1 Governing Equations

The compressible-fluid Navier–Stokes equations governing density, velocity and temperature, are solved in cylindrical polar coordinates with z, r and θ representing the axial, radial and azimuthal directions, respectively. The equations are non-dimensionalized with the nozzle radius R, the fluid density and temperature with the free-stream values, ρ_∞ and T_∞ respectively and the velocities with the free-stream speed of sound, c_∞ following a common approach (Salgado & Sandham, 2007). The Reynolds number is defined as $Re = c_\infty R/\nu$. The governing equations are

$$\left.\begin{aligned}
\frac{\partial\rho}{\partial t} + \left(V_r\frac{\partial\rho}{\partial r} + \frac{V_\theta}{r}\frac{\partial\rho}{\partial\theta} + V_z\frac{\partial\rho}{\partial z}\right) + \rho\left(\frac{\partial V_r}{\partial r} + \frac{V_r}{r} + \frac{1}{r}\frac{\partial V_\theta}{\partial\theta} + \frac{\partial V_z}{\partial z}\right) &= 0 \\
\rho\frac{\partial V_r}{\partial t} + \rho\left(V_r\frac{\partial V_r}{\partial r} + \frac{V_\theta}{r}\frac{\partial V_r}{\partial\theta} - \frac{V_\theta^2}{r} + V_z\frac{\partial V_r}{\partial z}\right) + \frac{1}{\gamma}\left(\rho\frac{\partial T}{\partial r} + T\frac{\partial\rho}{\partial r}\right) &= S_r \\
\rho\frac{\partial V_\theta}{\partial t} + \rho\left(V_r\frac{\partial V_\theta}{\partial r} + \frac{V_\theta}{r}\frac{\partial V_\theta}{\partial\theta} + \frac{V_rV_\theta}{r} + V_z\frac{\partial V_\theta}{\partial z}\right) + \frac{1}{\gamma}\left(\frac{\rho}{r}\frac{\partial T}{\partial\theta} + \frac{T}{r}\frac{\partial\rho}{\partial\theta}\right) &= S_\theta \\
\rho\frac{\partial V_z}{\partial t} + \rho\left(V_r\frac{\partial V_z}{\partial r} + \frac{V_\theta}{r}\frac{\partial V_z}{\partial\theta} + V_z\frac{\partial V_z}{\partial z}\right) + \frac{1}{\gamma}\left(\rho\frac{\partial T}{\partial z} + T\frac{\partial\rho}{\partial z}\right) &= S_z \\
\rho\frac{\partial T}{\partial t} + \rho\left(V_r\frac{\partial T}{\partial r} + \frac{V_\theta}{r}\frac{\partial T}{\partial\theta} + V_z\frac{\partial T}{\partial z}\right) + (\gamma-1)\rho T\left(\frac{\partial V_r}{\partial r} + \frac{V_r}{r} + \frac{1}{r}\frac{\partial V_\theta}{\partial\theta} + \frac{\partial V_z}{\partial z}\right) &= S_T
\end{aligned}\right\} \tag{4.1}$$

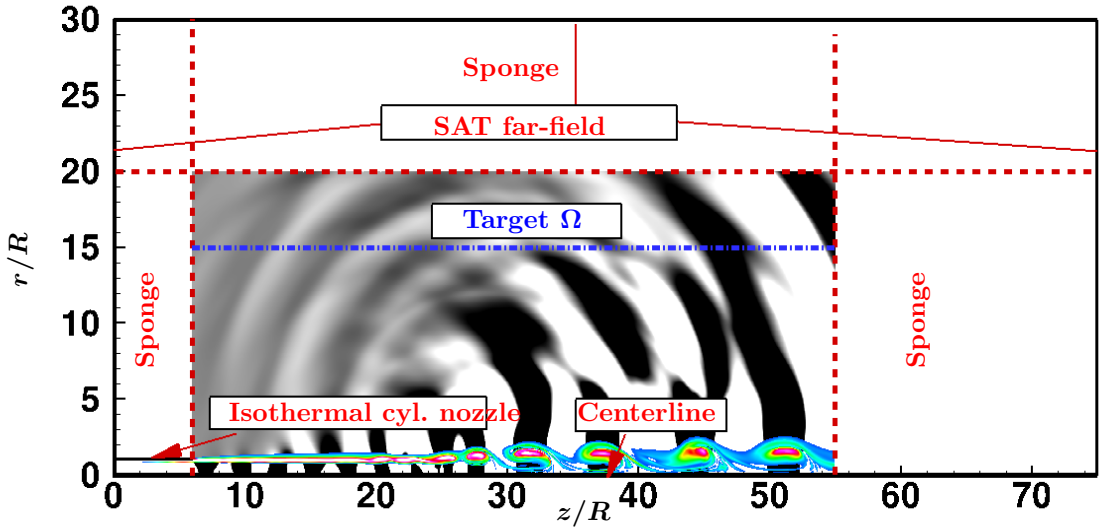

Figure 4.1: Computational domain and boundary conditions.

S_r, S_θ, S_z and S_T include all viscous and heat transfer effects (see Appendix D). A standard power law describes the temperature dependence of the fluid viscosity, μ, and thermal conductivity, κ as $\mu = \kappa = T^{2/3}$. The bulk viscosity is $\mu_B = \lambda + 2/3\mu = 0.6\mu$, where λ is the second coefficient of viscosity and the Prandtl number $Pr = \mu C_p/\kappa = 0.72$, where C_p is the specific heat at constant pressure. For this nondimensionalization, the equation of state is $p = \rho T$ and has been used in (4.1).

4.2 Numerical Methods

4.2.1 Nonlinear Flow Solver

The computational domain and the boundary conditions are shown in Fig. 4.1. The nozzle length and wall thickness are $L_{\text{nozzle}}/R = 6$ and $t_{\text{nozzle}}/R = 0.05$, respectively. The domain is discretized on a stretched, orthogonal mesh with $(N_z, N_r) = (4400, 640)$ points in the axial and radial directions. Derivatives are computed using 4-2 summation-by-parts finite-difference operators (Strand, 1994; Mattsson *et al.*, 2008), and fourth-order Runge–Kutta is used for temporal integration. To capture the weak shocks corresponding to slight deviations of perfect expansion due to the boundary layer in the nozzle, a shock-capturing scheme is implemented that adds dissipation via the normal transport coefficients μ, λ, and κ (Kawai *et al.*, 2010) (see Appendix F). Sponge zones (Freund, 1997; Bodony, 2006) are used at the domain boundaries to prevent spurious reflections into the domain. Navier–Stokes characteristic boundary conditions are used for the isothermal nozzle walls and non-reflecting boundary conditions using the Simultaneous-Approximation-

Term approach (Svärd *et al.*, 2007; Svärd & Nordström, 2008; Bodony, 2010) at the end of the sponge zones. The centerline singularity is treated by deriving conditions using symmetry and regularity conditions (Lewis & Bellan, 1990); see also Appendix D.2.

Eigenvalue Solver

The governing equations are linearized about the baseflow $\bar{\boldsymbol{Q}}$, and we assume a modal decomposition of the form

$$[\rho', V_r', V_\theta, V_z', T'] \quad = \quad \{\widehat{\rho}, \widehat{V_r}, \widehat{V_\theta}, \widehat{V_z}, \widehat{T}\}(r,z)e^{im\theta+\omega t}.$$

We obtain the discretized global eigenvalue problem as

$$\begin{aligned}\Big\{\omega \boldsymbol{I} \quad &+ \quad \boldsymbol{L_z^i}\frac{\partial\xi}{\partial z}\frac{\partial}{\partial\xi} + \boldsymbol{L_r^i}\frac{\partial\eta}{\partial r}\frac{\partial}{\partial\eta} + \frac{1}{Re\rho}\Big[\boldsymbol{L_z^v}\frac{\partial\xi}{\partial z}\frac{\partial}{\partial\xi} + \boldsymbol{L_r^v}\frac{\partial\eta}{\partial r}\frac{\partial}{\partial\eta} + \boldsymbol{L^v_{(1)zz}}\xi_z^2\frac{\partial^2}{\partial\xi^2} \\ &+ \quad \boldsymbol{L^v_{(2)zz}}\frac{\partial\xi_z}{\partial\xi}\xi_z\frac{\partial}{\partial\xi} + \boldsymbol{L^v_{(1)rr}}\eta_r^2\frac{\partial^2}{\partial\eta^2} + \boldsymbol{L^v_{(2)rr}}\frac{\partial\eta_r}{\partial\eta}\eta_r\frac{\partial}{\partial\eta} + \boldsymbol{L^v_{zr}}\xi_z\eta_r\frac{\partial^2}{\partial\xi\partial\eta} \\ &+ \quad \boldsymbol{L_{base}}\Big] + \boldsymbol{P^{-1}E_1T_r\Lambda_r^+T_r^{-1}}\eta_r + \boldsymbol{P^{-1}E_1T_z\Lambda_z^+T_z^{-1}}\xi_z\Big\}\widehat{\boldsymbol{Q}} = 0, \end{aligned} \tag{4.2}$$

where the $\boldsymbol{L}$s denote the discrete matrix operators and the superscripts 'i' and 'v' are used to differentiate the inviscid and the viscous operators respectively. $\boldsymbol{L}_{base}$ is the part of the global operator that does not contain any derivative operator. The linearization of the equations is done in a modular manner for the inviscid and viscous terms of each of the five equations separately and added to get the complete linearized Navier-Stokes operator. The terms in each of the coefficient matrices ($\boldsymbol{L}$s) are given in Table E.1–E.5 for the inviscid terms and in Table E.6–E.9 for the viscous terms. The verification of the eigenvalue solver for inviscid and viscous cases is given in Appendix C.

4.3 Baseflow Solution

The jet considered has Re = 2,000, $M_j = U_j/c_j = 1.5$, and $T_j/T_\infty = 0.6$. The momentum thickness of the nozzle exit boundary layer is $\theta/R = 0.01$ and the nozzle-wall temperature is $T_{\text{nozzle}}/T_\infty = 1$. Flow simulations provide two different solutions—an equilibrium and time-average— for $\bar{\boldsymbol{Q}}$.

For the equilibrium solution, which satisfies $\tilde{\boldsymbol{R}}(\boldsymbol{Q}_e) = 0$, we use a parallel shear layer as an initial condition and Selective Frequency Damping (SFD) (Åkervik *et al.*, 2006) to suppress the absolute instabilities so that the equilibrium solution satisfies $||\tilde{\boldsymbol{R}}(\boldsymbol{Q}_e)||_\infty \leq 10^{-11}$. Figs. 4.2(a) and (b) show its axial velocity and temperature. The spreading rate of the equilibrium jet is slow, contains weak shock cells, and lacks a

potential core.

The equilibrium baseflow solution was used as the initial condition for a time-resolved calculation and the flow-field was averaged over a period of $\Delta t c_\infty / R \sim 600$ to obtain an alternate $\bar{\boldsymbol{Q}}$. Fig. 4.3(a) and 4.3(b) show the contours of the average axial velocity and temperature. Fig. 4.3(c) shows the $r = 0$ axial velocity for both flows. The time-averaged flow spreads faster than the equilibrium solution and has a weak, yet distinct shock-cell structure.

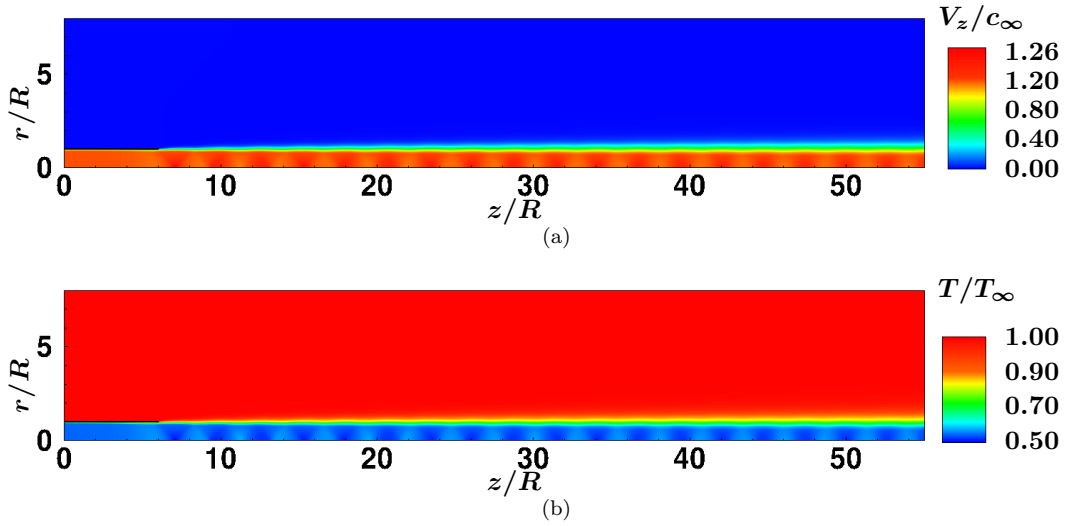

Figure 4.2: Equilibrium solution: (a) axial velocity and (b) temperature.

4.4 Global Modes

To construct the eigenvalue problems in (2.4) and (2.7), the baseflow is linearly interpolated onto a reduced mesh of size $(N_z, N_r) = (1100, 300)$. To focus effort on relevant Strouhal numbers ($St = \omega_i D / 2\pi U_j$), target eigenvalues $(\omega_{r\,\text{target}}, St_{\text{target}})$ (marked 'x' in Fig. 4.4(a) and Fig. 4.5(a)) were used with $\omega_{r\,\text{target}} = 0.10$ and St_{target} in the range $0.05 - 0.65$, with a spacing of $\Delta St_{\text{target}} = 0.05$. For each, 30 eigenmodes were obtained (based on the convergence criterion $||\boldsymbol{L}\widehat{\boldsymbol{Q}} - \omega\widehat{\boldsymbol{Q}}||/||\omega\widehat{\boldsymbol{Q}}|| \sim 10^{-10}$).

4.4.1 Equilibrium $\bar{Q}$

Fig. 4.4(a) shows the eigenspectrum for the equilibrium $\bar{\boldsymbol{Q}}$. As might be expected, the $\omega_r > 0$ values show that the equilibrium solution is globally unstable over a wide range of Strouhal numbers ($St \sim 0.15 - 0.75$), which contrasts with the parameterized but stable baseflow used by Nichols & Lele (2011). Figs. 4.4(b)–(e) show selected eigenmodes at different Strouhal numbers. Modes $B^e_{1,2}$ at lower Strouhal numbers ($St \sim 0.2 - 0.6$)

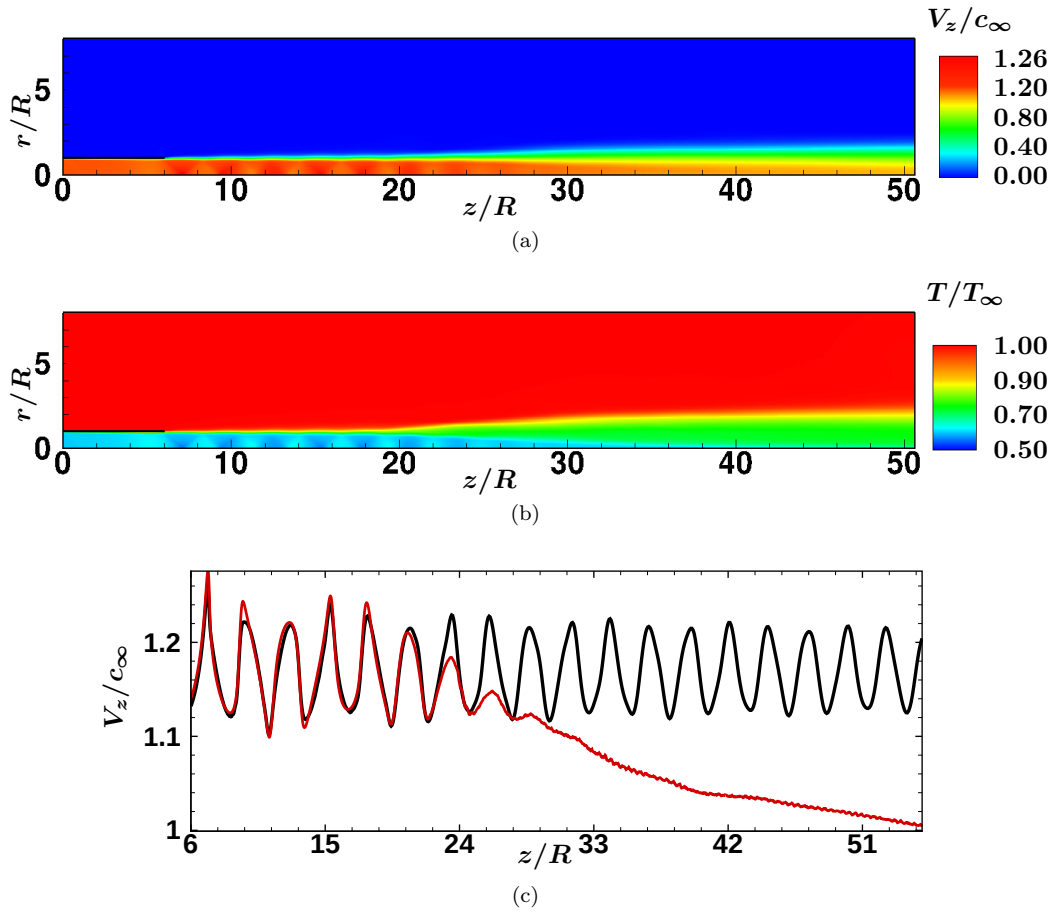

Figure 4.3: Time-averaged $\bar{\boldsymbol{Q}}$: (a) axial velocity, (b) temperature and (c) axial velocity along the centerline for — steady and — time-averaged baseflows.

are predominantly type B (Nichols & Lele, 2011), characterized by upstream-propagating structures. At higher Strouhal numbers ($St \sim 0.7$) the modes have a weak downstream-propagating component with a correspondingly weak acoustic footprint. The adjoint global mode for the most unstable eigenvalue B_3^e is shown in Fig. 4.4(f) with corresponding lipline variation in Fig 4.4(g). We see that the adjoint mode is localized close to the nozzle, with a distinct peak value appearing very close to the nozzle lip, suggesting localized high sensitivity.

4.4.2 Time-average $\bar{Q}$

Fig. 4.5(a) shows the eigenspectrum of the time-average $\bar{\boldsymbol{Q}}$, which is globally stable. Unlike the equilibrium baseflow, this flow supports both downstream-propagating (type A) and upstream-propagating (type B) modes (Nichols & Lele, 2011). Figs. 4.5(b)-(e) show the type A modes for eigenvalues at different Strouhal numbers ($A_1^t - A_4^t$) in Fig. 4.5(a). These modes have a predominantly downstream-propagating wavepacket structure with a strong acoustic footprint, which supports a connection to the far-field noise radiation. Figs. 4.5(f) and (g) show type B modes. Unlike type A modes, these have a strong upstream-propagating component. They have support localized closer to the jet axis. The spectrum also contains hydrodynamically bound modes, identified as $H_{1,2}^t$ in Fig. 4.5(a), which are acoustically inefficient (Figs. 4.5(h) and (i)). A spatial overlap of the forward-adjoint pair corresponding to a given eigenvalue defines a localized region in space called the wavemaker, and the eigenspectrum is most sensitive to modifications of the baseflow within this region (Chomaz, 2005). Following Giannetti & Luchini (2007), the wavemaker is

$$\mathcal{W}(z,r) = \frac{\widehat{\boldsymbol{Q}^\dagger}^T \boldsymbol{D}\boldsymbol{\delta}\boldsymbol{L}\widehat{\boldsymbol{Q}}}{\widehat{\boldsymbol{Q}^\dagger}^T \boldsymbol{M}\widehat{\boldsymbol{Q}}}, \tag{4.3}$$

where $\boldsymbol{\delta L}$ is the perturbation to the linearized operator $\boldsymbol{L}$. For a case with $||\boldsymbol{\delta L}|| = 1$, the wavemaker region for the forward-adjoint pairs corresponding to the eigenvalues A_1^t through A_4^t are shown in Figs. 4.6(a)-(d). Peak values of the wavemaker close to the nozzle lip indicate high dynamical receptivity to localized changes in the baseflow.

4.5 Projection of the Dynamics Onto the Global Modes

The content of the global modes in the nonlinear flow can be computed by projecting the instantaneous perturbation flow-field onto the modes. The global modes form a basis for the linear flow perturbations, and hence the perturbed flow at any time instant can be expressed as a linear combination of the global modes

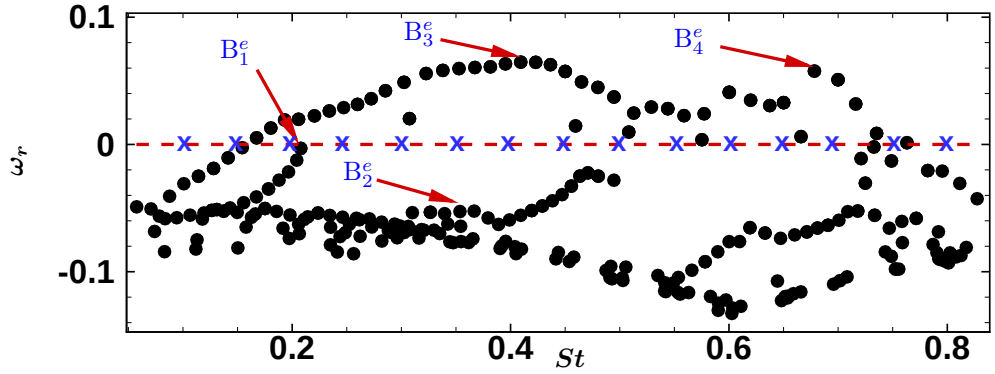

(a) Equilibrium baseflow eigenvalue spectrum

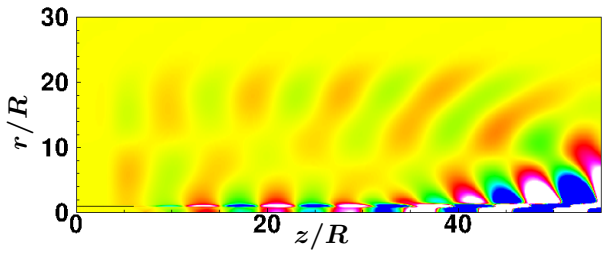

(b)

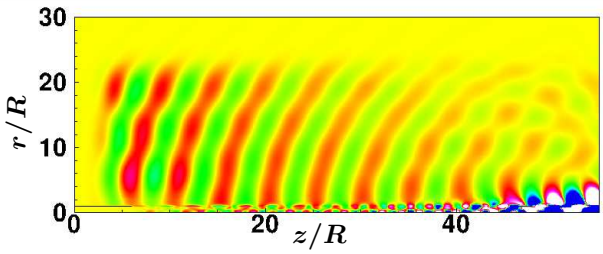

(c)

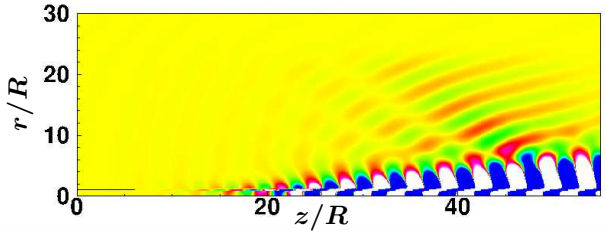

(d)

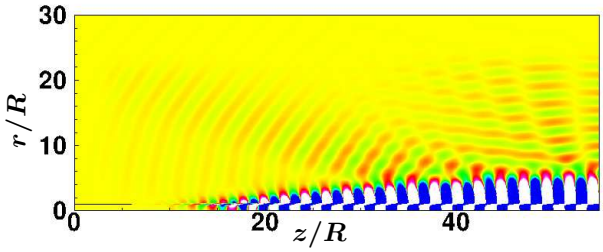

(e)

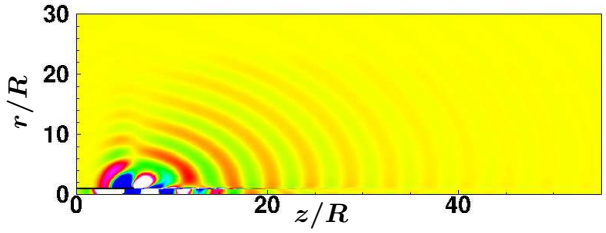

(f)

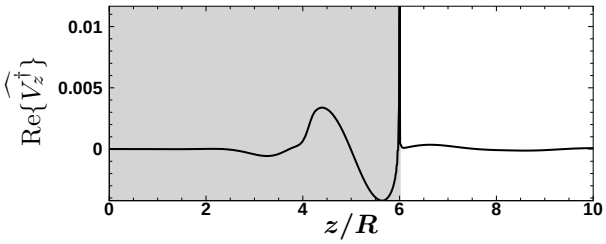

(g)

Figure 4.4: Global modes of the equilibrium solution: (a) eigenspectrum; forward global modes ($\mathrm{Re}\{\widehat{V_z}\}$) (b) mode B_1^e (c) mode B_2^e (d) mode B_3^e (e) mode B_4^e; (f) adjoint global mode ($\mathrm{Re}\{\widehat{V_z^\dagger}\}$) for the most unstable mode B_3^e (g) $\mathrm{Re}\{\widehat{V_z^\dagger}(z, r = 1)\}$.

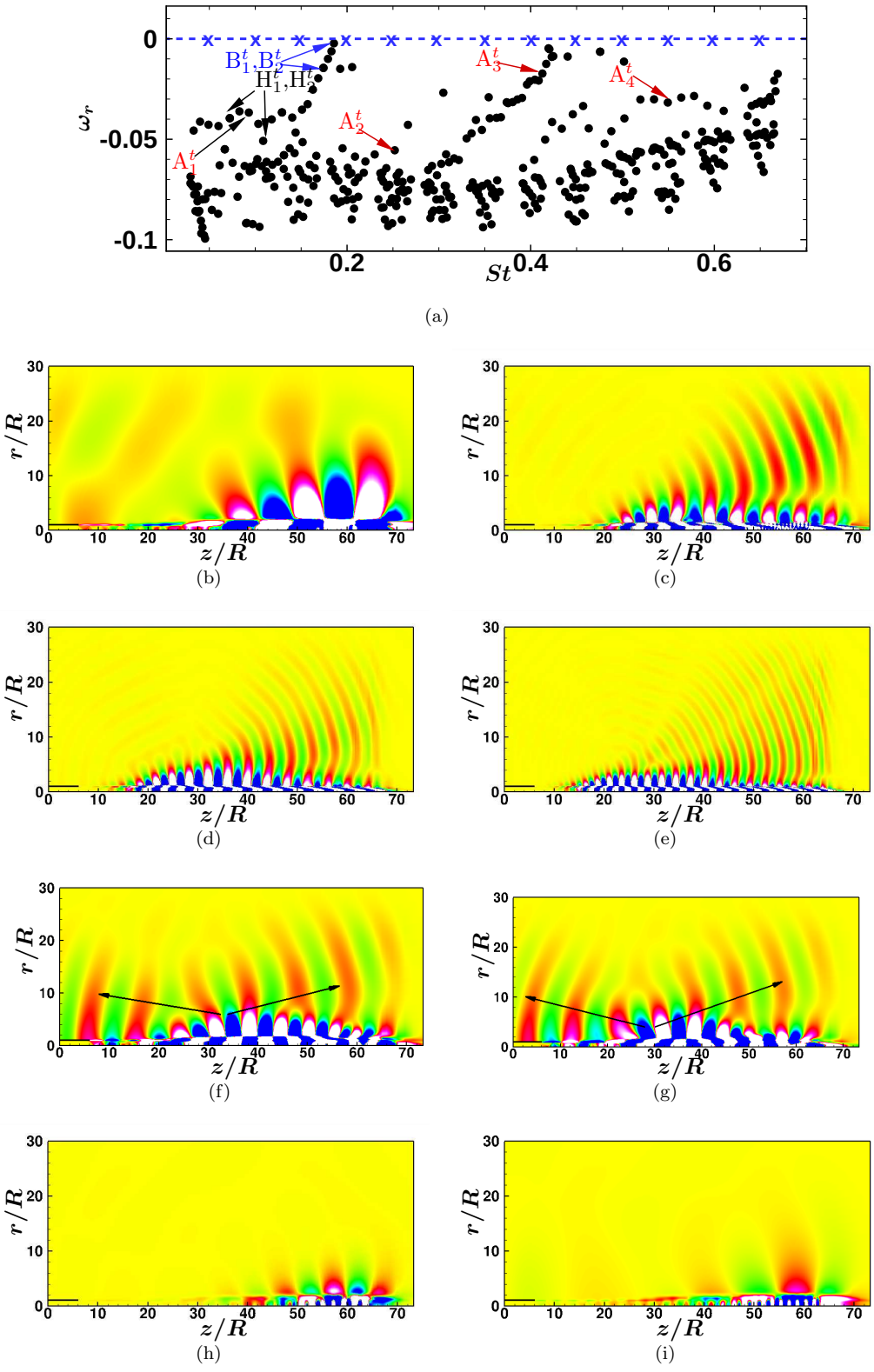

Figure 4.5: Global modes of the time-averaged $\bar{\boldsymbol{Q}}$: (a) eigenspectrum; forward global modes (Re$\{\widehat{V_z}\}$) of type A modes (downstream-propagating): (b) A_1^t (c) A_2^t (d) A_3^t, and (e) A_4^t; type B modes (with a predominant upstream-propagating wave structure): (f) B_1^t (g) B_2^t; hydrodynamic modes (h) H_1^t (i) H_2^t.

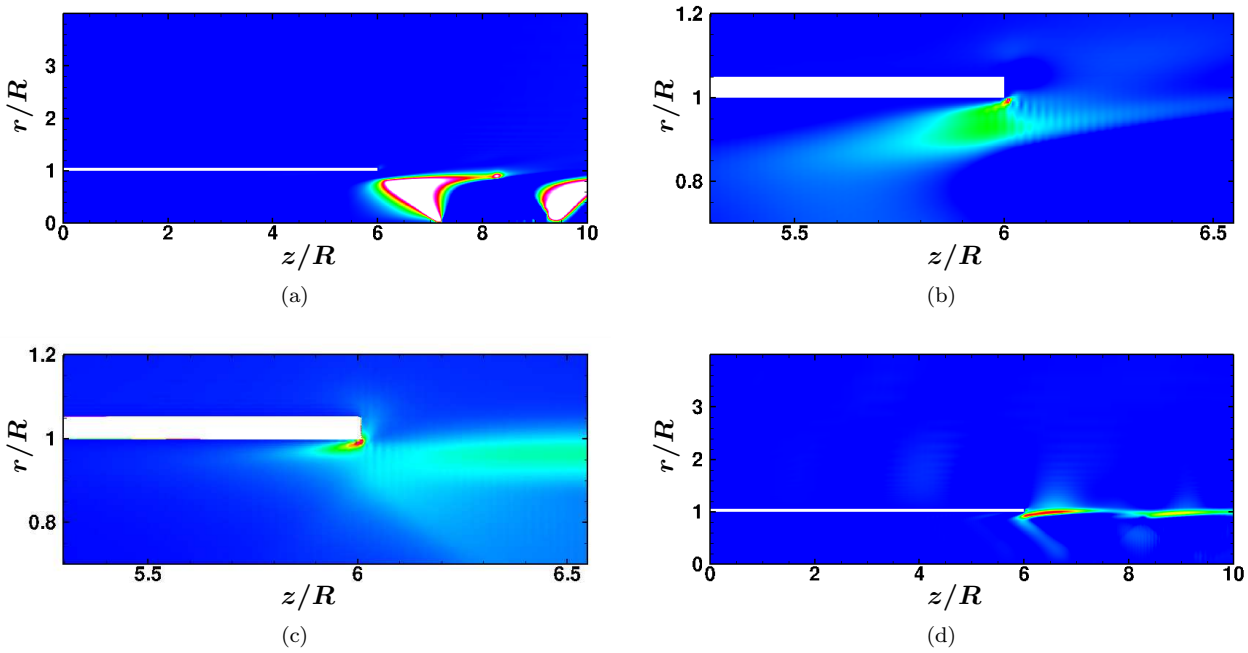

Figure 4.6: Wavemaker region defined by (4.3) for modes: (a) A_1^t, (b) A_2^t, (c) A_3^t and (d) A_4^t.

as

$$\boldsymbol{Q}' = \sum_{m=1}^{N} c_m \widehat{\boldsymbol{Q}_m}, \tag{4.4}$$

where $\widehat{\boldsymbol{Q}_m}$ and $\boldsymbol{Q}'$ are expressed as column vectors, and the projection coefficients c_m are complex valued. From (2.4) and (2.7), we have the following orthogonality condition,

$$\widehat{\boldsymbol{Q}_m}^T \boldsymbol{M}\boldsymbol{D}\widehat{\boldsymbol{Q}_n^\dagger} = 0 \quad \text{for} \quad \omega_m \neq \omega_n, \tag{4.5}$$

where $\widehat{\boldsymbol{Q}_m}$ and $\widehat{\boldsymbol{Q}_n^\dagger}$ correspond to the eigenvalues ω_m and ω_n. A vector inner product (dot product) of Q' with $\widehat{\boldsymbol{Q}_n^\dagger}$, yields

$$\langle \boldsymbol{Q}' \boldsymbol{M}\boldsymbol{D}\widehat{\boldsymbol{Q}_n^\dagger} \rangle = \left\langle \Big(\sum_{m=1}^{N} c_m \widehat{\boldsymbol{Q}_m} \Big) \boldsymbol{M}\boldsymbol{D}\widehat{\boldsymbol{Q}_n^\dagger} \right\rangle. \tag{4.6}$$

Using (4.5), we have

$$\boldsymbol{Q}'^T \boldsymbol{M}\boldsymbol{D}\widehat{\boldsymbol{Q}_n^\dagger} = c_n \widehat{\boldsymbol{Q}}_n^T \boldsymbol{M}\boldsymbol{D}\widehat{\boldsymbol{Q}_n^\dagger},$$

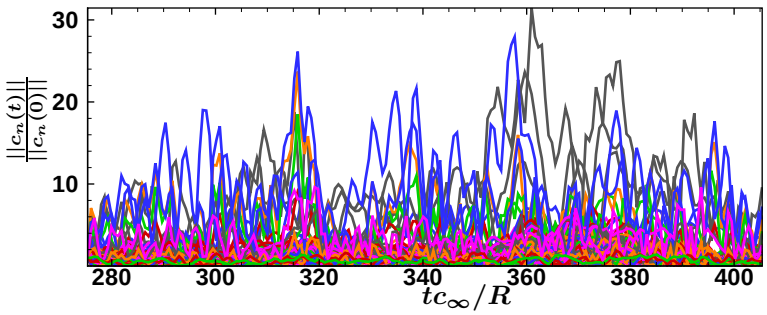

Figure 4.7: Projection of the flow perturbations onto the global modes as given by (4.7) for all the eigenvalues in Fig. 4.5(a).

which gives the projection of the global mode $\widehat{\boldsymbol{Q}}_n$ onto $\boldsymbol{Q}'$ as

$$c_n = \frac{\boldsymbol{Q}'^T \boldsymbol{M}\boldsymbol{D}\widehat{\boldsymbol{Q}}_n^\dagger}{\widehat{\boldsymbol{Q}}_n^T \boldsymbol{M}\boldsymbol{D}\widehat{\boldsymbol{Q}}_n^\dagger}, \tag{4.7}$$

which quantifies the content of the mode $\widehat{\boldsymbol{Q}}_{\boldsymbol{n}}$ to the perturbed flow-field $\boldsymbol{Q}'$. Fig. 4.7 shows the result of the projection of the flow perturbations onto the global modes for the time-averaged baseflow for all the eigenvalues shown in Fig. 4.5(a). It is observed that there are no modes which have a clear prominence over others in the flow-field.

4.6 Optimal Transient Growth

As a consequence of the non-normality of the linearized operator, for a globally stable system, it is possible to obtain perturbation growth for a finite period of time by a particular superposition of the basis for the linear system, namely the global modes (Schmid & Henningson, 2000). Optimal transient growth represents the maximum growth for the linear system in terms of the amplification of the defined disturbance energy norm. Since the long-term motivation of this work is noise control, a pressure perturbation-based energy semi-norm defined as

$$E(t) = \frac{1}{2}\int_{\mathcal{V}} \widehat{p}(t)\widehat{p}(t)^* \, dV = \frac{1}{2}\int_{\mathcal{V}} \widehat{p}(t)\widehat{p}(t)^* \, r dr dz, \tag{4.8}$$

would be instructive as an alternative to the energy-based norm used by Nichols & Lele (2011). Optimal transient growth is the envelope of the worst case scenario for all t and is given by

$$G(t) = \max \frac{\left|\left|\boldsymbol{Q}(t)\right|\right|_E^2}{\left|\left|\boldsymbol{Q}(0)\right|\right|_E^2} \tag{4.9}$$

where $\boldsymbol{Q}(0)$ and $\boldsymbol{Q}(t)$ are the initial condition and its response, respectively. A singular-value decomposition problem is formulated to solve for $G(t)$, and the optimal initial condition $\boldsymbol{Q}_{opt}(0)$ to obtain the transient response at any given time t can be computed (Nichols *et al.*, 2009). Fig. 4.8(a) shows the optimal transient response for the eigenspectrum of the time-average baseflow for the $m = 0$ and $m = 1$ modes. The contribution of the modes to the optimal initial condition is shown in Figs. 4.8(b) and (c). It is observed that the optimal transient response is predominantly due to the superposition of type A global modes in the range $St \sim 0.45 - 0.65$. The optimal transient growth is associated with a propagating aerodynamic wavepacket which emits an acoustic wavepacket into the far-field (Figs. 4.8(d)–(i)), which is a potential mechanism for jet noise production and propagation (Nichols & Lele (2011)), as well as a control objective.

4.6.1 Controller Development

The baseline flow is the uncontrolled time-average $\bar{\boldsymbol{Q}}$ shown in Figs. 4.3(a) and (b). Fig. 4.8(b) shows that the contribution to the optimal initial condition is maximal in the range $St \sim 0.50 - 0.60$. An eigenmode was chosen in this range as the target for developing the controller (Fig. 4.9) with a view of reducing transient growth. From Lighthill's U^8 law (Lighthill, 1952), we know that the noise intensity varies as a high power of the jet velocity. Hence, the axial jet velocity V_z is a natural choice for the control variable and a feedback based on the radial velocity V_r was chosen. Figs. 4.10(a) and (b) show the contours of the forward and adjoint eigenmodes corresponding to the target eigenvalue. The adjoint eigenmode and the wavemaker defined by $\mathrm{Re}(\delta\omega)$ (Fig. 4.10(c)) have a strong growth along the shear layer close to the nozzle lip indicating high sensitivity and hence is the region most viable for flow control (Chomaz, 2005). In the range $St \sim 0.50 - 0.60$, the acoustically efficient global modes do not have peak values close to the outflow. Since the wavemaker region as shown in Fig. 4.6(d) is controlled mostly by the adjoint mode (Fig. 4.10(b)) which is confined very close to the nozzle, our control strategy is not dependent on the mode shapes far downstream of the jet exit. Using the procedure described in Section 2.2.6, a co-located V_z (control) – V_r (feedback) controller was developed, and Fig. 4.10(d) shows the control region.

4.7 Controlled Jet Simulations

To assess the performance of the control on the far-field sound of the baseline jet (Flow A), direct numerical simulations were carried out with the controller developed in Section 4.6.1 with three different gains: Flow B with $\alpha = 2.0$, Flow C with $\alpha = 4.0$ and Flow D with $\alpha = -2.0$. Table 4.1 summarizes the flows and their effect on far-field noise relative to the uncontrolled flow.

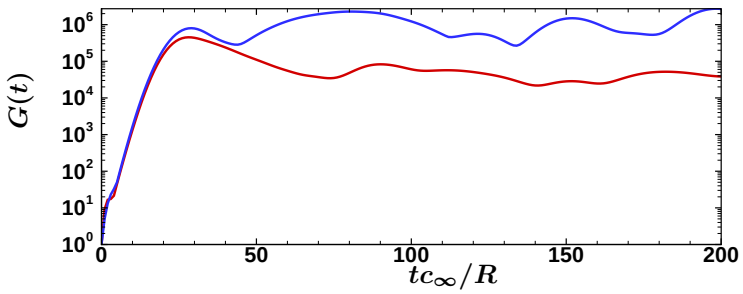

(a)

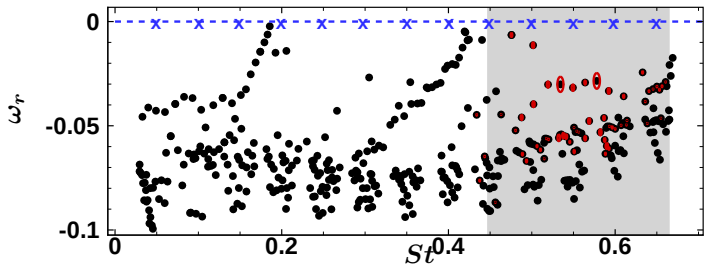

(b)

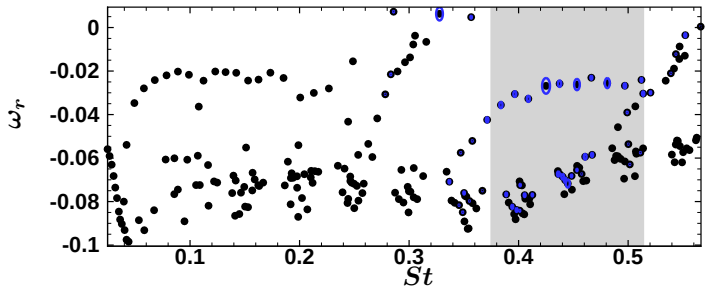

(c)

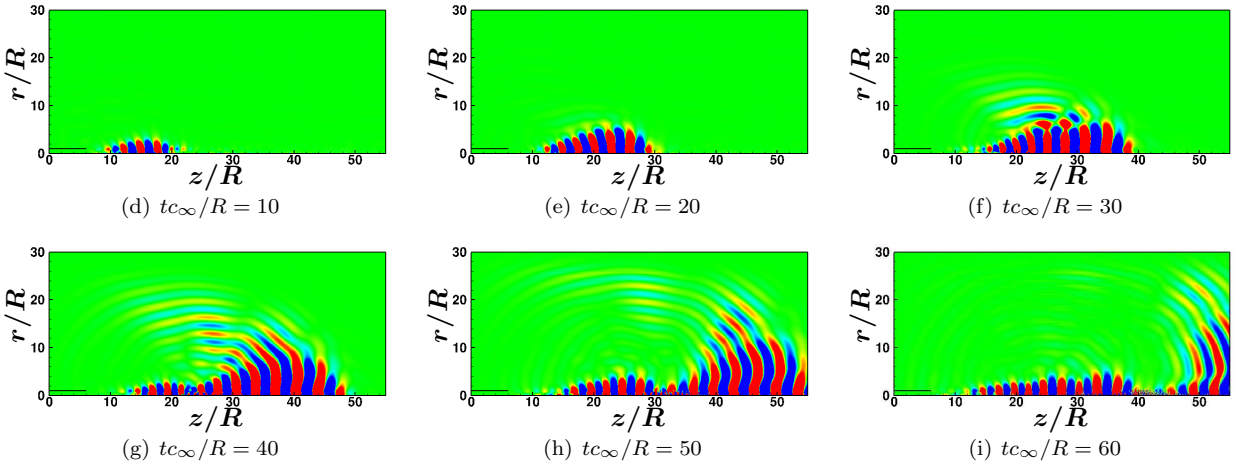

(d) $tc_\infty/R = 10$ (e) $tc_\infty/R = 20$ (f) $tc_\infty/R = 30$

(g) $tc_\infty/R = 40$ (h) $tc_\infty/R = 50$ (i) $tc_\infty/R = 60$

Figure 4.8: (a) Optimal transient response for the time-averaged baseflow for $m = 0$ (—) and $m = 1$ (—) modes; Mode contribution to the optimal initial condition for (b) $m = 0$ (c) $m = 1$. The size of the symbols is proportional to the contribution of the corresponding global mode to the optimal initial condition (d)–(i) Evolution of the optimal initial condition for $m = 0$ modes. Color levels in (d)–(i) show the real part of perturbation pressure.

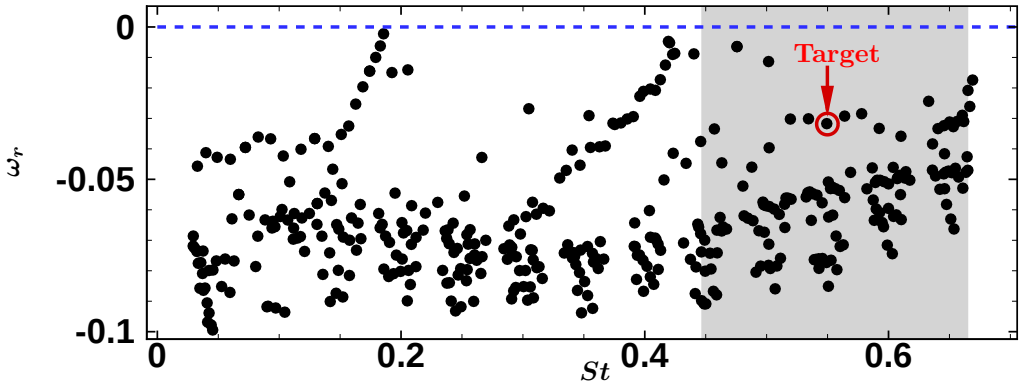

Figure 4.9: Global eigenspectrum for the uncontrolled time-average flow. The target eigenvalue for control is circled.

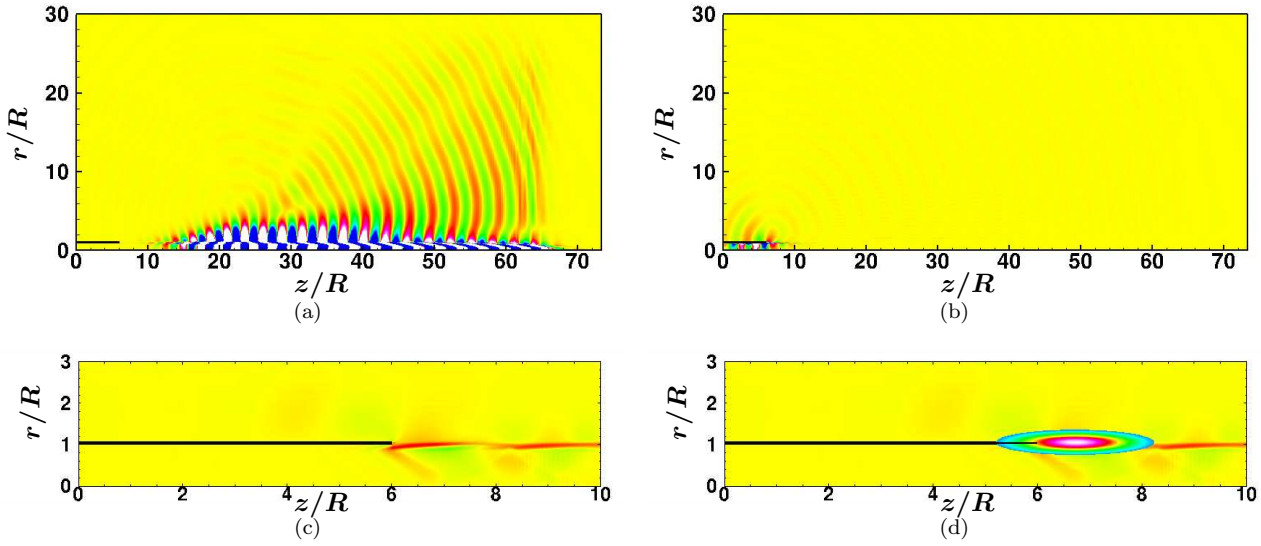

Figure 4.10: Visualization of the (a) flow eigenmode ($\widehat{V_z}$), (b) adjoint eigenmode ($\widehat{V_z^\dagger}$), (c) wavemaker and (d) the co-located actuator/sensor region for $V_z - V_r$ control-feedback.

Simulation	Control gain(α)	Effect on far-field noise
Flow A	0.0	Uncontrolled flow
Flow B	2.0	Quieter
Flow C	4.0	Quieter
Flow D	-2.0	Louder

Table 4.1: Direct numerical simulations to study the effect of control on far-field sound.

Noise Control

The target surface to quantify the radiated noise is a cylindrical region Ω at $r/R = 15$ (Fig. 4.1) and the objective function is

$$\mathcal{I}_{\text{noise}}(t) = \int_{\Omega} (p(\boldsymbol{x}, t) - \bar{p}(\boldsymbol{x}))^2 \, d\Omega. \tag{4.10}$$

Fig. 4.11 shows the contours of vorticity and pressure perturbation at $tc_\infty/R = 870$ for all the cases. The pressure perturbation contours clearly suggest the radiated sound is much higher for Flow D. Fig. 4.12 shows an instantaneous snapshot of vorticity for all the cases. For the quieter flows B and C, the vortex pairing is less vigorous and is delayed further downstream by the control. Figs. 4.13(a), (b) and (c) show the objective function $\mathcal{I}_{\text{noise}}(t)$ for all the flows. A specific trend of the far-field noise as a function of the control gain α is observed, the flow becoming quieter with the increase in gain. The trend can be observed in Fig. 4.13(d) as well, which shows the Overall Sound Pressure Level (OASPL) along the target surface Ω. Figs. 4.14(a) and (b) show the $z - t$ diagram for the pressure perturbation ($p' = p - \bar{p}$) along the lipline $r/R = 1$ for the quieter flow C and the louder flow D. The louder flow has vigorous and frequent vortex pairing events which are less frequent in the quieter flow.

Global Eigenanalysis of Controlled Flows

A global eigenanalysis was performed for the time-averaged flows for all the cases to identify changes in the spectrum and mode shapes. From Figs. 4.15(b) and (c), a fundamental change can be observed in the eigenspectrum for the quieter flows B and C. An unstable global mode is present for the quieter flows but the louder flow D (Fig. 4.15(d)) and the uncontrolled flow (Fig. 4.15(a)) have very similar eigenstructure. Figs. 4.16(c) and (d) show the eigenmode corresponding to the unstable eigenvalue for the quieter flows B and C. These modes do not have significant support in the acoustic field, in comparison to the stable modes which do (Figs. 4.16(a) and (b)).

Projection Onto Global Modes for the Controlled Flows

Using the method outlined in Section 4.5, the projection of the flow perturbations onto the global modes for the uncontrolled and controlled flows were computed. Figs. 4.17(a) and (b) show the amplification for the louder flows A and D. It is observed that none of the modes have a clear prominence over others in the flow-field, whereas for the quieter flows B and C (Figs. 4.17(c) and (d)), it can be seen that the unstable modes have a much higher amplification, reach a limit cycle and continue to be more prominent in the

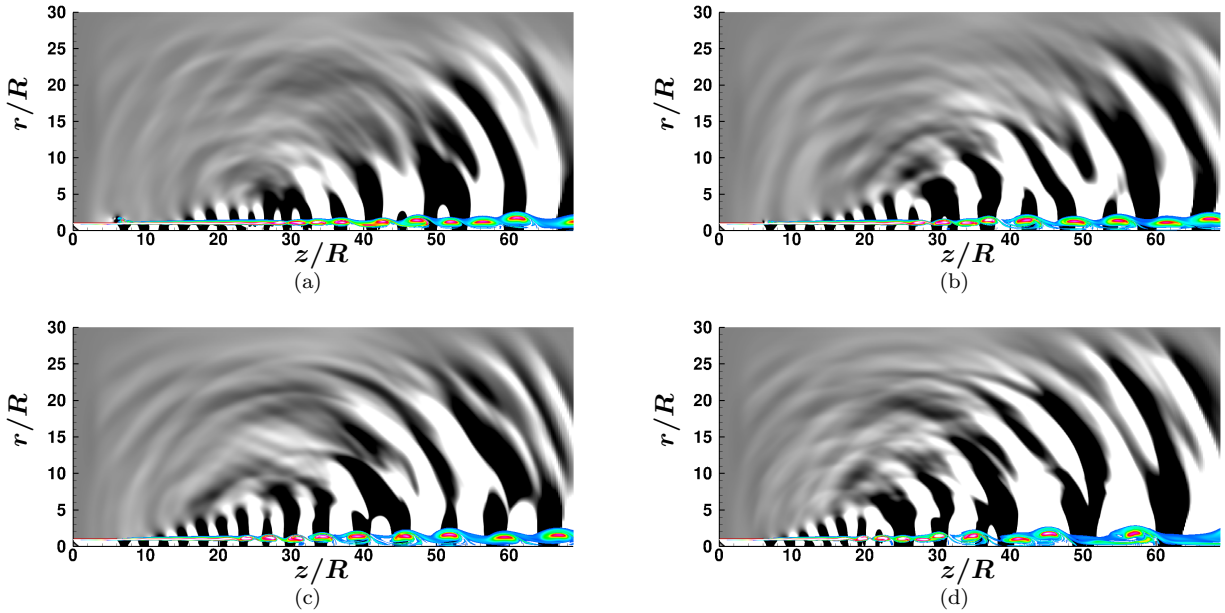

Figure 4.11: Contour plot of vorticity and pressure perturbation at $tc_\infty/R = 870$: (a) $\alpha = 4.0$, (b) $\alpha = 2.0$, (c) No control, and (d) $\alpha = -2.0$.

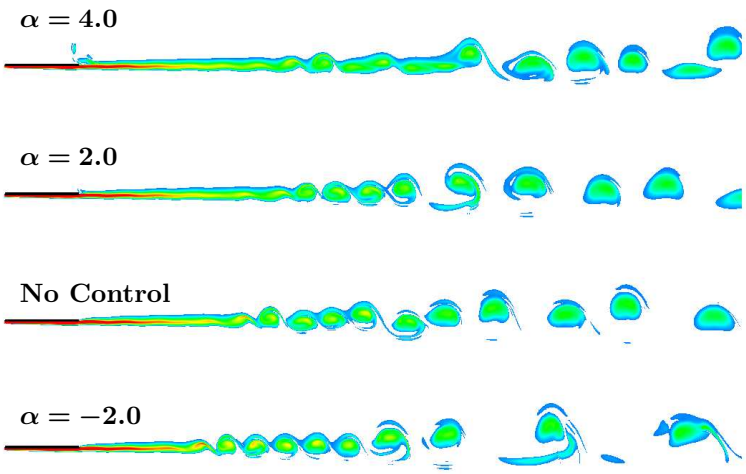

Figure 4.12: Visualization of vorticity at $tc_\infty/R = 880$.

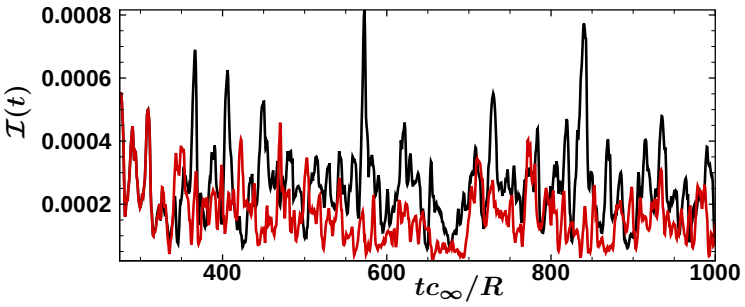

(a)

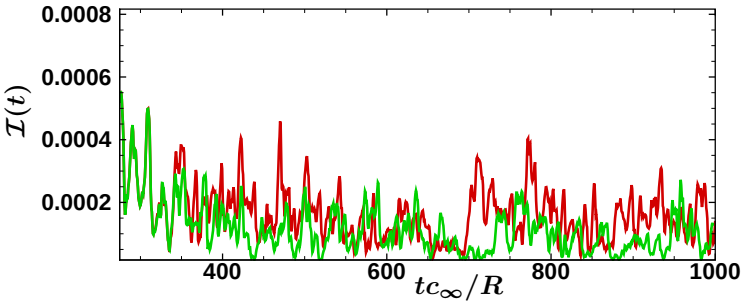

(b)

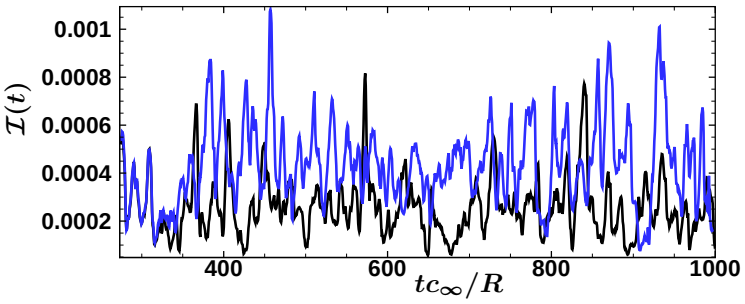

(c)

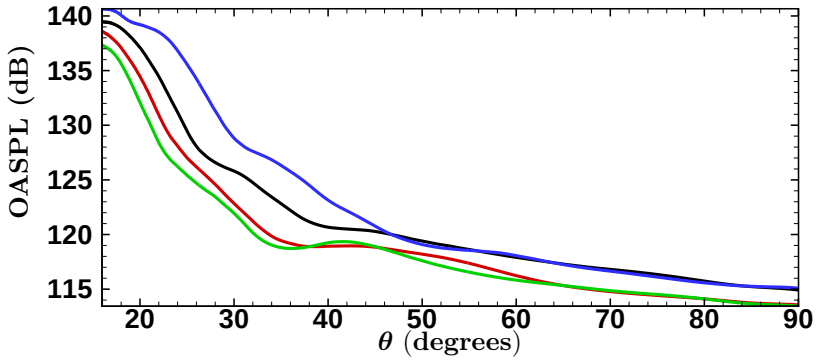

(d)

Figure 4.13: (a)-(c) The objective function $\mathcal{I}(t)$ at $r/R = 15$: —— uncontrolled; —— $\alpha = 2.0$; —— $\alpha = 4.0$; —— $\alpha = -2.0$; (d) the overall sound pressure level on target surface Ω (θ is the angle measured from the jet axis with the vertex at the nozzle exit).

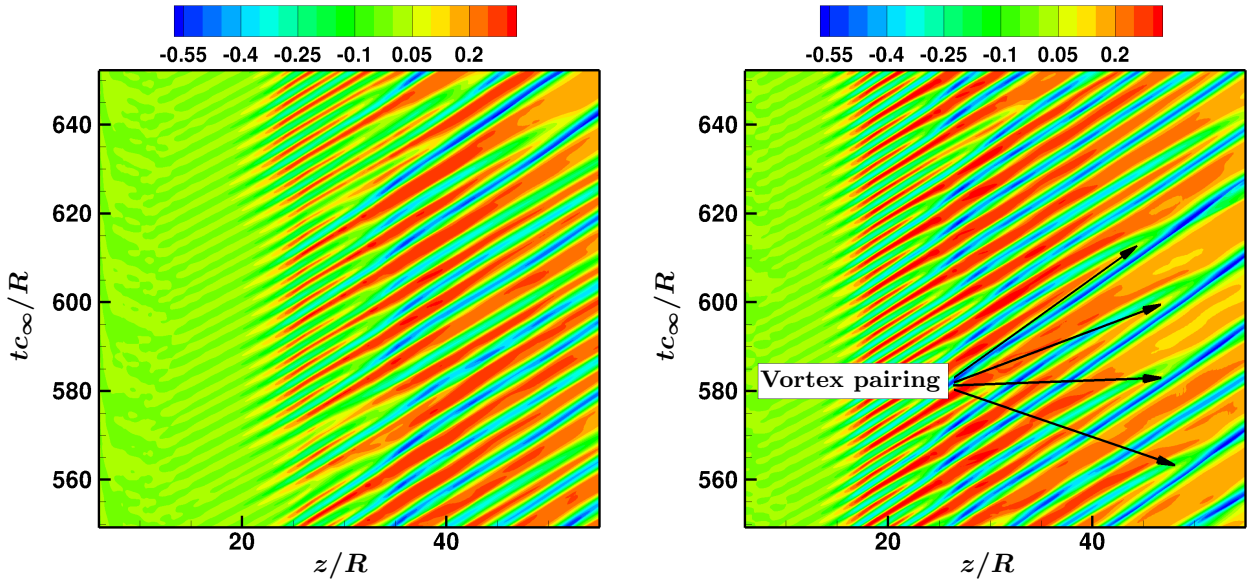

Figure 4.14: $z-t$ diagram of pressure perturbation along the lipline $r/R=1$ for (a) flow C and (b) flow D.

flow-field throughout the control time period. Hence the unstable modes, which do not have any significant acoustic footprint, are more prominent in the flow-field than the acoustically efficient stable modes.

Mean Flow Alterations

Time-averaged flow quantities are computed for all the flows to analyze the changes due to control. Fig. 4.18 shows the axial variation of jet half-width, momentum thickness and centerline axial velocity. It can be seen that all the flows have the same initial mean flow development until ~ 15 jet radii, and changes are apparent only further downstream. There is a specific trend of the mean flow quantities as a function of the control gain. Changes in the half-width (Fig. 4.18(a)) become significant at the axial location where the vortex shedding begins, sand the quieter flows have lower spreading rate downstream. The momentum thickness (Fig. 4.18(b)) also shows a similar trend as the flow becomes quieter. Fig. 4.18(c) shows that the quieter flows have a slower rate of decay of the centerline axial velocity.

Proper Orthogonal Decomposition

A Proper Orthogonal Decomposition (POD) of the flow-field is performed to quantify changes to the energetic perturbations caused by the control (see Appendix G). The analysis is carried out using snapshots of the flow-field that span the whole time interval in Fig. 4.13 for the flows A and B, using a pressure based inner

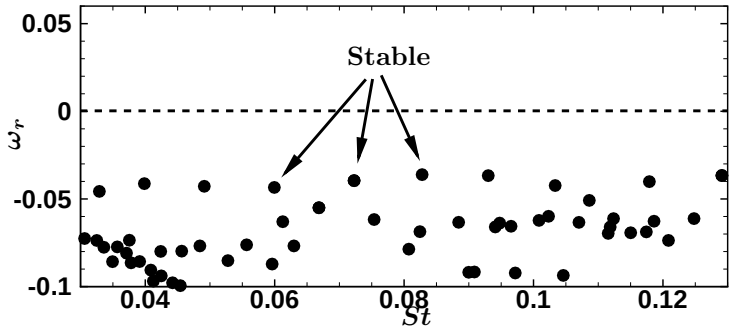

(a)

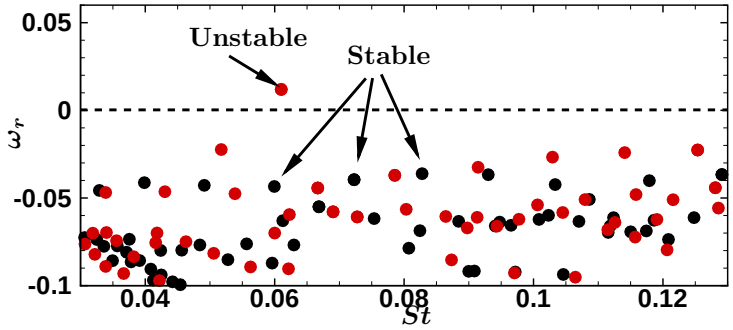

(b)

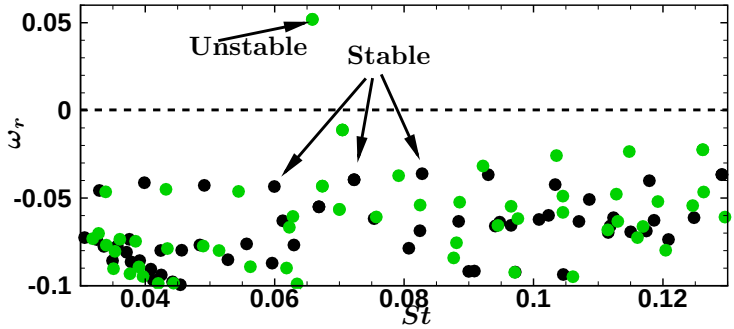

(c)

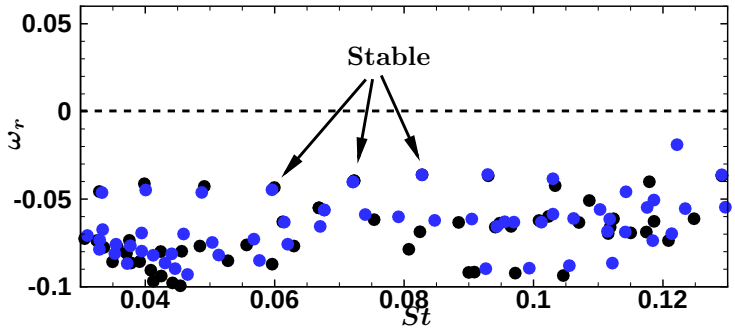

(d)

Figure 4.15: Eigenspectrum for all time-averaged flows: ● uncontrolled, ● $\alpha = 2.0$, ● $\alpha = 4.0$, and ● $\alpha = -2.0$.

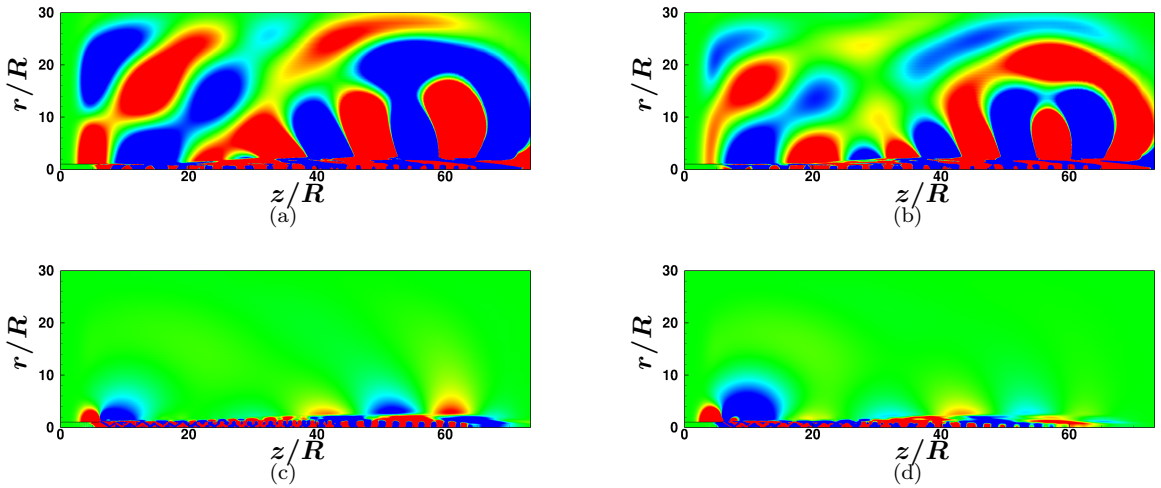

Figure 4.16: Visualization of flow eignmodes: (a), (b) stable modes marked in Fig. 4.16(a); (c), (d) eigenmode corresponding to the unstable eigenvalue for $\alpha = 2.0$ and $\alpha = 4.0$.

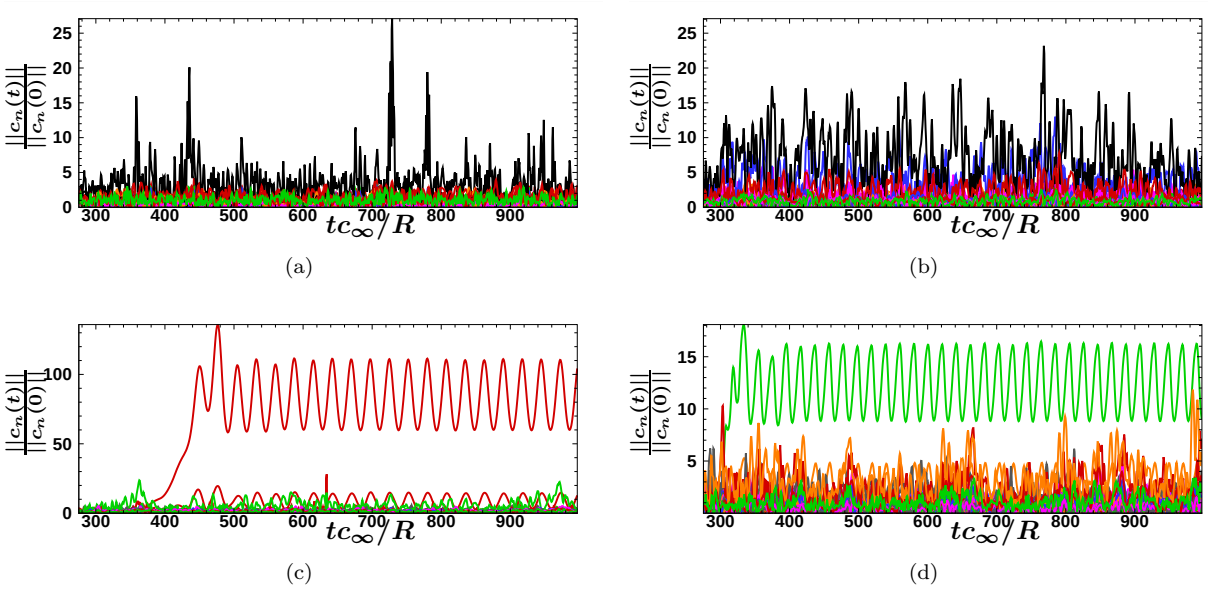

Figure 4.17: Projection of the flow perturbations onto the global modes as given by (4.7) for all the flows for the eigenvalues shown in Fig. 4.15: (a) $\alpha = -2.0$, (b) no control, (c) $\alpha = 2.0$ and (d) $\alpha = 4.0$.

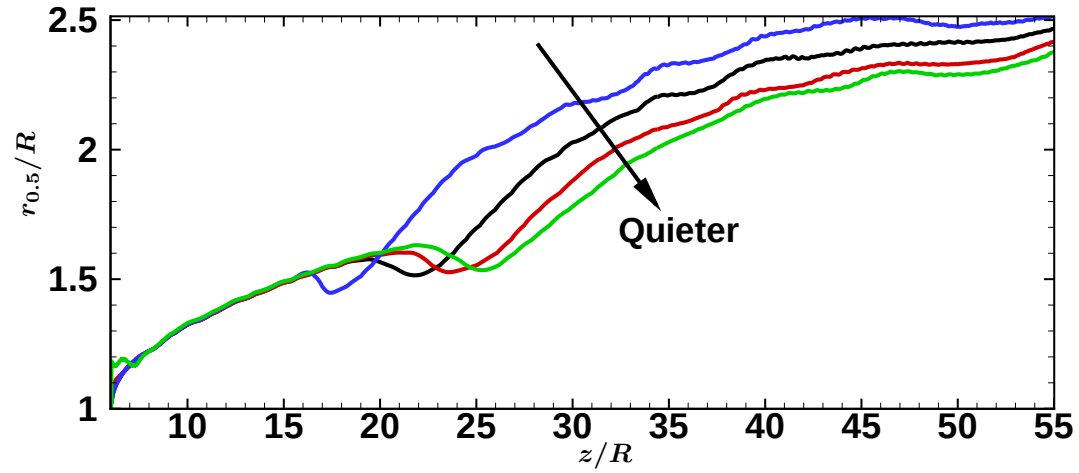

(a)

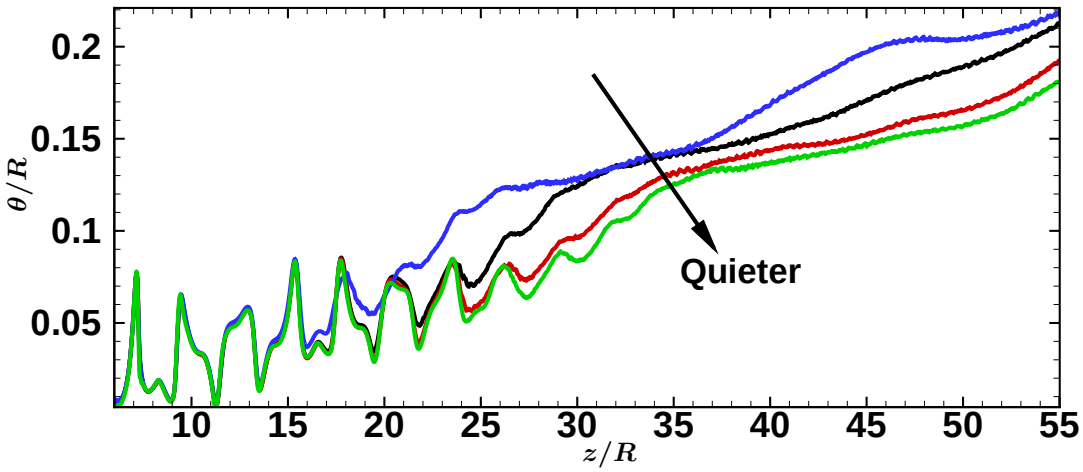

(b)

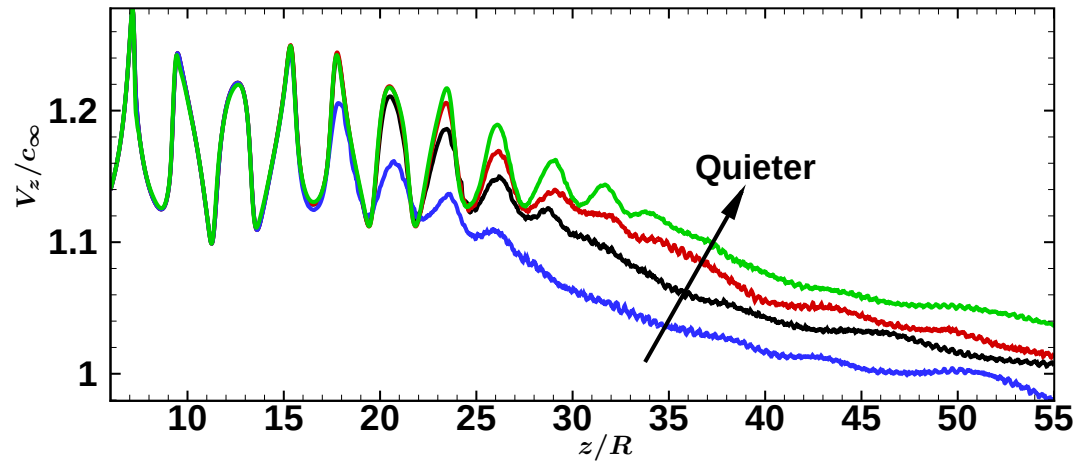

(c)

Figure 4.18: Time-averaged flow quantities: — uncontrolled; — $\alpha = 2.0$; — $\alpha = 4.0$; — $\alpha = -2.0$ (a) jet half-width, (b) momentum thickness, and (c) centerline axial velocity.

product norm defined by

$$\langle \boldsymbol{Q_i}, \boldsymbol{Q_j} \rangle_{\mathrm{P}} = \int_V p'_i(z,r) p'_j(z,r)\, r\, dz\, dr, \tag{4.11}$$

where i and j refer to two instantaneous snapshots of the flow field $\boldsymbol{Q}$. Fig. 4.19(a) shows the POD eigenspectrum for all the flows. A semilog plot of the same is shown in Fig. 4.19(b). The reconstructed pressure perturbation field was observed to converge using 23 modes. It can be seen that, in the chosen norm, there is a continuous decrease in the eigenspectrum as the flow gets quieter. Fig. 4.13(a) shows that the sound at the target surface is characterized by intermittent peaks separated by periods of quietness. We use POD to anlayze the change in flow behavior by performing a time-localized POD for a time interval isolating a loud event E in Flow A that was quiet in Flow B. A kinetic energy norm was used defined as

$$\langle \boldsymbol{Q}_i, \boldsymbol{Q}_j \rangle_{\mathrm{KE}} = \int_V (V'_{r_i} V'_{r_j} + V'_{z_i} V'_{z_j})\, r\, dz\, dr. \tag{4.12}$$

Fig. 4.19(a) shows a comparison of the eigenspectrum for Flows A and B. The first two energetic modes for the uncontrolled flow are shown in Figs. 4.20(c) and (d) and those of the quieter flow B are shown in Figs. 4.20(e) and (f) respectively. Pairing of the most energetic modes can be observed for the quiet flow B. The radial velocity field was reconstructed using the modes as

$$V'_r = \sum_n a_n \psi_n^{\mathrm{KE}}, \tag{4.13}$$

where ψ_n^{KE} denotes the n^{th} POD mode. Phase plots of the POD coefficients $a_1(t)$ and $a_2(t)$ of the first two energetic modes for flows A and B are shown in Figs. 4.21(a) and (b) respectively. The plots show that the quieter flow B is more regularized during this time interval compared to flow A, which has been observed in a noise-controlled mixing layer (Wei & Freund, 2006).

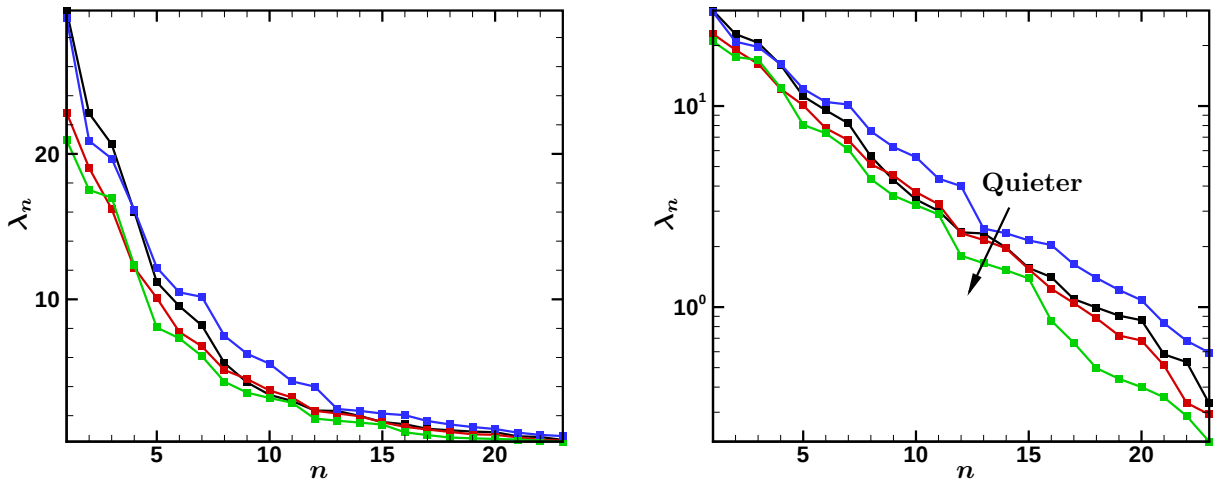

(a) (b)

Figure 4.19: (a) POD eigenspectrum for all the flows using the pressure based norm defined in (4.11) and (b) in semilog scale: — uncontrolled; — $\alpha = 2.0$; — $\alpha = 4.0$; — $\alpha = -2.0$.

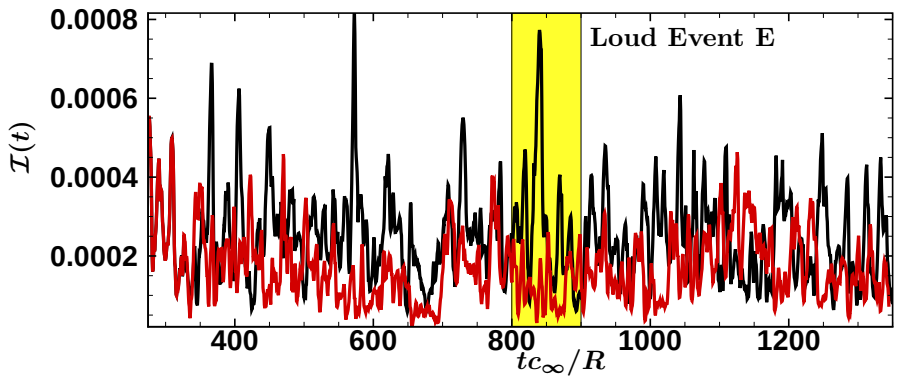

(a)

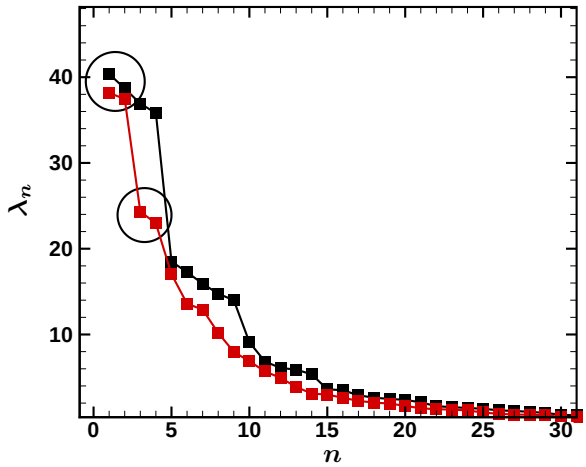

(b)

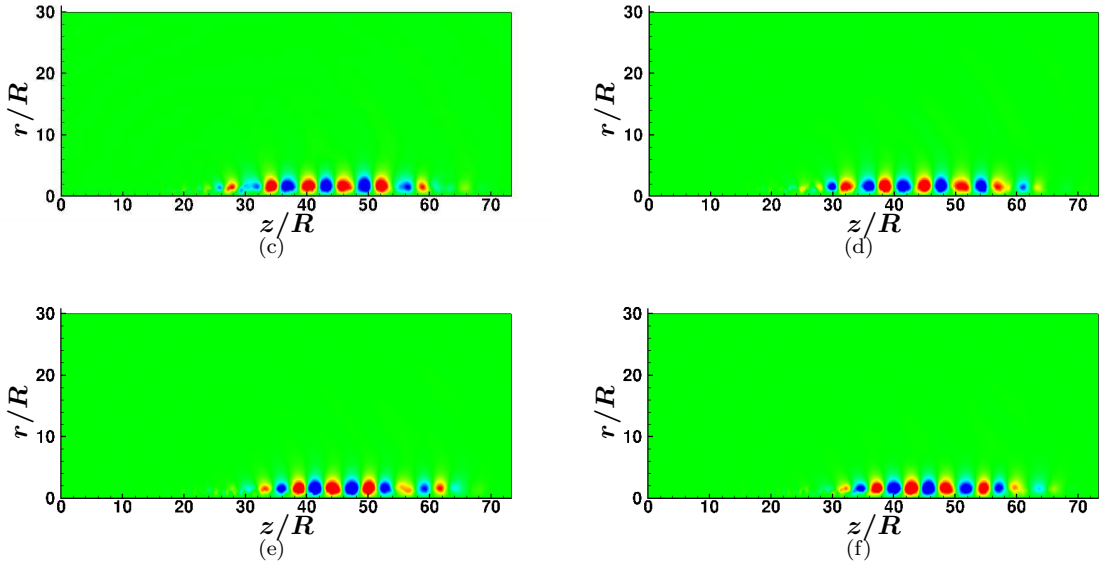

Figure 4.20: (a) The objective function $\mathcal{I}(t)$ showing the time interval of the loud event E. (b) POD eigenspectrum: —— uncontrolled; —— $\alpha = 2.0$. First two energetic POD modes: (c), (d) uncontrolled and (e), (f) $\alpha = 2.0$.

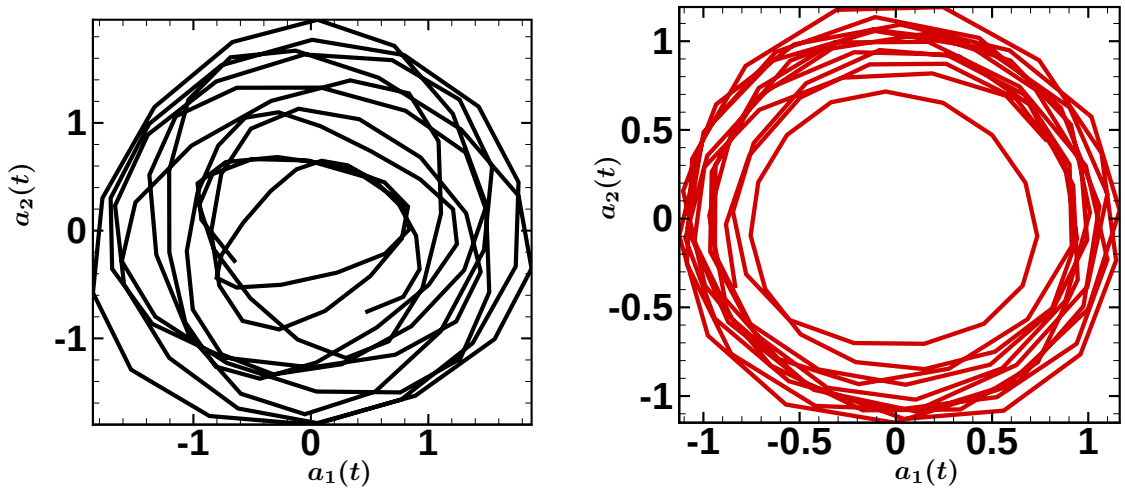

(a) (b)

Figure 4.21: The POD coefficients for the first two energetic modes for (a) flow A and (b) flow B.

Chapter 5

Noise Reduction of a Turbulent Jet

This chapter is devoted to the noise reduction of a Mach 0.9 turbulent jet. The control strategy of Chapter 4 is utilized to develop the controller for a Mach 0.9 jet baseflow computed using large eddy simulation (LES). Section 5.1 gives the details of the numerics and flow conditions. The eigenanalysis of the baseline flow is given in Section 5.2 and the results and analysis of controlled simulations are given in Section 5.3.

5.1 Large Eddy Simulation

Fig. 5.1(a) shows the domain for the LES of a turbulent jet issuing from a cylindrical nozzle with centerline Mach number $M_j = U_j/c_j = 0.9$ at a Reynolds number of $Re = \rho_j U_j D/\mu_j = 88000$. The centerline temperature ratio is $T_j/T_\infty = 0.86$. The incoming boundary layer has a momentum thickness of $\theta/D = 0.03$ at the nozzle exit. The nozzle is isothermal with a wall temperature of $T_{\text{wall}}/T_\infty = 1$ and the nozzle length and wall thickness are $L/D = 3$ and $t_{\text{nozzle}}/D = 0.025$, respectively. An overset grid approach is used for the simulations with 5.81 million grid points. The grid consists of a cartesian core grid $(L_x, L_y, L_z) = (0.25, 0.25, 30)$ of dimensions $((N_x, N_y, N_z) = (50, 50, 459)$ and an outer annular cylindrical grid $(r_{\min}, r_{\max}, L_z) = (0.25, 12.5, 30)$ of dimensions $(N_r, N_\theta, N_z) = (318, 32, 459)$. Derivatives are computed using 4-2 summation-by-parts finite-difference operators (Strand (1994)), and fourth-order Runge-Kutta is used for temporal integration. Data are interpolated between the overset grids using linear interpolation. The LES uses a dynamic Smagorinsky model (Moin *et al.*, 1991) with a 7-point explicit least squares test filter (Fig. 5.1(b)). The flow solution is also filtered using a tridiagonal implicit filter (Fig. 5.1(b)) with $\alpha_f = 0.49$. Navier-Stokes characteristic boundary conditions are used for the isothermal nozzle walls and sponge zones (Freund (1997), Bodony (2006)) are used at the domain boundaries to prevent spurious reflections into the domain while non-reflecting boundary conditions with the Simultaneous-Approximation-Term approach (Svärd *et al.* (2007)) are used at the end of the sponge zones. The target surface Ω for the computation of the near-field sound is cylindrical with $r_{\text{target}}/D = 7$.

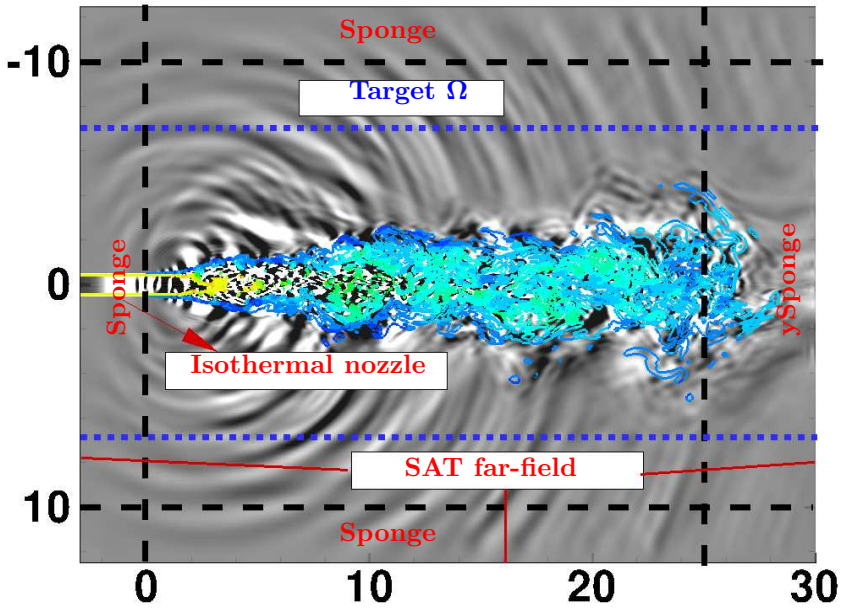

(a)

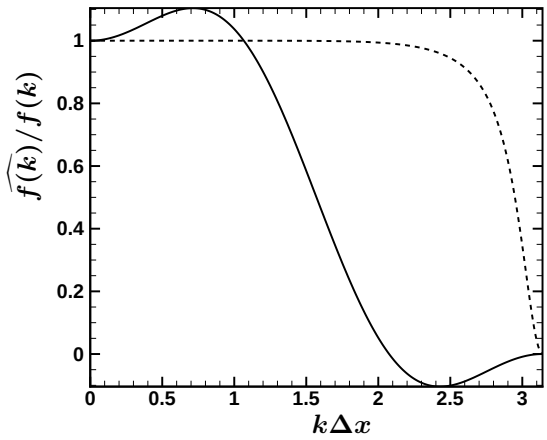

(b)

Figure 5.1: (a) Computational domain and boundary conditions and (b) transfer functions for the LES test filter (—) and flow solution filter (−−).

5.2 Eigenanalyis of the Baseline Flow

The baseflow for the eigenanalaysis is the time-and-azimuthal averaged flow averaged over $\Delta t c_\infty / D \sim 300$. Figs. 5.2(a) and (b) show the contours of axial velocity and temperature for the time-and-azimuthal averaged baseflow. Fig. 5.2(c) shows a comparison of the centerline axial velocity with the result of Bodony (2005), who did an LES of the jet at the same conditions. It is understood that the $m = 0$ modes are an important component of even high-Reynolds-number turbulent jets (Cavalieri *et al.*, 2013), and previous studies of jet noise control suggest that disruption of the coherence of acoustically efficient axisymmetric flow structures is a possible mechanism (Kim *et al.*, 2014). Hence we focus on the axisymmetric modes for noise control in the present work. The eigenspectrum for the time-and-azimuthal averaged flow for a wide range of Strouhal numbers ($St \sim 0.05 - 1.70$) is shown in Fig. 5.3(a). For the modes shown, at low Strouhal numbers ($St \sim 0.05 - 0.30$) the acoustically-active modes do not exhibit a directive pattern (Fig. 5.3(b)) but, as the Strouhal number increases ($> St \sim 0.40$), the modes begin to exhibit super-directive (Figs. 5.3(c) and (d)) and multi-directive modes ($St > 1.4$) (Fig. 5.3(e)), as has been observed by Schmidt *et al.* (2016).

5.2.1 Optimal Transient Growth

The jet's optimal transient growth is associated with a propagating aerodynamic wavepacket that emits an acoustic wavepacket into the far-field, which is a potential mechanism for jet noise propagation (Nichols & Lele (2011)), as well as a control objective. Since the motivation of this chapter is noise reduction, a pressure perturbation based energy semi-norm defined as

$$E(t) = \frac{1}{2} \int_{\mathcal{V}} \widehat{p}(t) \widehat{p}(t)^* \, dV = \frac{1}{2} \int_{\mathcal{V}} \widehat{p}(t) \widehat{p}(t)^* \, r dr dz, \tag{5.1}$$

is used as an alternative to the energy-based norm used by Nichols & Lele (2011). Fig. 5.3(f) shows the optimal transient response for the eigenspectrum of the time-average baseflow for the $m = 0$ modes. The contribution of the modes to the optimal initial condition is shown in Fig. 5.4(a). It is observed that the optimal transient response is predominantly due to the superposition of multi-directive global modes (Figs. 5.4(b) and (c)) in the range $St \sim 0.45 - 0.65$. We target mode $O1$ which has the maximum contribution to the optimal initial condition. The adjoint of mode $O1$ is shown in Fig. 5.4(d). Fig. 5.4(e) shows a close-up view of the adjoint at the nozzle lip, and it is observed that the adjoint has a peak value at the lower nozzle lip. The discrete-adjoint formulation used is not dual consistent, and hence, close to the nozzle-lip, the adjoint is found to exhibit an oscillatory behavior. Similar behavior with the same formulation has been observed by Chandler *et al.* (2012) in low-Mach number jets. Hicken & Zingg (2011) have shown that a dual

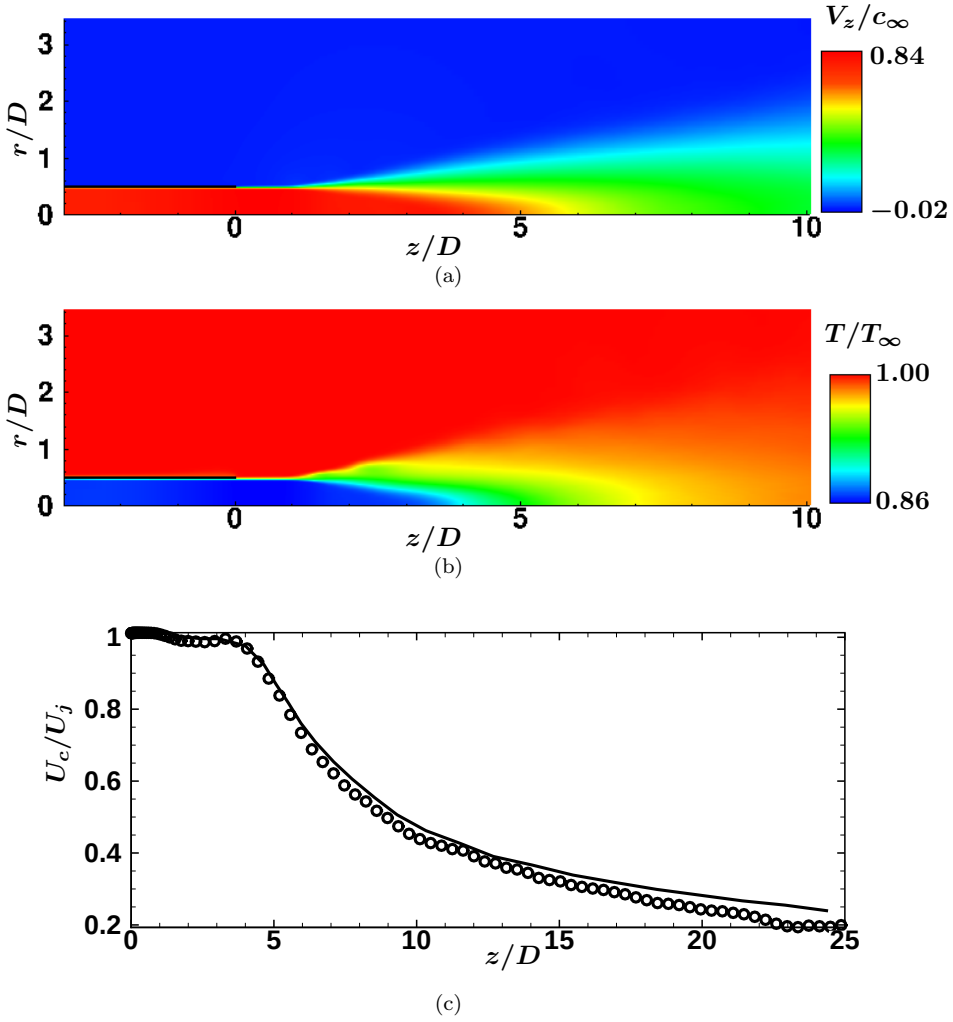

Figure 5.2: Time-and-azimuthal averaged contours of (a) axial velocity and (b) temperature; (c) centerline axial velocity: present (—); Bodony & Lele (○).

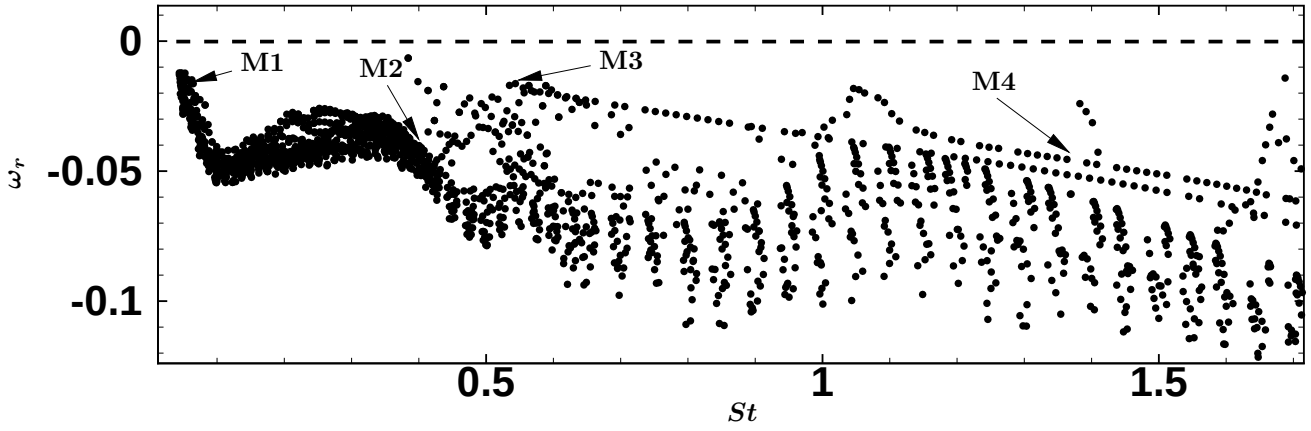

(a)

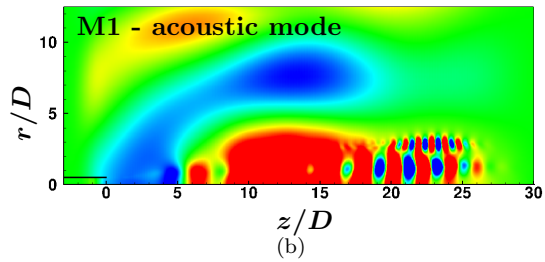

(b)

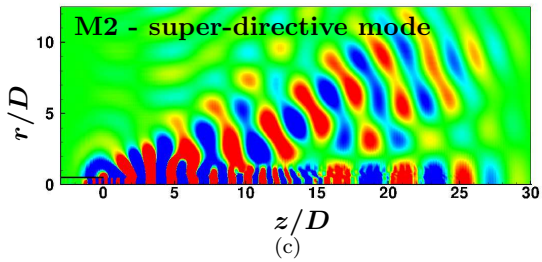

(c)

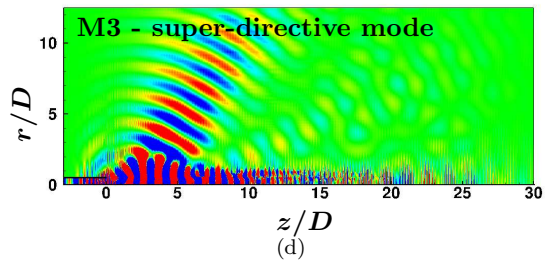

(d)

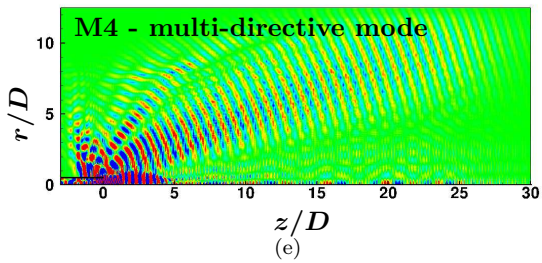

(e)

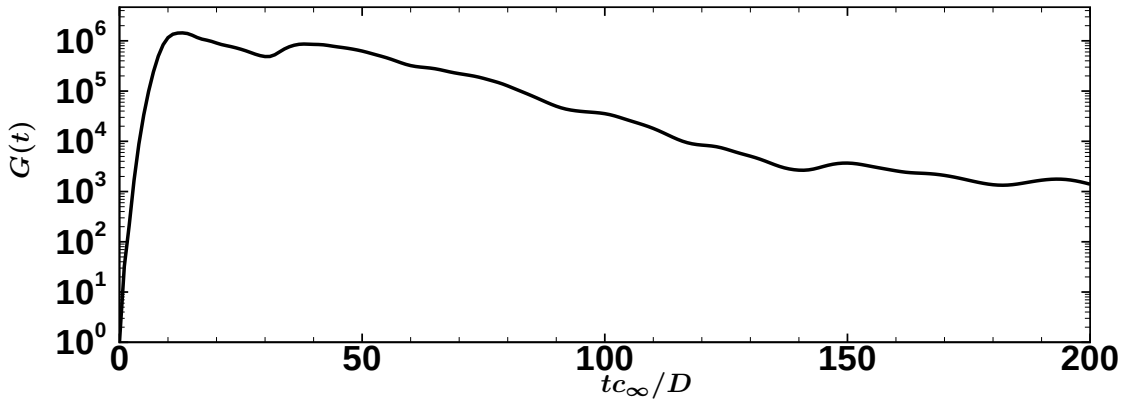

(f)

Figure 5.3: (a) Eigenspectrum and eigenmodes (Real($\widehat{p}$)) for the (b) acoustic mode M1, (c), (d) super-directive modes M2 and M3, and (e) multi-directive mode M4; (f) envelope of optimal transient response.

consistent formulation gives physically relevant adjoint fields.

5.3 Noise Controlled Simulation

Using the control strategy in Section 2.2.6, we develop a V_z (control)-V_r (feedback) controller (Fig. 5.4(f)). To assess the performance of the control on the radiated sound of the baseline jet (T1), a LES was performed with a control gain of $\alpha = 2.0$ (T2). To ensure consistency, a forcing term consistent with the applied momentum forcing appears in the total energy equation. Hence the governing equations for the z-momentum and the total energy equation with the forcing terms are

$$\frac{\partial \rho V_z}{\partial t} = \tilde{\boldsymbol{R}}_{\rho V_z} + \underbrace{\alpha\rho(V_r - \overline{V_r})e^{-(z-z_0)^2/\ell_z^2-(r-r_0)^2/\ell_r^2}}_{\mathrm{F}_{\rho \mathrm{V_z}}}, \tag{5.2}$$

$$\frac{\partial \rho E}{\partial t} = \tilde{\boldsymbol{R}}_{\rho E} + F_{\rho V_z} V_z. \tag{5.3}$$

Figs. 5.5(a) and (b) show the instantaneous contours of vorticity-dilatation at $tc_\infty/D = 163$ for the baseline and T2. The dilatation contours are less intense at the target surface for T2, which is indicative of its quieter nature. A near-nozzle view of the vorticity contours (Figs. 5.5(c) and (d)) show that, for the quieter flow, there is an enhancement of vorticity close to the nozzle lip. To analyze the effect of the radiated sound, we compute the noise objective function defined as

$$\mathcal{I}_{\mathrm{noise}}(t) = \int_\Omega \left(p(\boldsymbol{x}, t) - \bar{p}(\boldsymbol{x})\right)^2 d\Omega, \tag{5.4}$$

where Ω is the cylindrical target surface at $r_{\mathrm{target}}/D = 7$ and the overall sound pressure level (OASPL) defined as

$$\text{OASPL (dB)} = 10\log_{10}\Big(\frac{p^2_{\mathrm{rms}}}{p^2_{\mathrm{ref}}}\Big),$$

where $p_{\mathrm{ref}} = 20\mu Pa$. Fig. 5.6(a) shows the comparison of the noise objective function $\mathcal{I}(t)$ for the baseline and controlled flows. For the quieter jet, the controller has been effective in reducing the noise over a control horizon of $\sim \Delta tc_\infty/D = 350$. Fig. 5.6(b) shows the time-and-azimuthal averaged OASPL for the baseline and controlled flows at the target surface Ω. The angle θ is measured from the downstream jet axis along a line connecting the nozzle exit to the target surface. The quieter flow shows a consistent reduction of 3-4 dB for all angles $> 40^0$ with a maximum reduction of approximately 4 dB at 90^0.

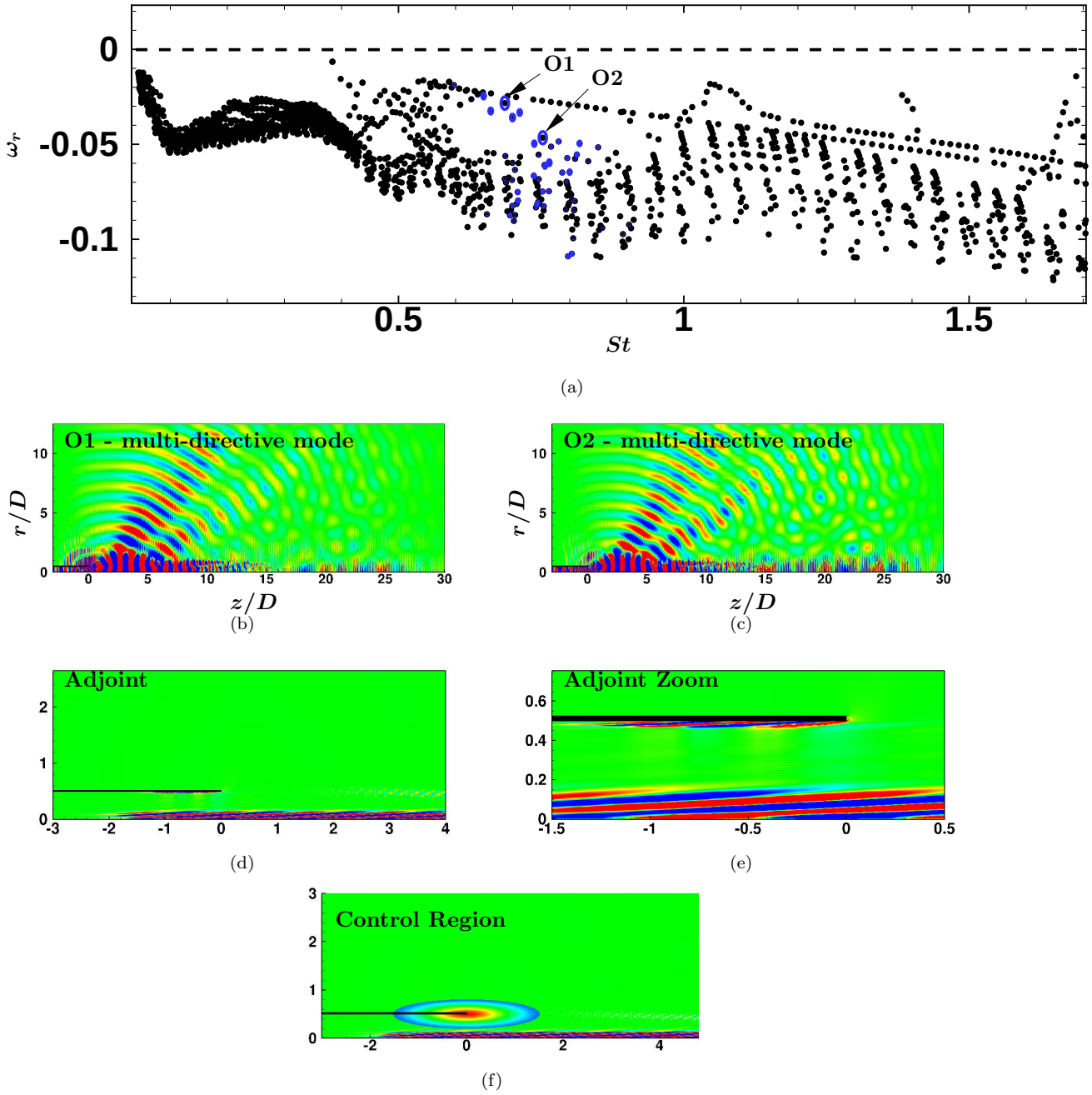

Figure 5.4: (a) Eigenspectrum showing the mode contribution to the optimal initial condition corresponding to the maximum transient response. Forward eigenmode (Real($\widehat{p}$)) for (b) O1 and (c) O2 which are dominant in the optimal initial condition. (d) Adjoint eigenmode (Real($\widehat{p}$)) for O1 and (e) near-nozzle view of the adjoint; (f) co-located control region for the V_z (control) - V_r (feedback) controller.

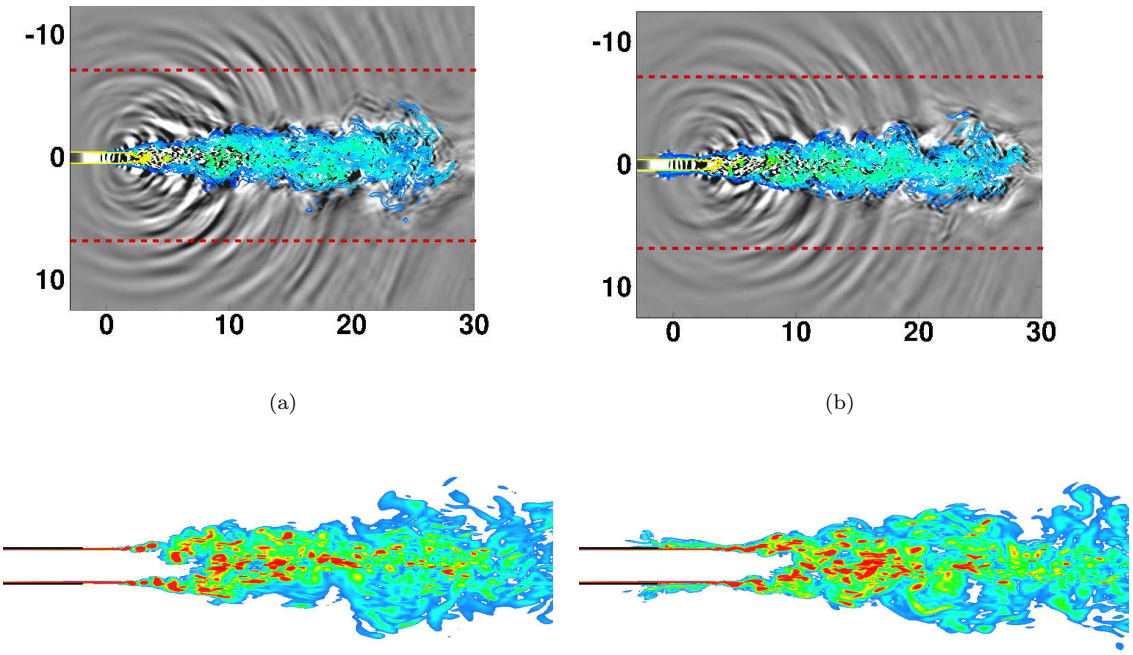

Figure 5.5: Vorticity-dilatation contours for (a) baseline T1 and the (b) controlled flow T2 at $tc_\infty/D = 163$; near-nozzle view of vorticity contours for (c) baseline and (d) controlled flows at $tc_\infty/D = 163$.

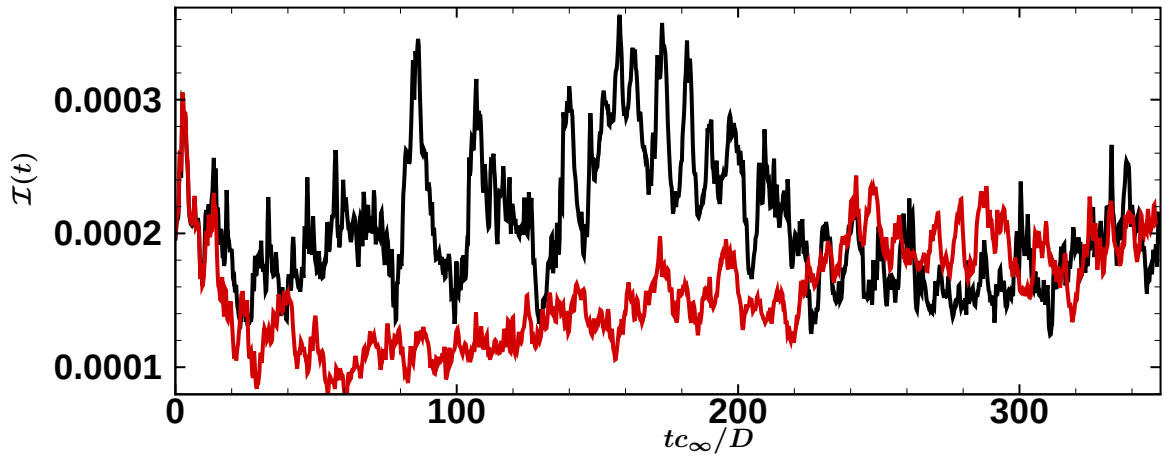

(a)

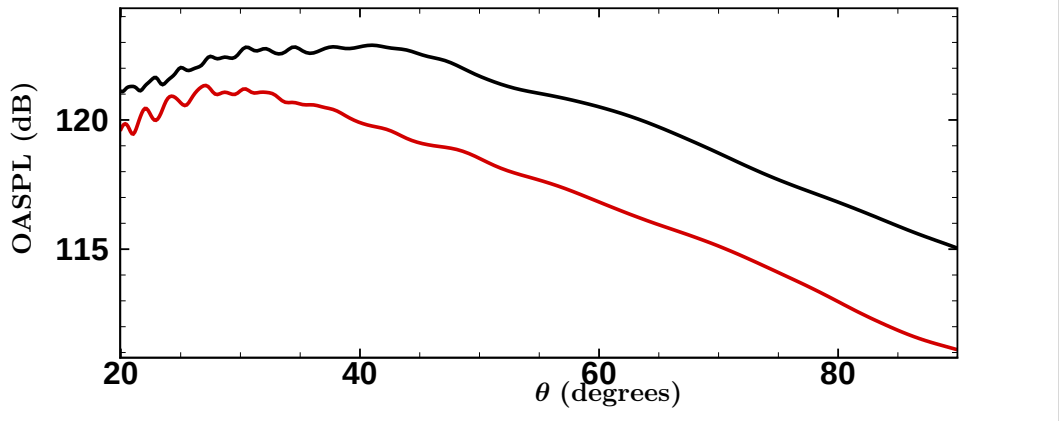

(b)

Figure 5.6: (a) Objective function $\mathcal{I}(t)$ and (b) overall sound pressure level on the target surface for the baseline (–) and controlled flows (–).

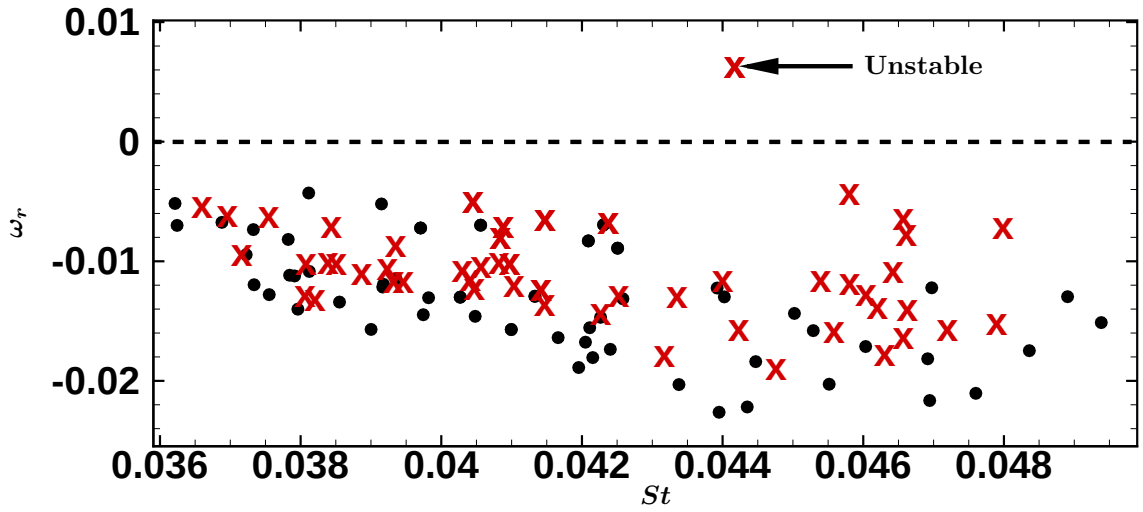

(a)

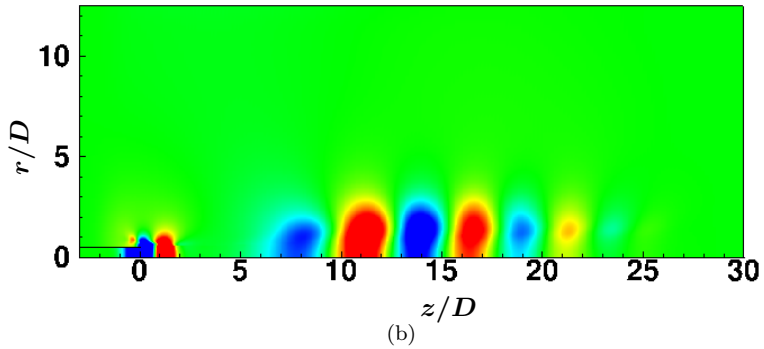

(b)

Figure 5.7: (a) Eigenspectrum comparison for the baseline (•) and controlled (×) time-and-azimuthal averaged flows at low Strouhal numbers. (b) Unstable eigenmode (Real($\widehat{p}$)) for the controlled flow showing non-radiative structure.

5.3.1 Global Eigenanalysis of Controlled Flows

Global eigenanalysis was performed for the time-and-azimuthal averaged flows for all the cases to identify changes in the spectrum and mode shapes. From Fig. 5.7(a), a fundamental change can be observed in the eigenspectrum for the quieter flows T2. Similar to what was observed in the axisymmetric case (Section 4.7), the stable modes have significant acoustic support in the far-field whereas the unstable global mode has a non-radiating pattern (Fig. 5.7(b)) with no acoustic footprint.

5.3.2 Mean Flow Alterations

Time-and-azimuthal averaged flow quantities are computed for all the flows to analyze the changes due to control. Fig. 5.8 shows the variation of the time-and-azimuthal averaged quantities for the turbulent

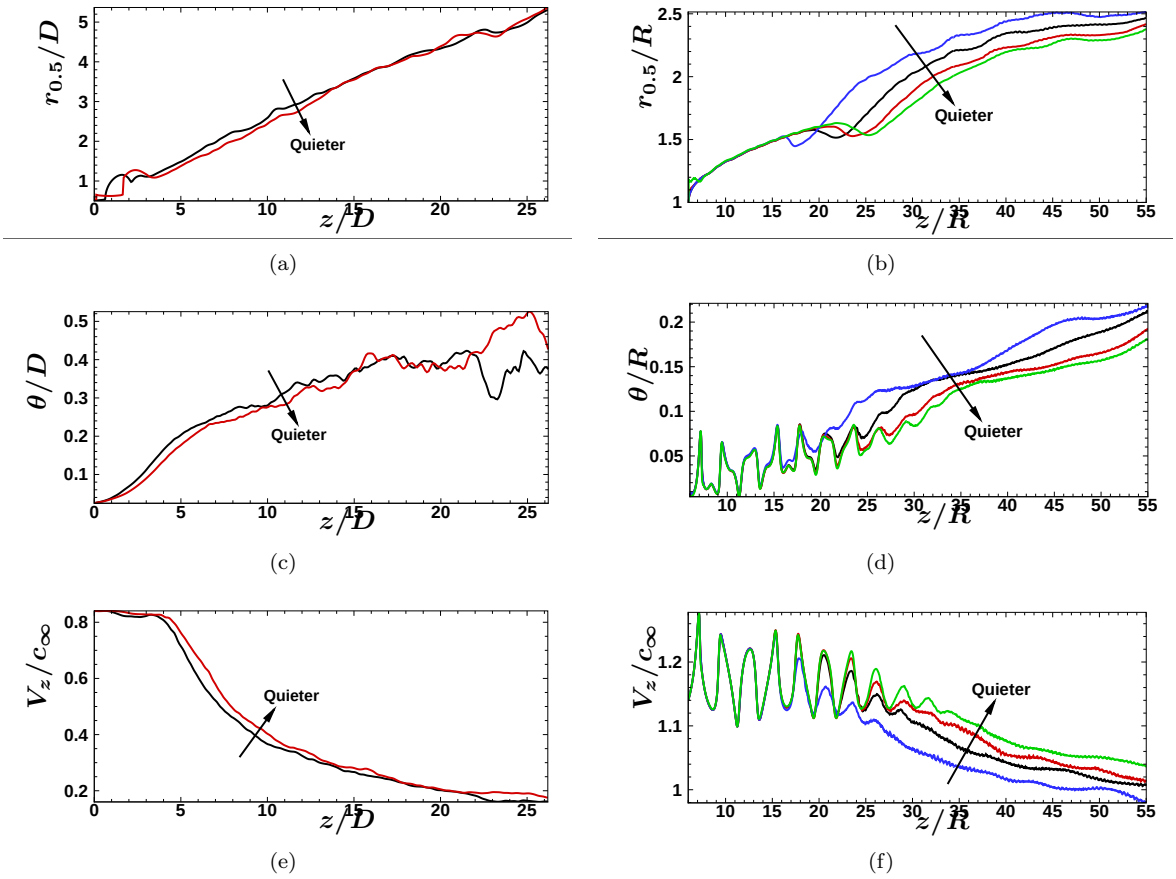

Figure 5.8: Comparison of time-averaged quantities for the baseline and controlled flows (turbulent jet (left) and axisymmetric jet(right)): (a) jet half-width (b) momentum thickness (c) centerline axial velocity for the baseline (–) and T2 (–) flows.

baseline and controlled jets and the time-averaged quantities for the axisymmetric jet for comparison. The axial variation of jet half-width (Fig. 5.8(a)), momentum thickness (Fig. 5.8(c)) and centerline axial velocity (Fig. 5.8(e)) show the same trends as in the axisymmetric case (Fig. 5.8(b), (d) and (f)). The time-and azimuthal averaged root mean square axial velocity for the baseline and controlled cases (Fig. 5.9(a) and (b)) show that the quieter jets have significantly reduced turbulence intensities. Fig. 5.9(c) shows the lipline variation of the mean square axial velocity for the baseline and controlled turbulent jets and has the same trend as the axisymmetric case (Fig. 5.9(d)).

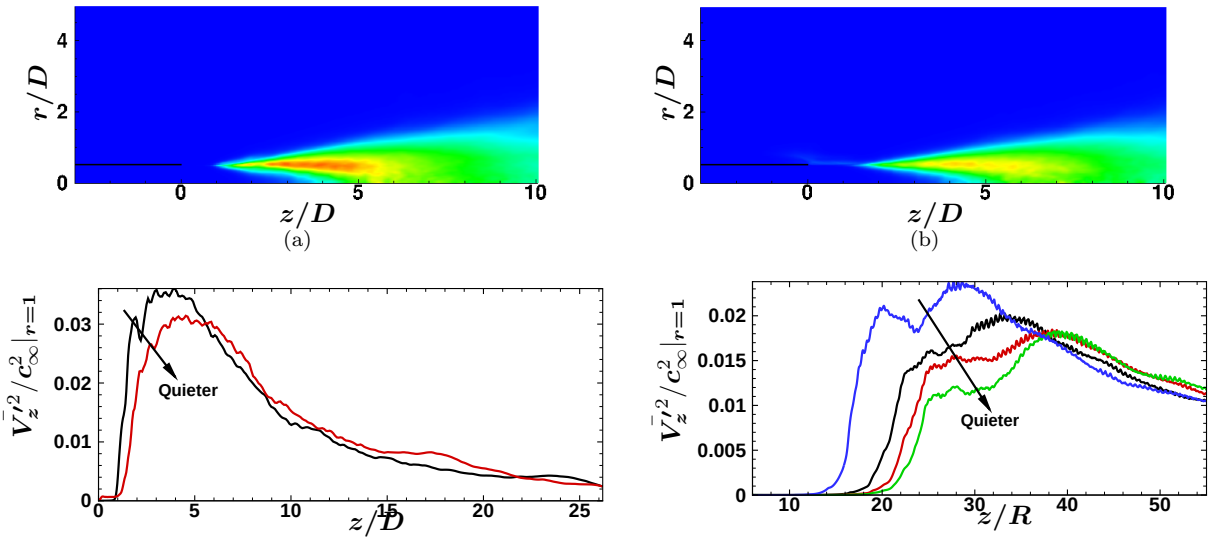

Figure 5.9: Comparison of time-averaged quantities : root mean square value of axial velocity for (a) baseline T1 and the (b) controlled flow T2; rms of axial velocity along the lipline for the (c) baseline T1 (–) and controlled flow T2 (–), and for the (d) baseline and controlled flows in the axisymmetric case.

Chapter 6

Conclusions and Future Work

6.1 Conclusions

A rational approach for co-located actuator(s)/sensor(s) selection and placement for linear feedback control of compressible flows has been developed. The strategy is flexible, and different types of control and feedback can be obtained. The control strategy was applied to three different flow control scenarios, the conclusions of which are given in this section.

6.1.1 Flow Control in a Mach 0.65 Diffuser

The method was first applied to control a separated boundary layer within an asymmetric diffuser at Mach 0.65. The shape and location of the co-located actuator(s)/sensor(s) region was found to be dependent on the specific control-feedback pair chosen for optimization. Complete global stabilization was achieved at $Re = 250$ for shorter diffusers ($L/\delta = 120$) for control gains within the stabilization window ($0.105 < \alpha < 0.108$), but complete stabilization could not be achieved for a higher Reynolds number, $Re = 350$ or longer domains ($L/\delta = 180$). The globally stabilizing control was found to be effective in complete suppression of vortex shedding for $Re = 250$. An error analysis of the predicted and computed eigenspectrum as a function of the control gain gave quantitative estimates of the extent to which the linear theory is valid.

6.1.2 Noise Reduction of an Axisymmetric Mach 1.5 Jet

A framework was developed to compute the global modes of axisymmetric jet flows. Direct numerical simulations were performed to obtain the equilibrium and time-averaged baseflows for an axisymmetric, Mach 1.5 jet, and the forward and adjoint global modes were computed for both baseflows. The equilibrium baseflow, characterized by an extended potential core region with weak shock cells, supported unstable global modes whose acoustic radiation was predominantly in the upstream direction. The time-averaged baseflow was absolutely stable and contained modes whose acoustic radiation was directed in both the upstream and downstream directions. Further analysis of the time-averaged baseflow case showed a wavemaker localized

near the nozzle exit, but with a spatial footprint that depended on the mode type. Projection of the nonlinear dynamics onto the modes did not indicate any particular modal dominance. The framework identified a co-located sensor and actuator for linear feedback control of supersonic jet noise. Direct numerical simulations of the controlled flows show a monotonic reduction of the radiated noise with increasing control gain. A global eigenanalysis showed that the quieter flows were characterized by an unstable mode that has little support in the acoustic field, whereas the louder flows had an eigenstructure very similar to the uncontrolled flow. Projecting the flow-field perturbations onto the global modes showed that for the quieter flows, acoustically inefficient unstable modes were highly amplified by the control and were more prominent in the flow-field than the acoustically efficient stable modes. The vortex pairing in the quieter flows was delayed further downstream and appears less vigorous than in the corresponding louder flows. The axial mean flow variations remained the same for the uncontrolled baseline as well as the controlled flows for $\sim$15 jet radii downstream of the nozzle beyond which changes became significant. A monotonic trend is observed in the downstream mean flow quantities (jet half-width, momentum thickness and centerline axial velocity) as a function of the control gain. A phase plot of the POD coefficients for the flows showed that the quieter flows were more regularized during the time interval spanning an uncontrolled loud event.

6.1.3 Noise Reduction of a Turbulent Mach 0.9 Jet

The active control strategy developed for the axisymmetric case was applied to reducing the noise of a Mach 0.9 turbulent jet. The baseline and controlled flows were computed using large eddy simulations. The global analysis of the time-and-azimuthal averaged baseline flow showed that at low Strouhal numbers ($St \sim 0.05 - 0.35$) the acoustically efficient global modes do not have a directive pattern, but with an increase in Strouhal number, the modes begin to exhibit acoustically efficient super-directive ($St \sim 0.40$) and multi-directive ($St \sim 1.40$) patterns. The transient growth was found to be dominated by multi-directive global modes at $St \sim 0.65 - 0.75$. The control was effective in reducing the noise. At the target surface at $r/D = 7$, a consistent reduction of 3-4 dB was obtained for all angles $> 40^0$, with a maximum reduction of approximately 4 dB at 90^0. The global analysis of the time-and-azimuthal averaged flow for the quiet jet revealed the existence of an unstable mode without any significant acoustic footprint at $St \sim 0.05$. The variation of mean quantities (jet half-width, momentum thickness and centerline axial velocity) at the centerline, as a function of the control gain, for the loud and quiet jets, also showed trends similar to the axisymmetric case. The quieter jet was found to have reduced turbulence intensities.

6.2 Future Work

The developed active control strategy has been shown to be effective in different flow control scenarios over a range of Mach numbers and Reynolds numbers. However, at present, the control procedure is purely computational in nature and demands additional work to extend it to develop experimentally realizable actuators. The major hurdles that we need to overcome are:

1. **Sensing measurable quantities** – To keep things simple, we currently restrict ourselves to utilizing a single control and a single feedback variable. Quantities such as density (as was done in the case of the Mach 0.65 diffuser) are not easily measurable. The control needs to be developed using physically realizable control and feedback variables. The current formulation is flexible in using any combination of control and feedback variables, but the efficacy of such actuators can be judged only after rigorous testing.

2. **Separate the control and actuation regions** – Co-located actuator/sensors are not realizable and we need to separate the control and actuator regions. We need to determine effective locations for both feedback and control, and this could lead to a more complex optimization problem with a larger parametric space.

3. **Control at the surface** – The present control strategy uses a forcing term in the right hand side of the Navier-Stokes equations, which means that the control is effective over a volume in space, which is difficult to realize in practice. We need to develop active control strategies for surface control techniques such as blowing/suction by incorporating the control through the boundary conditions. This can be done through the SAT based boundary condition approach which implements the boundary conditions using source terms in the governing equations, similar to how the control forcing is implemented currently.

4. **Time-delay in feedback systems** – There is always a delay between the time when a variable is sensed and when it is fedback to the controller. This has not been considered in the present case and might be critical in developing physically implementable feedback control systems.

Another aspect that deserves special attention is the discrete-adjoint method. The current formulation leads to unphysical oscillations in the adjoint field, in particular, close to boundaries. Such oscillations can adversely affect the actuator placement strategy. This can be overcome by using a dual-consistent formulation which has been shown to have physically meaningful adjoint fields (Hicken & Zingg, 2011).

Appendix A

Eigenvalue Solver for Inviscid Parallel Flows in Cartesian Coordinates

This appendix describes the shooting method to obtain the eigenvalues and eigenmodes for parallel flows in cartesian coordinates. The specific case considered is that of a compressible wall bounded shear layer in Section 3.2.1.

The Euler equations for compressible flow are linearized about the mean flow, and the following form is assumed for the perturbation of the primitive variables.

$$\{\rho', u', v', p'\} = \{\hat{\rho}(y), \hat{u}(y), \hat{v}(y), \hat{p}(y)\}e^{i(\alpha x - \sigma t)}$$

The resulting system of equations can be rearranged to give the following single ordinary differential equation for the pressure perturbation eigenfunction (Tam & Burton, 1984),

$$\frac{d^2\hat{p}}{dy^2} + \Big(\frac{2\alpha}{\hat{\omega}}\frac{d\bar{U}}{dy} - \frac{1}{\bar{\rho}}\frac{d\bar{\rho}}{dy}\Big)\frac{d\hat{p}}{dy} - (\alpha^2 - \bar{\rho}\hat{\omega}^2)\hat{p} = 0, \tag{A.1}$$

with $\hat{\omega} = \omega - \alpha\bar{U}$ and the boundary conditions

$$\frac{\partial\hat{p}}{\partial y} = 0 \quad \text{at} \quad y = \pm 1.$$

Knowing $\hat{p}$, the other perturbation eigenmodes can be obtained from Sandham (1989)

$$\begin{aligned}
\hat{u} &= \frac{\Big(-\dfrac{i\alpha\hat{p}}{\bar{\rho}} - \hat{v}D\bar{U}\Big)}{i(\alpha\bar{U} - \omega)} \\
\hat{v} &= \frac{-D\hat{p}}{i\bar{\rho}(\alpha\bar{U} - \sigma)} \\
\hat{\rho} &= -\frac{(\bar{\rho}(i\alpha\hat{u} + D\hat{v}) + \hat{v}D\bar{\rho})}{i(\alpha\bar{U} - \omega)}.
\end{aligned}$$

In regions 1 and 2, above and below the shear layer respectively, we have $\frac{d\bar{U}}{dy} = 0$, $\frac{d\bar{\rho}}{dy} = 0$. The Rayleigh

equation (A.1) reduces to

$$\frac{d^2\hat{p}}{dy^2} - (\alpha^2 - \bar{\rho}\hat{\omega}^2)\hat{p} = 0$$

which has the following exact solution for $\hat{p}$ above and below the shear layer Greenough *et al.* (1989)

$$\hat{p} = \begin{cases} A\cosh(\lambda(1-y)) & \text{above the shear layer} \\ B\cosh(\lambda(1+y)) & \text{below the shear layer} , \end{cases}$$

where $\lambda = \left\{\alpha^2 - \bar{\rho}(\omega - \alpha\bar{U})^2\right\}^{1/2}$ and $\hat{\omega} = \omega - \alpha\bar{U}$. The Rayleigh equation (A.1) is then solved using a shooting method. An initial guess for the eigenvalue $\omega = \omega_r + i\omega_i$ is the input. The analytical solution is used below the shear layer and integration is performed using the fourth-order Runge-Kutta method from $y = -0.25$ to $y = +0.25$ to find the solution within the shear layer. The difference in the slopes between the solution obtained and the exact solution at $y = +0.25$ is used to correct the guessed eigenvalue in a Newton-Raphson iteration procedure.

Appendix B

Linearization of the Viscous Terms in 2D Generalized Coordinates

The term-by-term linearization of the viscous terms in the linearized compressible Navier-Stokes equations are given in this appendix.

$$\hat{E}_v = \Big(\frac{\xi_x}{J}\Big)E_v + \Big(\frac{\xi_y}{J}\Big)F_v$$

Linearizing the viscous term $\dfrac{\partial}{\partial\xi}\hat{E}_v$,

$$\frac{\partial}{\partial\xi}\hat{E}'_v = \frac{\partial}{\partial\xi}\Big(\frac{\xi_x}{J}\Big)E'_v + \frac{\xi_x}{J}\frac{\partial}{\partial\xi}E'_v + \frac{\partial}{\partial\xi}\Big(\frac{\xi_y}{J}\Big)F'_v + \frac{\xi_y}{J}\frac{\partial}{\partial\xi}F'_v$$

$$\begin{aligned}
E'_v &= (E^\xi_v + E^\eta_v)' \\
&= E^\xi_{v_1}\frac{\partial}{\partial\xi}Q' + E^\xi_{v_2}Q' + E^\eta_{v_1}\frac{\partial}{\partial\eta}Q' + E^\eta_{v_2}Q' + E^\xi_{v_\mu}Q' + E^\eta_{v_\mu}Q' \\
&= E^\xi_{v_1}\frac{\partial}{\partial\xi}Q' + E^\eta_{v_1}\frac{\partial}{\partial\eta}Q' + \underbrace{(E^\xi_{v_2} + E^\eta_{v_2} + E^\xi_{v_\mu} + E^\eta_{v_\mu})}_{E_{v_2}}Q'
\end{aligned}$$

$$\begin{aligned}
\frac{\partial E'_v}{\partial\xi} &= \frac{\partial}{\partial\xi}E^\xi_{v_1}\frac{\partial}{\partial\xi}Q' + E^\xi_{v_1}\frac{\partial^2}{\partial\xi^2}Q' + \frac{\partial}{\partial\xi}\Big(E^\eta_{v_1}\frac{\partial}{\partial\eta}Q'\Big) + \frac{\partial}{\partial\xi}E_{v_2}Q' + E_{v_2}\frac{\partial}{\partial\xi}Q' \\
&= \left[\frac{\partial}{\partial\xi}E^\xi_{v_1}\frac{\partial}{\partial\xi} + E_{v_2}\frac{\partial}{\partial\xi} + E^\xi_{v_1}\frac{\partial^2}{\partial\xi^2} + \frac{\partial}{\partial\xi}\Big(E^\eta_{v_1}\frac{\partial}{\partial\eta}\Big) + \frac{\partial}{\partial\xi}E_{v_2}\right]Q' \\
\frac{\partial E'_v}{\partial\eta} &= \frac{\partial}{\partial\eta}\Big(E^\xi_{v_1}\frac{\partial}{\partial\xi}Q'\Big) + \frac{\partial}{\partial\eta}E^\eta_{v_1}\frac{\partial}{\partial\eta}Q' + E^\eta_{v_1}\frac{\partial^2}{\partial\eta^2}Q' + \frac{\partial}{\partial\eta}E_{v_2}Q' + E_{v_2}\frac{\partial}{\partial\eta}Q' \\
&= \left[\frac{\partial}{\partial\eta}\Big(E^\xi_{v_1}\frac{\partial}{\partial\xi}\Big) + E_{v_2}\frac{\partial}{\partial\eta} + \frac{\partial}{\partial\eta}E^\eta_{v_1}\frac{\partial}{\partial\eta} + E^\eta_{v_1}\frac{\partial^2}{\partial\eta^2} + \frac{\partial}{\partial\eta}E_{v_2}\right]Q'
\end{aligned}$$

Similarly,

$$\frac{\partial \hat{F}'_v}{\partial \eta} = \frac{\partial}{\partial \eta}\Big(\frac{\eta_x}{J}\Big)E'_v + \frac{\eta_x}{J}\frac{\partial}{\partial \eta}E'_v + \frac{\partial}{\partial \eta}\Big(\frac{\eta_y}{J}\Big)F'_v + \frac{\eta_y}{J}\frac{\partial}{\partial \eta}F'_v$$

$$E^{\xi}_{v_1} = \begin{bmatrix} 0 & 0 & 0 & 0 \\ (2\mu+\lambda)\xi_x u_\rho + \lambda\xi_y v_\rho & (2\mu+\lambda)\xi_x u_{\rho u} & \lambda\xi_y v_{\rho v} & 0 \\ \mu(\xi_y u_\rho + \xi_x v_\rho) & \mu\xi_y u_{\rho u} & \mu\xi_x v_{\rho v} & 0 \\ u\times(2,1) + v\times(3,1) & u\times(2,2) + v\times(3,2) & u\times(2,3) + v\times(3,3) & \\ +\frac{\mu}{Pr(\gamma-1)}\xi_x a^2_\rho & +\frac{\mu}{Pr(\gamma-1)}\xi_x a^2_{\rho u} & +\frac{\mu}{Pr(\gamma-1)}\xi_x a^2_{\rho v} & \frac{\mu}{Pr(\gamma-1)}\xi_x a^2_{\rho e} \end{bmatrix}$$

$$E^{\xi}_{v_2} = \begin{bmatrix} 0 & 0 & 0 & 0 \\ (2\mu+\lambda)\xi_x u_{\rho_\xi} + \lambda\xi_y v_{\rho_\xi} & (2\mu+\lambda)\xi_x u_{\rho u_\xi} & \lambda\xi_y v_{\rho v_\xi} & 0 \\ \mu(\xi_y u_{\rho_\xi} + \xi_x v_{\rho_\xi}) & \mu\xi_y u_{\rho u_\xi} & \mu\xi_x v_{\rho v_\xi} & 0 \\ u\times(2,1) + v\times(3,1) & u\times(2,2) + v\times(3,2) & u\times(2,3) + v\times(3,3) & \\ u_\rho((2\mu+\lambda)\xi_x u_\xi + \lambda\xi_y v_\xi) & u_{\rho u}((2\mu+\lambda)\xi_x u_\xi + \lambda\xi_y v_\xi) & & \\ \mu v_\rho(\xi_y u_\xi + \xi_x v_\xi) & & \mu v_{\rho v}(\xi_y u_\xi + \xi_x v_\xi) & \\ +\frac{\mu}{Pr(\gamma-1)}\xi_x a^2_{\rho_\xi} & +\frac{\mu}{Pr(\gamma-1)}\xi_x a^2_{\rho u_\xi} & +\frac{\mu}{Pr(\gamma-1)}\xi_x a^2_{\rho v_\xi} & \frac{\mu}{Pr(\gamma-1)}\xi_x a^2_{\rho e_\xi} \end{bmatrix}$$

$$F^{\xi}_{v_1} = \begin{bmatrix} 0 & 0 & 0 & 0 \\ \mu(\xi_y u_\rho + \xi_x v_\rho) & \mu\xi_y u_{\rho u} & \mu\xi_x v_{\rho v} & 0 \\ (\lambda\xi_x u_\rho + (2\mu+\lambda)\xi_y v_\rho & \lambda\xi_x u_{\rho u} & (2\mu+\lambda)\xi_y v_{\rho v} & 0 \\ u\times(2,1) + v\times(3,1) & u\times(2,2) + v\times(3,2) & u\times(2,3) + v\times(3,3) & \\ +\frac{\mu}{Pr(\gamma-1)}\xi_y a^2_\rho & +\frac{\mu}{Pr(\gamma-1)}\xi_y a^2_{\rho u} & +\frac{\mu}{Pr(\gamma-1)}\xi_y a^2_{\rho v} & \frac{\mu}{Pr(\gamma-1)}\xi_y a^2_{\rho e} \end{bmatrix}$$

$$F^{\xi}_{v_2} = \begin{bmatrix} 0 & 0 & 0 & 0 \\ \mu(\xi_y u_{\rho_\xi} + \xi_x v_{\rho_\xi}) & \mu\xi_y u_{\rho u_\xi} & \mu\xi_x v_{\rho v_\xi} & 0 \\ (\lambda\xi_x u_{\rho_\xi} + (2\mu+\lambda)\xi_y v_{\rho_\xi} & \lambda\xi_x u_{\rho u_\xi} & (2\mu+\lambda)\xi_y v_{\rho v_\xi} & 0 \\ u\times(2,1) + v\times(3,1) & u\times(2,2) + v\times(3,2) & u\times(2,3) + v\times(3,3) & \\ \mu u_\rho(\xi_y u_\xi + \xi_x v_\xi) & \mu u_{\rho u}(\xi_y u_\xi + \xi_x v_\xi) & & \\ v_\rho(\lambda\xi_x u_\xi + (2\mu+\lambda)\xi_y v_\xi) & & v_{\rho v}(\lambda\xi_x u_\xi + (2\mu+\lambda)\xi_y v_\xi) & \\ +\frac{\mu}{Pr(\gamma-1)}\xi_y a^2_{\rho_\xi} & +\frac{\mu}{Pr(\gamma-1)}\xi_y a^2_{\rho u_\xi} & +\frac{\mu}{Pr(\gamma-1)}\xi_y a^2_{\rho v_\xi} & \frac{\mu}{Pr(\gamma-1)}\xi_y a^2_{\rho e_\xi} \end{bmatrix}$$

$$E_v = \underbrace{\begin{bmatrix} 0 \\ \mu(\frac{29}{15}\xi_x u_\xi - \frac{1}{15}\xi_y v_\xi) \\ \mu(\xi_y u_\xi + \xi_x v_\xi) \\ u\mu(\frac{29}{15}\xi_x u_\xi - \frac{1}{15}\xi_y v_\xi) + \\ \mu v(\xi_y u_\xi + \xi_x v_\xi) + \\ \frac{\mu}{Pr(\gamma-1)}\xi_x \partial_\xi a^2 \end{bmatrix}}_{E_v^\xi} + \underbrace{\begin{bmatrix} 0 \\ \mu(\frac{29}{15}\eta_x u_\eta - \frac{1}{15}\eta_y v_\eta) \\ \mu(\eta_y u_\eta + \eta_x v_\eta) \\ u\mu(\frac{29}{15}\eta_x u_\eta - \frac{1}{15}\eta_y v_\eta) + \\ \mu v(\eta_y u_\eta + \eta_x v_\eta) + \\ \frac{\mu}{Pr(\gamma-1)}\eta_x \partial_\eta a^2 \end{bmatrix}}_{E_v^\eta}$$

and

$$F_v = \underbrace{\begin{bmatrix} 0 \\ \mu(\xi_y u_\xi + \xi_x v_\xi) \\ \mu(-\frac{1}{15}\xi_x u_\xi + \frac{29}{15}\xi_y v_\xi) \\ \mu u(\xi_y u_\xi + \xi_x v_\xi) + \\ v\mu(-\frac{1}{15}\xi_x u_\xi + \frac{29}{15}\xi_y v_\xi) + \\ \frac{\mu}{Pr(\gamma-1)}\xi_y \partial_\xi a^2 \end{bmatrix}}_{F_v^\xi} + \underbrace{\begin{bmatrix} 0 \\ \mu(\eta_y u_\eta + \eta_x v_\eta) \\ \mu(-\frac{1}{15}\eta_x u_\eta + \frac{29}{15}\eta_y v_\eta) \\ \mu u(\eta_y u_\eta + \eta_x v_\eta) + \\ v\mu(-\frac{1}{15}\eta_x u_\eta + \frac{29}{15}\eta_y v_\eta) + \\ \frac{\mu}{Pr(\gamma-1)}\eta_y \partial_\eta a^2 \end{bmatrix}}_{F_v^\eta}$$

We have

$$\mu = [(\gamma - 1)T]^n = \left(\frac{\gamma p}{\rho}\right)^n = (a^2)^n$$

where n = 0.666. Linearizing gives,

$$\mu' = n(a^2)^{n-1}(a^2)' = n(a^2)^{n-1}\begin{bmatrix} a_\rho^2 & a_{\rho u}^2 & a_{\rho v}^2 & a_{\rho e}^2 \end{bmatrix}\begin{bmatrix} \rho' \\ \rho u' \\ \rho v' \\ \rho e' \end{bmatrix}$$

$$E_{v_\mu}^\xi \text{ or } F_{v_\mu}^\xi = \begin{bmatrix} 0 & 0 & 0 & 0 \\ A \times n(a^2)^{n-1}a_\rho^2 & A \times n(a^2)^{n-1}a_{\rho u}^2 & A \times n(a^2)^{n-1}a_{\rho v}^2 & A \times n(a^2)^{n-1}a_{\rho e}^2 \\ B \times n(a^2)^{n-1}a_\rho^2 & B \times n(a^2)^{n-1}a_{\rho u}^2 & B \times n(a^2)^{n-1}a_{\rho v}^2 & B \times n(a^2)^{n-1}a_{\rho e}^2 \\ u \times (2,1) + v \times (3,1) & u \times (2,2) + v \times (3,2) & u \times (2,3) + v \times (3,3) & u \times (2,4) + v \times (3,4) \\ C \times n(a^2)^{n-1}a_\rho^2 & C \times n(a^2)^{n-1}a_{\rho u}^2 & C \times n(a^2)^{n-1}a_{\rho v}^2 & C \times n(a^2)^{n-1}a_{\rho e}^2 \end{bmatrix}$$

where for $E_{v_\mu}^\xi$

$$\begin{aligned} A &= \Big(\frac{29}{15}\xi_x u_\xi - \frac{1}{15}\xi_y v_\xi\Big) \\ B &= (\xi_y u_\xi + \xi_x v_\xi) \\ C &= \frac{1}{Pr(\gamma-1)}\xi_x \partial_\xi a^2 \end{aligned}$$

and for $F_{v_\mu}^\xi$

$$\begin{aligned} A &= (\xi_y u_\xi + \xi_x v_\xi) \\ B &= \Big(-\frac{1}{15}\xi_x u_\xi + \frac{29}{15}\xi_y v_\xi\Big) \\ C &= \frac{1}{Pr(\gamma-1)}\xi_y \partial_\xi a^2 \end{aligned}$$

with

$$\frac{\partial(0,u,v,a^2)}{\partial(\rho,\rho u,\rho v,\rho e)} = \begin{bmatrix} 0 & 0 & 0 & 0 \\ -\frac{u}{\rho} & \frac{1}{\rho} & 0 & 0 \\ -\frac{v}{\rho} & 0 & \frac{1}{\rho} & 0 \\ \gamma(\gamma-1)\Big(-\frac{\rho e}{\rho^2}+\frac{(u^2+v^2)}{\rho}\Big) & -\gamma(\gamma-1)\frac{u}{\rho} & -\gamma(\gamma-1)\frac{v}{\rho} & \gamma(\gamma-1)\frac{1}{\rho} \end{bmatrix}$$

Replacing ξ by η in the above matrices, we get $E^{\eta}_{v_1}, E^{\eta}_{v_2}, F^{\eta}_{v_1}, F^{\eta}_{v_2}$.

Hence the linearized viscous terms are given by

$$-\frac{J}{Re}\left[\frac{\partial}{\partial\xi}\hat{E}'_v+\frac{\partial}{\partial\eta}\hat{F}'_v\right] = -\frac{J}{Re}\left[\frac{\partial}{\partial\xi}\Big(\frac{\xi_x}{J}\Big)E'_v+\frac{\xi_x}{J}\frac{\partial}{\partial\xi}E'_v+\frac{\partial}{\partial\xi}\Big(\frac{\xi_y}{J}\Big)F'_v+\frac{\xi_y}{J}\frac{\partial}{\partial\xi}F'_v+ \frac{\partial}{\partial\eta}\Big(\frac{\eta_x}{J}\Big)E'_v+\frac{\eta_x}{J}\frac{\partial}{\partial\eta}E'_v+\frac{\partial}{\partial\eta}\Big(\frac{\eta_y}{J}\Big)F'_v+\frac{\eta_y}{J}\frac{\partial}{\partial\eta}F'_v\right]$$

$$= \left\{-\frac{J}{Re}\left[\frac{\partial}{\partial\xi}\Big(\frac{\xi_x}{J}\Big)+\frac{\partial}{\partial\eta}\Big(\frac{\eta_x}{J}\Big)\right]\right\}E'_v+\left\{-\frac{J}{Re}\left(\frac{\xi_x}{J}\right)\frac{\partial}{\partial\xi}E'_v\right\}+\left\{-\frac{J}{Re}\left(\frac{\eta_x}{J}\right)\frac{\partial}{\partial\eta}E'_v\right\}+ \left\{-\frac{J}{Re}\left[\frac{\partial}{\partial\xi}\Big(\frac{\xi_y}{J}\Big)+\frac{\partial}{\partial\eta}\Big(\frac{\eta_y}{J}\Big)\right]\right\}F'_v+\left\{-\frac{J}{Re}\left(\frac{\xi_y}{J}\right)\frac{\partial}{\partial\xi}F'_v\right\}+\left\{-\frac{J}{Re}\left(\frac{\eta_y}{J}\right)\frac{\partial}{\partial\eta}F'_v\right\}$$

We know from the transformation invariants that the first two terms are zero. Hence, we have,

$$-\frac{J}{Re}\left[\frac{\partial}{\partial\xi}\hat{E}'_v+\frac{\partial}{\partial\eta}\hat{F}'_v\right] = \left\{-\frac{1}{Re}\xi_x\frac{\partial}{\partial\xi}E'_v\right\}+\left\{-\frac{1}{Re}\eta_x\frac{\partial}{\partial\eta}E'_v\right\}+ \left\{-\frac{1}{Re}\xi_y\frac{\partial}{\partial\xi}F'_v\right\}+\left\{-\frac{1}{Re}\eta_y\frac{\partial}{\partial\eta}F'_v\right\}$$

Appendix C

Verification of Global Eigenvlaue Solver for Axisymmetric Configurations

C.1 Inviscid Test Case: Axisymmetric Parallel Free Shear Layer

The inviscid terms of the global eigenmode solver is validated using the standard test case for the inviscid instability of a parallel free shear layer. The baseflow uses a hyyperbolic tangent profile for the axial velocity at constant pressure and the baseflow density profile obtained using Crooco Busemann relations (Panickar & Raman (2009)). Figure C.1 show the baseflow profiles used for the verification.

$$\bar{V_z} = \frac{1}{2}\left[1+\tanh\left\{a\left(\frac{1}{r}-r\right)\right\}\right] \tag{C.1}$$

$$\bar{\rho} = \left[\frac{1}{2}(\gamma-1)\bar{V_z}(1-\bar{V_z})M_j^2+\bar{V_z}+\frac{T_\infty}{T_j}(1-\bar{V_z})\right]^{-1} \tag{C.2}$$

where a is a free parameter. Using eigenmodes of the form $[V_z', V_r', V_\theta', p'] \equiv [\widehat{V_z}, \widehat{V_r}, \widehat{V_\theta}, \widehat{p}]e^{i(\alpha x+n\theta-\omega t)}$ in the

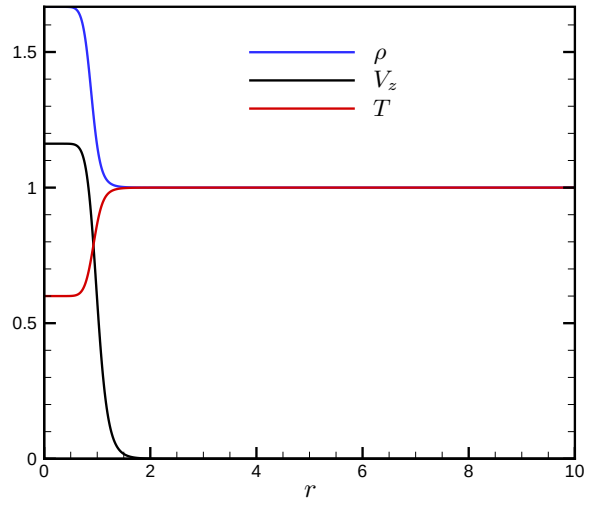

Figure C.1: Baseflow profiles.

inviscid governing equations, we obtain the Rayleigh equation for the pressure perturbation as

$$\frac{d^2\widehat{p}}{dr^2} + \left[\frac{1}{r} - \frac{1}{\bar{\rho}}\frac{d\bar{\rho}}{dr} + \frac{2\alpha}{\omega - \alpha\bar{V_z}}\frac{d\bar{V_z}}{dr}\right]\frac{d\widehat{p}}{dr} + \left[\bar{\rho}(\omega - \alpha\bar{V_z})^2 - \frac{n^2}{r^2} - \alpha^2\right]\widehat{p} = 0. \tag{C.3}$$

As $r \to 0$, $\bar{\rho} = \dfrac{\rho_j}{\rho_\infty} = \dfrac{T_j}{T_\infty}, \bar{u} = \dfrac{U_j}{c_\infty}$.

$$\frac{d^2\widehat{p}}{dr^2} + \frac{1}{r}\frac{d\widehat{p}}{dr} + \left[\frac{\rho_j}{\rho_\infty}\Big(\omega - \alpha\frac{U_j}{c_\infty}\Big)^2 - \frac{n^2}{r^2} - \alpha^2\right]\widehat{p} = 0$$

which has the solution

$$\widehat{p}(r=0) \quad = \quad AJ_n\left[\left(\sqrt{\frac{T_\infty}{T_j}\left(\omega - \alpha\frac{U_j}{c_\infty}\right)^2 - \alpha^2}\right)r\right]$$

and as $r \to \infty$, $\bar{\rho} = \dfrac{\rho_\infty}{\rho_\infty} = 1, \bar{u} = 0$.

$$\frac{d^2\widehat{p}}{dr^2} + \frac{1}{r}\frac{d\widehat{p}}{dr} + \left[\omega^2 - \frac{n^2}{r^2} - \alpha^2\right]\widehat{p} = 0$$

has the solution

$$\widehat{p}(r \to \infty) \quad = \quad BH_n^{(1)}\Big[\Big(\sqrt{\omega^2 - \alpha^2}\Big)r\Big].$$

A one-dimensional code based on the shooting method was developed to solve for the pressure eigenfunction. All the eigenfunctions can be derived from the pressure eigenfunction using the following relations

$$\begin{aligned}
\widehat{V_r} &= \frac{1}{i\rho(\omega - \alpha V_z)}\frac{d\widehat{p}}{dr} \\
\widehat{V_\theta} &= \frac{n\widehat{p}}{\rho(\omega - \alpha V_z)r} \\
\widehat{V_z} &= \frac{\alpha\widehat{p}}{\rho(\omega - \alpha V_z)} + \frac{\widehat{V_r}}{i(\omega - \alpha V_z)}\frac{dV_z}{dr} \\
\widehat{\rho} &= \frac{\widehat{p}}{\bar{a}^2} + \frac{\widehat{V_r}}{i(\omega - \alpha V_z)}\frac{d\rho}{dr} = \rho\widehat{p} + \frac{\widehat{V_r}}{i(\omega - \alpha V_z)}\frac{d\rho}{dr} \\
\widehat{T} &= \frac{\gamma\widehat{p} - T\widehat{\rho}}{\rho}
\end{aligned}$$

Azimuthal Mode	Wavenumber	Eigenvalue ($\omega_r + i\omega_i$)	
n	α	Shooting	Global
0	1	$0.1815 - 0.8709i$	$0.1813 - 0.8708i$
1	1	$0.2686 - 0.7447i$	$0.2684 - 0.7446i$
2	1	$0.2093 - 0.6903i$	$0.2096 - 0.6907i$

Table C.1: Comparison of eigenvalues from shooting method and global solver.

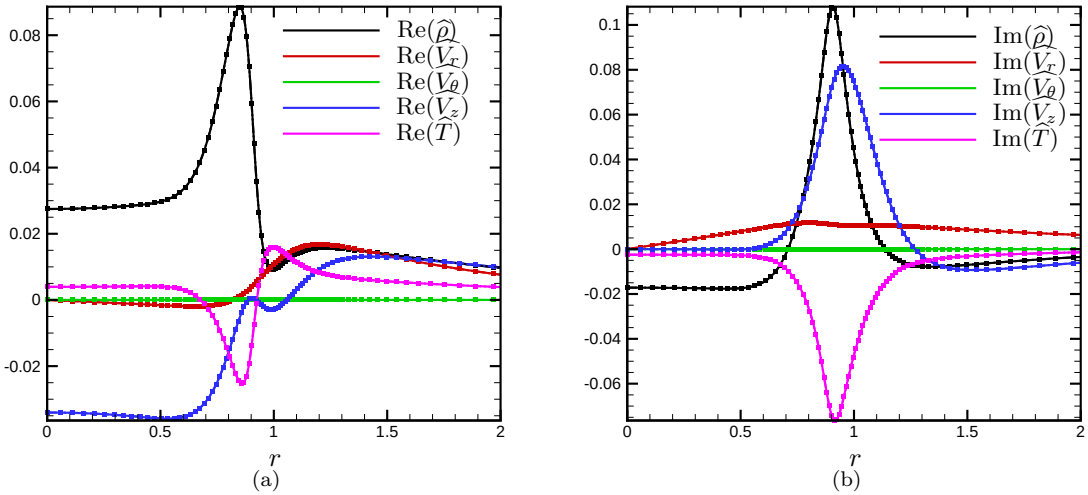

Figure C.2: $n = 0$: Comparison of eigenmodes : Shooting method (Symbols), Global eigenmode solver (Lines) (a) Real (b) Imaginary.

Three cases with different azimuthal mode numbers $n = 0, 1, 2$ were done to verify all possible axis condition scenarios. Table C.1 shows the comparison of the eigenvalues for the shooting method and the global eigenmode solver. Figs. C.2, C.3 and C.4 show the comparison of the real and imaginary parts of the eigenmodes for the three cases. Good quantitative comparison is obtained.

C.2 Viscous Test Case: Steady Axisymmetric Jet

An axisymmetric baseflow at $Re = 2000$ was computed using the Selective Frequency Damping technique. The eigenaanalysis was done to compute the global modes. One of stable modes were superposed on the steady baseflow, and the time evolution of the mode was obtained from the direct numerical simulations. Fig. C.5(a) shows the domain, the probe locations are shown in Fig. C.5(b), and the perturbation growth at the probe locations are shown in Figs. C.5(c) and (d).

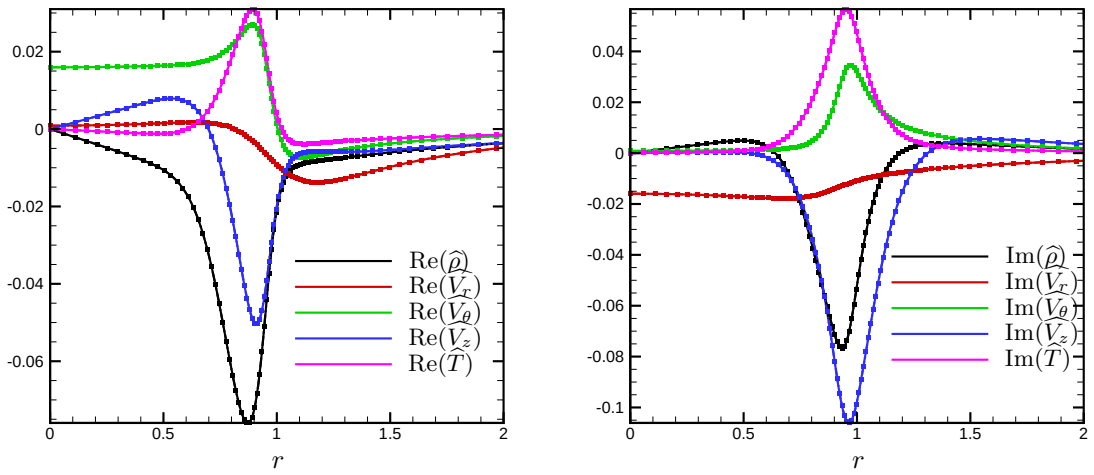

(a) (b)

Figure C.3: $n = 1$: Comparison of eigenmodes : Shooting method (Symbols), Global eigenmode solver (Lines) (a) Real (b) Imaginary.

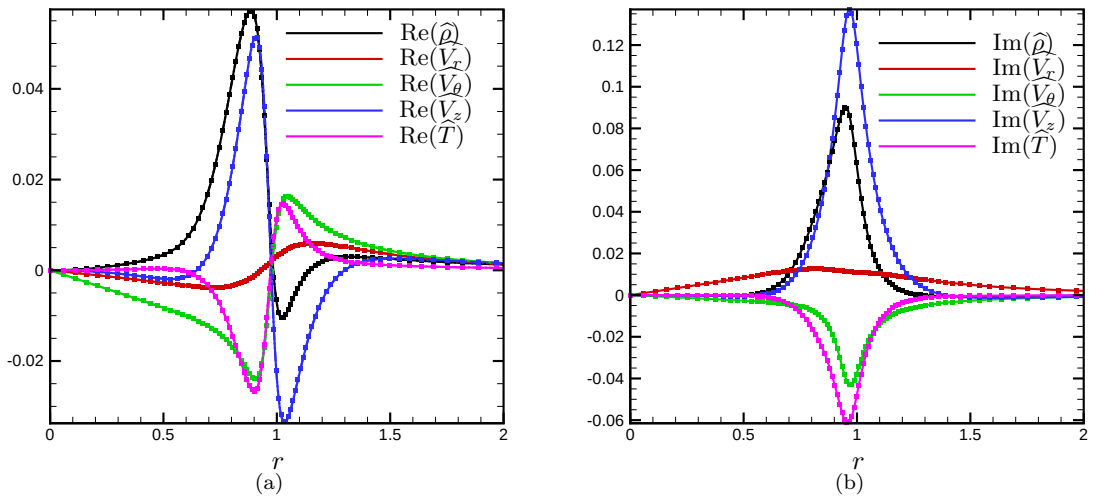

(a) (b)

Figure C.4: $n = 2$: Comparison of eigenmodes : Shooting method (Symbols), Global eigenmode solver (Lines) (a) Real (b) Imaginary.

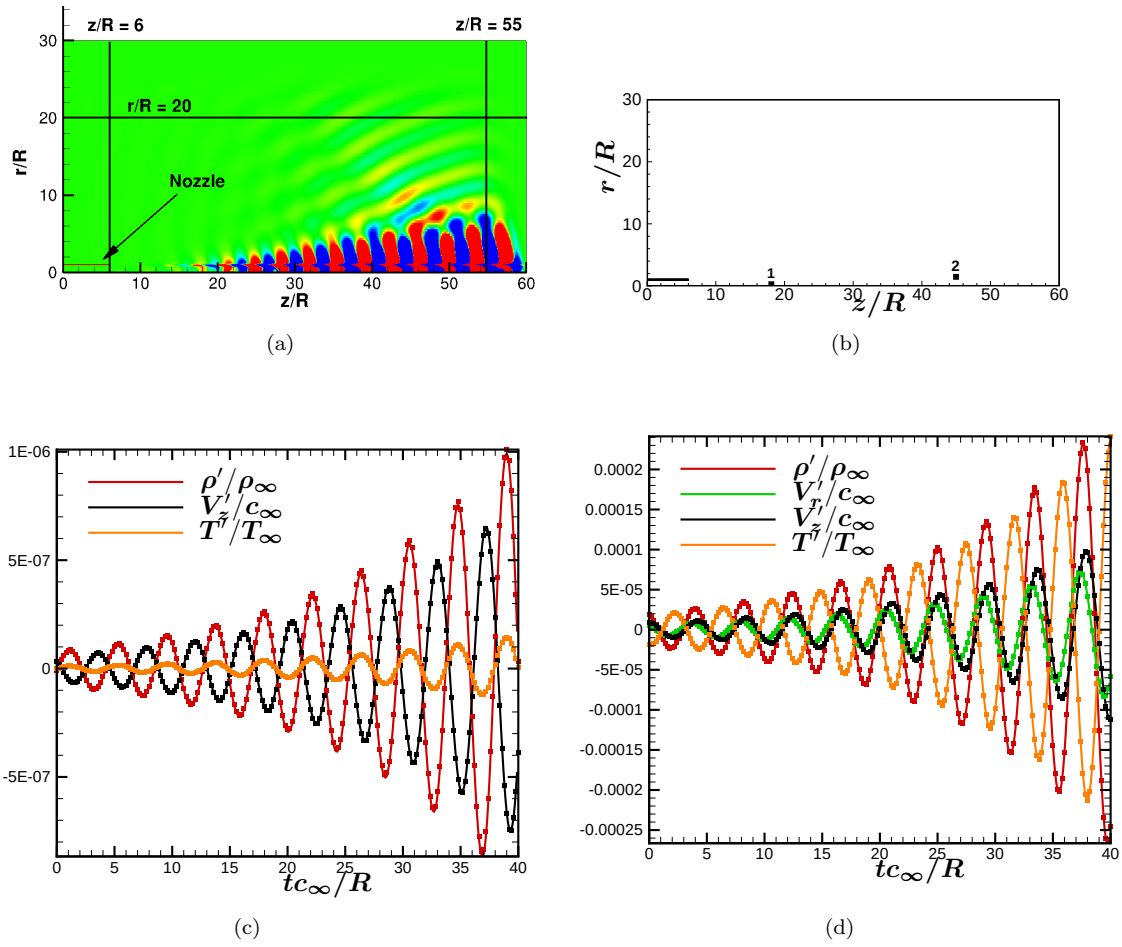

Figure C.5: (a) Computational domain showing the sponge zones, (b) probe locations, and comparison of linear stability analysis (lines) and DNS (symbols): (c) at probe 1 (d) at probe 2.

Appendix D

Axisymmetric Jet: Terms in Governing Equations and Boundary Conditions

D.1 Viscous terms

The viscous terms on the right hand side of (4.1) are given by

$$
\begin{aligned}
S_r = \frac{1}{Re}\Bigg[\mu\Bigg(\Bigg(2+\frac{\lambda}{\mu}\Bigg)\frac{\partial^2 V_r}{\partial r^2} \quad &+ \quad \Bigg(2+\frac{\lambda}{\mu}\Bigg)\frac{1}{r}\frac{\partial V_r}{\partial r} + \Bigg(1+\frac{\lambda}{\mu}\Bigg)\frac{1}{r}\frac{\partial^2 V_r}{\partial r \partial\theta} + \Bigg(1+\frac{\lambda}{\mu}\Bigg)\frac{\partial^2 V_z}{\partial z \partial r} + \frac{1}{r^2}\frac{\partial V_r^2}{\partial \theta^2} \\
&- \quad \Bigg(3+\frac{\lambda}{\mu}\Bigg)\frac{1}{r^2}\frac{\partial V_\theta}{\partial\theta} + \frac{\partial^2 V_r}{\partial z^2} - \Bigg(2+\frac{\lambda}{\mu}\Bigg)\frac{V_r}{r^2}\Bigg) \\
&+ \quad \frac{\partial\mu}{\partial r}\Bigg(\Bigg(2+\frac{\lambda}{\mu}\Bigg)\frac{\partial V_r}{\partial r} + \frac{\lambda}{\mu}\frac{V_r}{r} + \frac{\lambda}{\mu}\frac{1}{r}\frac{\partial V_\theta}{\partial\theta} + \frac{\lambda}{\mu}\frac{\partial V_z}{\partial z}\Bigg) \\
&+ \quad \frac{\partial\mu}{\partial\theta}\Bigg(\frac{1}{r}\frac{\partial V_\theta}{\partial r} + \frac{1}{r^2}\frac{\partial V_r}{\partial\theta} - \frac{V_\theta}{r^2}\Bigg) + \frac{\partial\mu}{\partial z}\Bigg(\frac{\partial V_r}{\partial z} + \frac{\partial V_z}{\partial r}\Bigg)\Bigg]
\end{aligned}
$$

$$
\begin{aligned}
S_\theta = \frac{1}{Re}\Bigg[\mu\Bigg(\frac{\partial^2 V_\theta}{\partial r^2} \quad &+ \quad \Bigg(1+\frac{\lambda}{\mu}\Bigg)\frac{1}{r}\frac{\partial^2 V_\theta}{\partial\theta\partial r} + \Bigg(2+\frac{\lambda}{\mu}\Bigg)\frac{1}{r^2}\frac{\partial^2 V_\theta}{\partial\theta^2} + \Bigg(3+\frac{\lambda}{\mu}\Bigg)\frac{1}{r^2}\frac{\partial V_r}{\partial\theta} \\
&+ \quad \Bigg(1+\frac{\lambda}{\mu}\Bigg)\frac{1}{r}\frac{\partial^2 V_z}{\partial\theta\partial z} + \frac{\partial^2 V_\theta}{\partial z^2} + \frac{1}{r}\frac{\partial V_\theta}{\partial r} - \frac{V_\theta}{r^2}\Bigg) \\
&+ \quad \frac{\partial\mu}{\partial r}\Bigg(\frac{\partial V_\theta}{\partial r} + \frac{1}{r}\frac{\partial V_r}{\partial\theta} - \frac{V_\theta}{r}\Bigg) \\
&+ \quad \frac{\partial\mu}{\partial\theta}\Bigg(\Bigg(2+\frac{\lambda}{\mu}\Bigg)\frac{1}{r^2}\frac{\partial V_\theta}{\partial\theta} + \frac{(2\mu+\lambda)}{\mu}\frac{V_r}{r^2} + \frac{\lambda}{\mu}\frac{1}{r}\frac{\partial V_r}{\partial r} + \frac{\lambda}{\mu}\frac{1}{r}\frac{\partial V_z}{\partial z}\Bigg) \\
&+ \quad \frac{\partial\mu}{\partial z}\Bigg(\frac{\partial V_\theta}{\partial z} + \frac{1}{r}\frac{\partial V_z}{\partial\theta}\Bigg)\Bigg]
\end{aligned}
$$

$$
\begin{aligned}
S_z = \frac{1}{Re}\Bigg[\mu\Bigg(\frac{\partial^2 V_z}{\partial r^2} &+ \frac{1}{r^2}\frac{\partial^2}{\partial\theta^2} + \left(2+\frac{\lambda}{\mu}\right)\frac{\partial^2 V_z}{\partial z^2} + \left(1+\frac{\lambda}{\mu}\right)\frac{\partial^2 V_r}{\partial r \partial z} + \frac{1}{r}\frac{\partial V_z}{\partial r} \\
&+ \left(1+\frac{\lambda}{\mu}\right)\frac{1}{r}\frac{\partial V_r}{\partial z} + \left(1+\frac{\lambda}{\mu}\right)\frac{1}{r}\frac{\partial^2 V_\theta}{\partial\theta\partial z}\Bigg) \\
&+ \frac{\partial\mu}{\partial r}\left(\frac{\partial V_z}{\partial r}+\frac{\partial V_r}{\partial z}\right) + \frac{\partial\mu}{\partial\theta}\left(\frac{1}{r^2}\frac{\partial V_z}{\partial\theta}+\frac{1}{r}\frac{\partial V_\theta}{\partial z}\right) \\
&+ \frac{\partial\mu}{\partial z}\left(\left(2+\frac{\lambda}{\mu}\right)\frac{\partial V_z}{\partial z} + \frac{\lambda}{\mu}\frac{\partial V_r}{\partial r} + \frac{\lambda}{\mu}\frac{V_r}{r} + \frac{\lambda}{\mu}\frac{1}{r}\frac{\partial V_\theta}{\partial\theta}\right)\Bigg]
\end{aligned}
$$

$$
\begin{aligned}
S_T &= \frac{\gamma}{RePr}\left[\kappa\left(\frac{\partial^2 T}{\partial r^2}+\frac{1}{r}\frac{\partial T}{\partial r}+\frac{1}{r^2}\frac{\partial^2 T}{\partial\theta^2}+\frac{\partial^2 T}{\partial z^2}\right)+\frac{\partial\kappa}{\partial r}\frac{\partial T}{\partial r}+\frac{1}{r^2}\frac{\partial\kappa}{\partial\theta}\frac{\partial T}{\partial\theta}+\frac{\partial\kappa}{\partial z}\frac{\partial T}{\partial z}\right] \\
&+ \frac{\gamma(\gamma-1)}{Re}\mu\Bigg[\frac{\partial V_r}{\partial r}\left((2\mu+\lambda)\frac{\partial V_r}{\partial r}+\lambda\frac{V_r}{r}+\lambda\frac{1}{r}\frac{\partial V_\theta}{\partial\theta}+\lambda\frac{\partial V_z}{\partial z}\right) \\
&+ \left(\frac{\partial V_r}{\partial\theta}+\frac{\partial V_\theta}{\partial r}-\frac{V_\theta}{r}\right)\left(\frac{\partial V_\theta}{\partial r}+\frac{1}{r}\frac{\partial V_r}{\partial\theta}-\frac{V_r}{r}\right) \\
&+ \left(\frac{1}{r}\frac{\partial V_\theta}{\partial\theta}+\frac{V_r}{r}\right)\left((2\mu+\lambda)\frac{1}{r}\frac{\partial V_\theta}{\partial\theta}+(2\mu+\lambda)\frac{V_r}{r}+\lambda\frac{\partial V_r}{\partial r}+\lambda\frac{\partial V_z}{\partial z}\right) \\
&+ \left(\frac{\partial V_\theta}{\partial z}+\frac{1}{r}\frac{\partial V_z}{\partial\theta}\right)\left(\frac{\partial V_\theta}{\partial z}+\frac{1}{r}\frac{\partial V_z}{\partial\theta}\right) \\
&+ \frac{\partial V_z}{\partial z}\left((2\mu+\lambda)\frac{\partial V_z}{\partial z}+\lambda\frac{\partial V_r}{\partial r}+\lambda\frac{V_r}{r}+\lambda\frac{1}{r}\frac{\partial V_\theta}{\partial\theta}\right)+\left(\frac{\partial V_r}{\partial z}+\frac{\partial V_z}{\partial r}\right)\left(\frac{\partial V_z}{\partial r}+\frac{\partial V_r}{\partial z}\right)\Bigg]
\end{aligned}
$$

D.2 Additional Boundary Condition Details

D.2.1 Centerline treatment

The governing equations in cylindrical coordinates have a singularity at the centerline ($r = 0$) and should be treated appropriately. To obtain the modified governing equations at the centerline, the Fourier expansion of the flow variables is used and physical constraints on the Fourier coefficients are derived imposing the properties of symmetry and regularity in physical space (Lewis & Bellan, 1990). Since the flow under consideration is axisymmetric, we obtain a set of conditions at the centerline which the flow variables should satisfy. Depending on how the variables transform under coordinate transformation, they are classified as scalar-like or vector-like. The variables ρ, V_z and T are scalar-like and V_r and V_θ are vector-like. This section outlines the centerline treatment of both these classes of variables.

For a scalar-like quantity $f(r,\theta)$, consider the Fourier expansion

$$f(r,\theta) = \sum_{m=-\infty}^{\infty} f_m(r)e^{im\theta}.$$

The symmetry condition $f(r,\theta) = f(-r,\theta+\pi)$ imposes a condition on the Fourier coefficients given by

$$f_m(r) = (-1)^m f_m(-r), \tag{D.1}$$

and the regularity condition gives the least restrictive form of $f_m(r)$ as

$$f_m(r) \sim r^{|m|}. \tag{D.2}$$

Combining the symmetry and regularity conditions, we obtain the centerline conditions for a scalar as

$$\begin{aligned} \frac{\partial f_0}{\partial r} &= 0 \quad m = 0 \\ f_m &= 0 \quad m \neq 0. \end{aligned} \tag{D.3}$$

Now, for the vector-like quantities, V_r and V_θ, consider the Fourier expansions

$$\begin{aligned} V_r &= \sum_{m=-\infty}^{\infty} V_{rm}e^{im\theta}, \\ V_\theta &= \sum_{m=-\infty}^{\infty} V_{\theta m}e^{im\theta}. \end{aligned} \tag{D.4}$$

The symmetry and regularity conditions for the cartesian velocities V_x and V_y give the conditions as

$$\begin{aligned} V_{r0} = V_{\theta 0} = 0 \quad & m = 0, \\ \frac{\partial V_{rm}}{\partial r} = \frac{\partial V_{\theta m}}{\partial r} = 0 \quad & |m| = 1 \\ V_{rm} = V_{\theta m} = 0 \quad & |m| \geq 2 \end{aligned} \tag{D.5}$$

Using (D.3) and (D.5), we get the centerline conditions for axisymmetric flow as (Salgado & Sandham, 2007)

$$\frac{\partial \rho}{\partial r} = V_r = V_\theta = \frac{\partial V_z}{\partial r} = \frac{\partial T}{\partial r} = 0.$$

D.2.2 Far-field Simultaneous Approximation Term (SAT) treatment

The SAT treatment is based on a weak enforcement of the boundary conditions with the boundary source terms in (4.1) that are active only at the boundaries. Following the notation in Svärd *et al.* (2007), the governing equations with the SAT boundary terms are given by

$$\frac{\partial \boldsymbol{Q}}{\partial t} = \boldsymbol{R}(\boldsymbol{Q}) + \boldsymbol{P^{-1}E_1T_r\Lambda_r^+T_r^{-1}}\eta_r(\boldsymbol{Q}-\boldsymbol{Q}_{\text{target}}) + \boldsymbol{P^{-1}E_1T_z\Lambda_z^+T_z^{-1}}\xi_z(\boldsymbol{Q}-\boldsymbol{Q}_{\text{target}}), \tag{D.6}$$

where $\boldsymbol{R}(\boldsymbol{Q})$ is the Navier-Stokes right hand side and $\xi_z \equiv \frac{\partial \xi}{\partial z}$ and $\eta_r \equiv \frac{\partial \eta}{\partial r}$ are the grid metrics in the ξ and η directions, respectively. The rotation matrices and eigenvalue matrices in the axial and radial directions for the SAT treatment are given in (D.7)-(D.10). The eigenvalue matrix, $\boldsymbol{\Lambda^+_{z,r}}$ ensures that the boundary conditions are applied only on the incoming characteristics. For example, in the z-direction, $\boldsymbol{\Lambda_z^+} = (\boldsymbol{\Lambda_z} + |\boldsymbol{\Lambda_z}|)/2$ on $z = 0$ and $\boldsymbol{\Lambda_z^+} = (\boldsymbol{\Lambda_z} - |\boldsymbol{\Lambda_z}|)/2$ on $z = z_{\max}$. The diagonal and rotation matrices are,

$$\boldsymbol{\Lambda_z} = \begin{bmatrix} V_z & & & & & \\ & V_z & & & & \\ & & V_z & & & \\ & & & (V_z - \sqrt{T}) & & \\ & & & & (V_z + \sqrt{T}) \end{bmatrix} \tag{D.7}$$

$$\boldsymbol{T_z} = \begin{bmatrix} -\frac{\rho}{T} & 0 & 0 & \frac{\rho}{(\gamma-1)T} & \frac{\rho}{(\gamma-1)T} \\ 0 & 0 & 1 & 0 & 0 \\ 0 & 1 & 0 & 0 & 0 \\ 0 & 0 & 0 & -\frac{1}{(\gamma-1)\sqrt{T}} & \frac{1}{(\gamma-1)\sqrt{T}} \\ 1 & 0 & 0 & 1 & 1 \end{bmatrix} \quad \text{and} \quad \boldsymbol{T_z^{-1}} = \begin{bmatrix} -\frac{(\gamma-1)T}{\gamma\rho} & 0 & 0 & 0 & \frac{1}{\gamma} \\ 0 & 0 & 1 & 0 & 0 \\ 0 & 1 & 0 & 0 & 0 \\ \frac{(\gamma-1)T}{2\gamma\rho} & 0 & 0 & -\frac{(\gamma-1)\sqrt{T}}{2} & \frac{(\gamma-1)}{2\gamma} \\ \frac{(\gamma-1)T}{2\gamma\rho} & 0 & 0 & \frac{(\gamma-1)\sqrt{T}}{2} & \frac{(\gamma-1)}{2\gamma} \end{bmatrix} \tag{D.8}$$

$$\boldsymbol{\Lambda_r} = \begin{bmatrix} V_r & & & & \\ & V_r & & & \\ & & V_r & & \\ & & & (V_r - \sqrt{T}) & \\ & & & & (V_r + \sqrt{T}) \end{bmatrix} \tag{D.9}$$

$$\boldsymbol{T_r} = \begin{bmatrix} -\frac{\rho}{T} & 0 & 0 & \frac{\rho}{(\gamma-1)T} & \frac{\rho}{(\gamma-1)T} \\ 0 & 0 & 0 & -\frac{1}{(\gamma-1)\sqrt{T}} & \frac{1}{(\gamma-1)\sqrt{T}} \\ 0 & 0 & 1 & 0 & 0 \\ 0 & 1 & 0 & 0 & 0 \\ 1 & 0 & 0 & 1 & 1 \end{bmatrix} \quad \text{and} \quad \boldsymbol{T_r^{-1}} = \begin{bmatrix} -\frac{(\gamma-1)T}{\gamma\rho} & 0 & 0 & 0 & \frac{1}{\gamma} \\ 0 & 0 & 0 & 1 & 0 \\ 0 & 0 & 1 & 0 & 0 \\ \frac{(\gamma-1)T}{2\gamma\rho} & -\frac{(\gamma-1)\sqrt{T}}{2} & 0 & 0 & \frac{(\gamma-1)}{2\gamma} \\ \frac{(\gamma-1)T}{2\gamma\rho} & \frac{(\gamma-1)\sqrt{T}}{2} & 0 & 0 & \frac{(\gamma-1)}{2\gamma} \end{bmatrix} \tag{D.10}$$

.

D.2.3 Nozzle Wall Treatment

Since the SAT approach does a weak enforcement of the boundary conditions, the no-slip and isothermal wall conditions are not strictly satisfied at the nozzle walls. This may lead to spurious oscillations in the global eigenmodes. Hence, a characteristic based treatment is used to strictly enforce the boundary conditions for the no-slip ($V_r = V_\theta = V_z = 0$), isothermal ($T = 1$) nozzle walls. Hence, on the nozzle walls, only the continuity equation, with the modified characteristic terms, is solved. For the nozzle wall with the wall normal in the $+z$ direction, the equations reduce to

$$\frac{\partial \rho}{\partial t} + \Big(V_r \frac{\partial \rho}{\partial r} + \frac{V_\theta}{r}\frac{\partial \rho}{\partial \theta}\Big) + \rho\Big(\frac{\partial V_r}{\partial r} + \frac{V_r}{r} + \frac{1}{r}\frac{\partial V_\theta}{\partial \theta}\Big) + \Big(\boldsymbol{T_z}\boldsymbol{\Lambda_z}\boldsymbol{T_z^{-1}}\frac{\partial \boldsymbol{Q}}{\partial z}\Big)_{\rho,\text{wall}(+z)} = 0, \tag{D.11}$$

where the z derivative terms in the continuity equation have been replaced with the characteristic terms in that direction. The relation between the incoming and outgoing wave amplitudes to impose $V_z = 0$ on the

wall is

$$\boldsymbol{\Lambda_z T_z^{-1}} \frac{\partial \boldsymbol{Q}}{\partial z}\bigg|_{\text{incoming}} = -\boldsymbol{\Lambda_z T_z^{-1}} \frac{\partial \boldsymbol{Q}}{\partial z}\bigg|_{\text{outgoing}}. \tag{D.12}$$

This gives

$$\Big(\boldsymbol{T_z \Lambda_z T_z^{-1}} \frac{\partial \boldsymbol{Q}}{\partial z}\Big)_{\rho,\text{wall}(+z)} = \rho \frac{\partial V_z}{\partial z} - \frac{\sqrt{T}}{\gamma}\frac{\partial \rho}{\partial z} - \frac{\rho}{\gamma\sqrt{T}}\frac{\partial T}{\partial z}. \tag{D.13}$$

Similarly, for the wall normal in the r direction, we have

$$\frac{\partial \rho}{\partial t} + \Big(\frac{V_\theta}{r}\frac{\partial \rho}{\partial \theta} + V_z \frac{\partial \rho}{\partial z}\Big) + \rho\Big(\frac{1}{r}\frac{\partial V_\theta}{\partial \theta} + \frac{\partial V_z}{\partial z}\Big) + \Big(\boldsymbol{T_r \Lambda_r T_r^{-1}} \frac{\partial \boldsymbol{Q}}{\partial r}\Big)_{\rho,\text{wall}(+,-r)} = 0. \tag{D.14}$$

For the wall normal in the $+r$ direction, we get

$$\Big(\boldsymbol{T_r \Lambda_r T_r^{-1}} \frac{\partial \boldsymbol{Q}}{\partial r}\Big)_{\rho,\text{wall}(+r)} = \rho \frac{\partial V_r}{\partial r} - \frac{\sqrt{T}}{\gamma}\frac{\partial \rho}{\partial r} - \frac{\rho}{\gamma\sqrt{T}}\frac{\partial T}{\partial r}, \tag{D.15}$$

and for the wall normal in the $-r$ direction, we get

$$\Big(\boldsymbol{T_r \Lambda_r T_r^{-1}} \frac{\partial \boldsymbol{Q}}{\partial r}\Big)_{\rho,\text{wall}(-r)} = \rho \frac{\partial V_r}{\partial r} + \frac{\sqrt{T}}{\gamma}\frac{\partial \rho}{\partial r} + \frac{\rho}{\gamma\sqrt{T}}\frac{\partial T}{\partial r}. \tag{D.16}$$

Appendix E

Linearization of the Equations in Axisymmetric Coordinates

The tables for the construction of the matrices for the inviscid terms of the linearized operator are given in this section.

	ρ'	V_r'	V_θ'	V_z'	T'
$\frac{\partial}{\partial r}$	V_r	ρ	0	0	0
$\frac{\partial}{\partial z}$	V_z	0	0	ρ	0
Base	$in\frac{V_\theta}{r}+\frac{\partial V_r}{\partial r}+\frac{V_r}{r}+\frac{\partial V_z}{\partial z}$	$\frac{\partial \rho}{\partial r}+\frac{\rho}{r}$	$in\frac{\rho}{r}$	$\frac{\partial \rho}{\partial z}$	0

Table E.1: Inviscid terms for the continuity equation.

The tables for the construction of the matrices for the viscous terms of the linearized operator are given in this section. **r-momentum equation**

	ρ'	V_r'	V_θ'	V_z'	T'
$\frac{\partial}{\partial r}$	$\frac{T}{\gamma\rho}$	V_r	0	0	$\frac{1}{\gamma}$
$\frac{\partial}{\partial z}$	0	V_z	0	0	0
Base	$-\frac{T}{\gamma\rho^2}\frac{\partial \rho}{\partial r}$	$in\frac{V_\theta}{r}+\frac{\partial V_r}{\partial r}$	$-2\frac{V_\theta}{r}$	$\frac{\partial V_r}{\partial z}$	$\frac{1}{\gamma\rho}\frac{\partial \rho}{\partial r}$

Table E.2: Inviscid terms for the r-momentum equation.

	ρ'	V_r'	V_θ'	V_z'	T'
$\frac{\partial}{\partial r}$	0	0	V_r	0	0
$\frac{\partial}{\partial z}$	0	0	V_z	0	0
Base	$in\frac{T}{\gamma\rho r}$	$\frac{\partial V_\theta}{\partial r}+\frac{V_\theta}{r}$	$in\frac{V_\theta}{r}+\frac{V_r}{r}$	$\frac{\partial V_\theta}{\partial z}$	$\frac{in}{\gamma r}$

Table E.3: Inviscid terms for the θ momentum equation.

	ρ'	V_r'	V_θ'	V_z'	T'
$\frac{\partial}{\partial r}$	0	0	0	V_r	0
$\frac{\partial}{\partial z}$	$\frac{T}{\gamma\rho}$	0	0	V_z	$\frac{1}{\gamma}$
Base	$-\frac{T}{\gamma\rho^2}\frac{\partial\rho}{\partial z}$	$\frac{\partial V_z}{\partial r}$	0	$in\frac{V_\theta}{r}+\frac{\partial V_z}{\partial z}$	$\frac{1}{\gamma\rho}\frac{\partial\rho}{\partial z}$

Table E.4: Inviscid terms for the z momentum equation.

	ρ'	V_r'	V_θ'	V_z'	T'
$\frac{\partial}{\partial r}$	0	$(\gamma-1)T$	0	0	V_r
$\frac{\partial}{\partial z}$	0	0	0	$(\gamma-1)T$	V_z
Base	0	$\frac{\partial T}{\partial r}+(\gamma-1)\frac{T}{r}$	$in(\gamma-1)\frac{T}{r}$	$\frac{\partial T}{\partial z}$	$in\frac{V_\theta}{r}+(\gamma-1)\left(\frac{\partial V_r}{\partial r}+\frac{V_r}{r}+\frac{\partial V_z}{\partial z}\right)$

Table E.5: Inviscid terms for the energy equation.

$$
\begin{aligned}
\text{Term1} &= \left(2+\frac{\lambda}{\mu}\right)\frac{\partial^2 V_r}{\partial r^2}+\left(2+\frac{\lambda}{\mu}\right)\frac{1}{r}\frac{\partial V_r}{\partial r}+\left(1+\frac{\lambda}{\mu}\right)\frac{1}{r}\frac{\partial^2 V_r}{\partial r\partial\theta}+\left(1+\frac{\lambda}{\mu}\right)\frac{\partial^2 V_z}{\partial z\partial r}+\frac{1}{r^2}\frac{\partial V_r^2}{\partial\theta^2} \\
&- \left(3+\frac{\lambda}{\mu}\right)\frac{1}{r^2}\frac{\partial V_\theta}{\partial\theta}+\frac{\partial^2 V_r}{\partial z^2}-\left(2+\frac{\lambda}{\mu}\right)\frac{V_r}{r^2} \\
\text{Term2} &= \left(2+\frac{\lambda}{\mu}\right)\frac{\partial V_r}{\partial r}+\frac{\lambda}{\mu}\frac{V_r}{r}+\frac{\lambda}{\mu}\frac{1}{r}\frac{\partial V_\theta}{\partial\theta}+\frac{\lambda}{\mu}\frac{\partial V_z}{\partial z} \\
\text{Term3} &= \frac{1}{r}\frac{\partial V_\theta}{\partial r}+\frac{1}{r^2}\frac{\partial V_r}{\partial\theta}-\frac{V_\theta}{r^2} \\
\text{Term4} &= \frac{\partial V_r}{\partial z}+\frac{\partial V_z}{\partial r}
\end{aligned}
$$

	ρ'	V_r'	V_θ'	V_z'	T'
$\frac{\partial}{\partial r}$	0	$(2\mu+\lambda)\frac{1}{r}+\frac{\partial\mu}{\partial r}\left(2+\frac{\lambda}{\mu}\right)$	$(\mu+\lambda)\frac{in}{r}$	$\frac{\partial\mu}{\partial z}$	$pT^{p-1}\times$ Term2
$\frac{\partial}{\partial z}$	0	$\frac{\partial\mu}{\partial z}$	0	$\frac{\lambda}{\mu}\frac{\partial\mu}{\partial r}$	$pT^{p-1}\times$ Term4
$\frac{\partial^2}{\partial r^2}$	0	$(2\mu+\lambda)$	0	0	0
$\frac{\partial^2}{\partial z^2}$	0	μ	0	0	0
$\frac{\partial^2}{\partial r\partial z}$	0	0	0	$(\mu+\lambda)$	0
Base	$-\frac{1}{\rho}\left[\mu\text{Term1}+\frac{\partial\mu}{\partial r}\text{Term2}+\frac{\partial\mu}{\partial z}\text{Term4}\right]$	$\mu\left[-\frac{n^2}{r^2}-\left(2+\frac{\lambda}{\mu}\right)\frac{1}{r^2}\right]+\frac{\partial\mu}{\partial r}\left[\frac{\lambda}{\mu}\frac{1}{r}\right]$	$-(3\mu+\lambda)\frac{1}{r^2}in+\frac{\partial\mu}{\partial r}\left[\frac{\lambda}{\mu}\frac{1}{r}in\right]$	0	$pT^{p-1}\times$ Term1 $+\frac{\partial}{\partial r}pT^{p-1}\times$ Term2 $+\frac{\partial}{\partial z}pT^{p-1}\times$ Term4

Table E.6: Viscous terms for the r-momentum equation.

θ-momentum equation

$$
\begin{aligned}
\text{Term1} &= \frac{\partial^2 V_\theta}{\partial r^2} + \left(1+\frac{\lambda}{\mu}\right)\frac{1}{r}\frac{\partial^2 V_\theta}{\partial\theta\partial r} + \left(2+\frac{\lambda}{\mu}\right)\frac{1}{r^2}\frac{\partial^2 V_\theta}{\partial\theta^2} + \left(3+\frac{\lambda}{\mu}\right)\frac{1}{r^2}\frac{\partial V_r}{\partial\theta} \\
&+ \left(1+\frac{\lambda}{\mu}\right)\frac{1}{r}\frac{\partial^2 V_z}{\partial\theta\partial z} + \frac{\partial^2 V_\theta}{\partial z^2} + \frac{1}{r}\frac{\partial V_\theta}{\partial r} - \frac{V_\theta}{r^2} \\
\text{Term2} &= \frac{\partial V_\theta}{\partial r} + \frac{1}{r}\frac{\partial V_r}{\partial\theta} - \frac{V_\theta}{r} \\
\text{Term3} &= \left(2+\frac{\lambda}{\mu}\right)\frac{1}{r^2}\frac{\partial V_\theta}{\partial\theta} + \frac{(2\mu+\lambda)}{\mu}\frac{V_r}{r^2} + \frac{\lambda}{\mu}\frac{1}{r}\frac{\partial V_r}{\partial r} + \frac{\lambda}{\mu}\frac{1}{r}\frac{\partial V_z}{\partial z} \\
\text{Term4} &= \frac{\partial V_\theta}{\partial z} + \frac{1}{r}\frac{\partial V_z}{\partial\theta}
\end{aligned}
$$

	ρ'	V_r'	V_θ'	V_z'	T'
$\frac{\partial}{\partial r}$	0	$(\mu+\lambda)\frac{in}{r}$	$\mu\frac{1}{r}+\frac{\partial\mu}{\partial r}$	0	$pT^{p-1}\times$ Term2
$\frac{\partial}{\partial z}$	0	0	$\frac{\partial\mu}{\partial z}$	$(\mu+\lambda)\frac{in}{r}$	$pT^{p-1}\times$ Term4
$\frac{\partial^2}{\partial r^2}$	0	0	μ	0	0
$\frac{\partial^2}{\partial z^2}$	0	0	μ	0	0
$\frac{\partial^2}{\partial r\partial z}$	0	0	0	0	0
Base	$-\frac{1}{\rho}\left[\mu\text{Term1}+\frac{\partial\mu}{\partial r}\text{Term2}+\frac{\partial\mu}{\partial z}\text{Term4}\right]$	$(3\mu+\lambda)\frac{1}{r^2}in+\frac{in}{r}\frac{\partial\mu}{\partial r}$	$\mu\left[-\left(2+\frac{\lambda}{\mu}\right)\frac{n^2}{r^2}-\frac{1}{r^2}\right]-\frac{1}{r}\frac{\partial\mu}{\partial r}$	$\frac{in}{r}\frac{\partial\mu}{\partial z}$	$pT^{p-1}\times\text{Term1}+\frac{\partial}{\partial r}pT^{p-1}\times\text{Term2}+\frac{\partial}{\partial z}pT^{p-1}\times\text{Term4}$

Table E.7: Viscous terms for the θ momentum equation.

z-momentum equation

$$
\begin{aligned}
\text{Term1} &= \frac{\partial^2 V_z}{\partial r^2} + \frac{1}{r^2}\frac{\partial^2}{\partial \theta^2} + \left(2 + \frac{\lambda}{\mu}\right)\frac{\partial^2 V_z}{\partial z^2} + \left(1 + \frac{\lambda}{\mu}\right)\frac{\partial^2 V_r}{\partial r \partial z} + \frac{1}{r}\frac{\partial V_z}{\partial r} \\
&+ \left(1 + \frac{\lambda}{\mu}\right)\frac{1}{r}\frac{\partial V_r}{\partial z} + \left(1 + \frac{\lambda}{\mu}\right)\frac{1}{r}\frac{\partial^2 V_\theta}{\partial \theta \partial z} \\
\text{Term2} &= \frac{\partial V_z}{\partial r} + \frac{\partial V_r}{\partial z} \\
\text{Term3} &= \frac{1}{r^2}\frac{\partial V_z}{\partial \theta} + \frac{1}{r}\frac{\partial V_\theta}{\partial z} \\
\text{Term4} &= \left(2 + \frac{\lambda}{\mu}\right)\frac{\partial V_z}{\partial z} + \frac{\lambda}{\mu}\frac{\partial V_r}{\partial r} + \frac{\lambda}{\mu}\frac{V_r}{r} + \frac{\lambda}{\mu}\frac{1}{r}\frac{\partial V_\theta}{\partial \theta}
\end{aligned}
$$

	ρ'	V_r'	V_θ'	V_z'	T'
$\frac{\partial}{\partial r}$	0	$\frac{\lambda}{\mu}\frac{\partial \mu}{\partial z}$	0	$\frac{\mu}{r}+\frac{\partial \mu}{\partial r}$	$pT^{p-1}\times$ Term2
$\frac{\partial}{\partial z}$	0	$(\mu+\lambda)\frac{1}{r}+\frac{\partial \mu}{\partial r}$	$(\mu+\lambda)\frac{in}{r}+\frac{\partial \mu}{\partial \theta}\frac{1}{r}$	$\left(2+\frac{\lambda}{\mu}\right)\frac{\partial \mu}{\partial z}$	$pT^{p-1}\times$ Term4
$\frac{\partial^2}{\partial r^2}$	0	0	0	μ	0
$\frac{\partial^2}{\partial z^2}$	0	0	0	$\left(2+\frac{\lambda}{\mu}\right)\mu$	0
$\frac{\partial^2}{\partial r \partial z}$	0	$(\mu+\lambda)$	0	0	0
Base	$-\frac{1}{\rho}\left[\mu\text{Term1}+\frac{\partial \mu}{\partial r}\text{Term2}+\frac{\partial \mu}{\partial z}\text{Term4}\right]$	$\frac{\lambda}{\mu}\frac{1}{r}\frac{\partial \mu}{\partial z}$	$\frac{\lambda}{\mu}\frac{in}{r}\frac{\partial \mu}{\partial z}$	$-\frac{n^2}{r^2}\mu$	$pT^{p-1}\times$ Term1 $+\frac{\partial}{\partial r}pT^{p-1}\times$ Term2 $+\frac{\partial}{\partial z}pT^{p-1}\times$ Term4

Table E.8: Viscous terms for the z momentum equation.

Energy equation

$$
\begin{aligned}
\text{Term1} &= \frac{\partial^2 T}{\partial r^2} + \frac{1}{r}\frac{\partial T}{\partial r} + \frac{1}{r^2}\frac{\partial^2 T}{\partial \theta^2} + \frac{\partial^2 T}{\partial z^2} \\
\text{Term2} &= (2\mu+\lambda)\frac{\partial V_r}{\partial r} + \lambda\frac{V_r}{r} + \lambda\frac{1}{r}\frac{\partial V_\theta}{\partial \theta} + \lambda\frac{\partial V_z}{\partial z} \\
\text{Term3} &= \frac{\partial V_r}{\partial \theta} + \frac{\partial V_\theta}{\partial r} - \frac{V_\theta}{r} \\
\text{Term4} &= \frac{\partial V_\theta}{\partial r} + \frac{1}{r}\frac{\partial V_r}{\partial \theta} - \frac{V_r}{r} \\
\text{Term5} &= \frac{1}{r}\frac{\partial V_\theta}{\partial \theta} + \frac{V_r}{r} \\
\text{Term6} &= (2\mu+\lambda)\frac{1}{r}\frac{\partial V_\theta}{\partial \theta} + (2\mu+\lambda)\frac{V_r}{r} + \lambda\frac{\partial V_r}{\partial r} + \lambda\frac{\partial V_z}{\partial z} \\
\text{Term7} &= \frac{\partial V_\theta}{\partial z} + \frac{1}{r}\frac{\partial V_z}{\partial \theta} \\
\text{Term8} &= \frac{\partial V_\theta}{\partial z} + \frac{1}{r}\frac{\partial V_z}{\partial \theta} \\
\text{Term9} &= (2\mu+\lambda)\frac{\partial V_z}{\partial z} + \lambda\frac{\partial V_r}{\partial r} + \lambda\frac{V_r}{r} + \lambda\frac{1}{r}\frac{\partial V_\theta}{\partial \theta} \\
\text{Term10} &= \frac{\partial V_r}{\partial z} + \frac{\partial V_z}{\partial r} \\
\text{Term11} &= \frac{\partial V_z}{\partial r} + \frac{\partial V_r}{\partial z}
\end{aligned}
$$

	ρ'	V_r'	V_θ'	V_z'	T'
$\frac{\partial}{\partial r}$	0	$F_2\mu\left[\left(2+\frac{\lambda}{\mu}\right)\frac{\partial V_r}{\partial r}+\text{Term2}+\frac{\lambda}{\mu}\text{Term5}+\frac{\lambda}{\mu}\frac{\partial V_z}{\partial z}\right]$	$F_2\mu[\text{Term3}+\text{Term4}]$	$F_2\mu[\text{Term10}+\text{Term11}]$	$F_1\left[\frac{\partial \kappa}{\partial r}+pT^{p-1}\frac{\partial T}{\partial r}+\frac{\kappa}{r}\right]$
$\frac{\partial}{\partial z}$	0	$F_2\mu[\text{Term10}+\text{Term11}]$	$F_2\mu[\text{Term7}+\text{Term8}]$	$F_2\mu\left[\frac{\lambda}{\mu}\frac{\partial V_r}{\partial r}+\frac{\lambda}{\mu}\text{Term5}+\left(2+\frac{\lambda}{\mu}\right)\frac{\partial V_z}{\partial z}+\text{Term9}\right]$	$F_1\left[\frac{\partial \kappa}{\partial z}+pT^{p-1}\frac{\partial T}{\partial z}\right]$
$\frac{\partial^2}{\partial r^2}$	0	0	0	0	$F_1\kappa$
$\frac{\partial^2}{\partial z^2}$	0	0	0	0	$F_1\kappa$
$\frac{\partial^2}{\partial r \partial z}$	0	0	0	0	0
Base	$-\frac{F_1}{\rho}\left[\dots\right]$ $-\frac{F_2\mu}{\rho}\left[\dots\right]$	$F_2\mu\left[\frac{\lambda}{\mu}\frac{1}{r}+\text{Term3}\left(\frac{in}{r}-\frac{1}{r}\right)in\text{Term4}+\left(2+\frac{\lambda}{\mu}\right)\frac{1}{r}\text{Term5}\text{Term6}\frac{1}{r}+\frac{\lambda}{\mu}\frac{1}{r}\frac{\partial V_z}{\partial z}\right.$	$F_2\mu\left(\frac{\lambda}{\mu}\frac{in}{r}-\frac{1}{r}\text{Term4}-\frac{1}{r}\text{Term4}+\left(2+\frac{\lambda}{\mu}\right)\frac{in}{r}\text{Term5}\text{Term6}\frac{1}{r}+\frac{\lambda}{\mu}\frac{1}{r}\frac{\partial V_z}{\partial z}\right.$	$F_2\mu\left[\frac{in}{r}\text{Term7}+\frac{in}{r}\text{Term8}\right]$	$F_1\left[pT^{p-1}\times\text{Term1}-\frac{n^2}{r^2}\kappa\frac{\partial pT^{p-1}}{\partial r}\frac{\partial T}{\partial r}+\frac{\partial pT^{p-1}}{\partial z}\frac{\partial T}{\partial z}+F_2\left[\dots\right]\times pT^{p-1}\right.$

Table E.9: Viscous terms for the energy momentum equation. $F_1=\frac{\gamma}{Pr}$ and $F_2=\gamma(\gamma-1)$.

Appendix F

Shock Capturing Scheme for Axisymmetric Configurations

Supersonic jets have a shock cell pattern in the core flow. To appropriately capture the shock cell formation, a shock capturing scheme is implemented. The artificial transport coefficients are computed using the method described in Kawai and Lele (Kawai *et al.*, 2010). The idea behind shock capturing schemes is to enhance the dissipation to smoothen out the high gradient shock regions. A metric based on the grid and the strain-rate tensor identifies the shocks and is used to compute the localized artificial transport coefficients μ^*, κ^*, β^*, which are updated as

$$\begin{aligned} \mu' &= \mu + \mu^* \\ \beta' &= \beta + \beta^* \\ \kappa' &= \kappa + \kappa^*. \end{aligned}$$

where

$$\begin{aligned} \mu^* &= C_\mu \rho \overline{\left| \left(\frac{\partial \xi}{\partial z}\right)^4 \frac{\partial^4 S}{\partial \xi^4} \Delta z^6 + \left(\frac{\partial \eta}{\partial r}\right)^4 \frac{\partial^4 S}{\partial \eta^4} \Delta r^6 \right|} \times Re \\ \beta^* &= C_\beta \rho f_{sw} \overline{\left| \left(\frac{\partial \xi}{\partial z}\right)^4 \frac{\partial^4 S}{\partial \xi^4} \Delta z^6 + \left(\frac{\partial \eta}{\partial r}\right)^4 \frac{\partial^4 S}{\partial \eta^4} \Delta r^6 \right|} \times Re \\ \kappa^* &= C_\kappa \frac{\rho}{\gamma c} \overline{\left| \left(\frac{\partial \xi}{\partial z}\right)^4 \frac{\partial^4 T}{\partial \xi^4} \Delta z^6 + \left(\frac{\partial \eta}{\partial r}\right)^4 \frac{\partial^4 T}{\partial \eta^4} \Delta r^6 \right|} \times RePr \\ f_{sw} &= H(-\nabla \cdot u) \times \frac{(\nabla \cdot u)^2}{(\nabla \cdot u)^2 + (\nabla \times u)^2 + \epsilon} \end{aligned}$$

where H is the Heaviside function, S is the magnitude of the strain-rate tensor and $\overline{(\cdot)}$ denotes a Gaussian filtering operation. The coefficients are $C_\mu = 0.002$, $C_\beta = 1.75$, $C_\kappa = 0.01$.

$$\mathbf{S} = \begin{bmatrix} S_{11} & S_{12} & S_{13} \\ S_{21} & S_{22} & S_{23} \\ S_{31} & S_{32} & S_{33} \end{bmatrix}$$

$$\begin{aligned} S_{11} &= \frac{\partial V_r}{\partial r} - \frac{1}{3}\nabla \cdot u \\ S_{13} &= S_{31} = \frac{1}{2}(\frac{\partial V_r}{\partial z} + \frac{\partial V_z}{\partial r}) \\ S_{33} &= \frac{\partial V_z}{\partial z} - \frac{1}{3}\nabla \cdot u \\ S_{12} &= S_{21} = S_{23} = S_{32} = S_{33} = 0 \end{aligned}$$

and the magnitude of the strain-rate tensor is defined by

$$S = ||\mathbf{S}|| = \sum_{i,j=1}^{3} S_{ij}^2$$

A nine-point truncated-Gaussian filter is implemented for the filtering operation. The filter is of the form

$$\begin{aligned} \text{Central} \quad &: \quad \bar{f}_0 = \sum_{i=-4}^{4} C_i f_i \\ \text{Boundary} \quad &: \quad \bar{f}_k = \sum_{i=1}^{11} B_{ki} f_i \end{aligned}$$

$$
\begin{aligned}
C_{-4,4} &= 107/103680, \quad C_{-3,3} = 149/12960, \quad C_{-2,2} = 1997/25920, \quad C_{-1,1} = 3091/12960, \\
C_0 &= 3565/10368. \\
B_{21} &= 0.085777408970000, \quad B_{22} = 0.722371828476000, \quad B_{23} = 0.356848072173000, \\
B_{24} &= -0.223119093072000, \quad B_{25} = 0.057347064865000, \quad B_{26} = 0.000747264596000, \\
B_{27} &= 0.000027453993000. \\
B_{31} &= -0.032649010764000, \quad B_{32} = 0.143339502575000, \quad B_{33} = 0.726678822020000, \\
B_{34} &= 0.294622121167000, \quad B_{35} = -0.186711738069000, \quad B_{36} = 0.062038376258000, \\
B_{37} &= -0.007318073189000. \\
B_{41} &= 0.000054596010000, \quad B_{42} = -0.042124772446000, \quad B_{43} = 0.173103107841000, \\
B_{44} &= 0.700384128648000, \quad B_{45} = 0.276543612935000, \quad B_{46} = -0.131223506571000, \\
B_{47} &= 0.023424966418000, \quad B_{48} = -0.013937561779000 \quad B_{49} = 0.024565095706000 \\
B_{410} &= -0.013098287852000, \quad B_{411} = 0.002308621090000.
\end{aligned}
$$

Appendix G

Proper Orthogonal Decomposition

Suppose that we have an ensemble $\{u^k\}$ of real scalar fields, each being a function of $u = u(z, r)$ defined on the domain $0 \leq x \leq 1$. We want to find a basis $\{\phi(z, r)\}_{j=1}^{\infty} \epsilon\, L^2$ that is optimal for the data set in the sense that finite dimensional representations of the form

$$u_N(z, r) = \sum_{j=1}^{N} a_j \phi_j(z, r) \tag{G.1}$$

describe typical members of the ensemble better than representations of the same dimension in any other basis Holmes *et al.* (1998). The mathematical statement of optimality is that we should choose ϕ to maximize the averaged projection of u onto ϕ suitably normalized.

$$\max_{\phi \epsilon L^2([0,1])} \frac{\langle |(u, \phi)|^2 \rangle}{||\phi||^2} \tag{G.2}$$

where

$$(u, \phi) = \int_{\Omega_x} u(z, r)\phi(z, r) r dr dz$$

and $|\cdot|$ denotes the modulus and $||\cdot||$ is the L^2-norm :

$$||f|| = (f, f)^{\frac{1}{2}}$$

G.1 The Formulation

The corresponding cost functional for the problem is

$$J[\phi] = \langle |(u, \phi^2)| \rangle - \lambda(||\phi||^2 - 1) \tag{G.3}$$

and a necessary condition for the extrema is that the functional derivative vanish for all variations $\phi + \delta\psi \in L^2([0,1])$, $\delta \in \mathrm{R}$:

$$\frac{d}{d\delta} J[\phi + \delta\phi]|_{\delta=0} = 0 \tag{G.4}$$

$$\begin{aligned}
\frac{d}{d\delta} J[\phi + \delta\phi]|_{\delta=0} &= \frac{d}{d\delta}[\langle (u, \phi + \delta\psi)(\phi + \delta\psi, u)\rangle - \lambda(\phi + \delta\psi, \phi + \delta\psi)]|_{\delta=0} \\
&= \Big[\langle \frac{d}{d\delta}(u, \phi + \delta\psi)(\phi + \delta\psi, u) + (u, \phi + \delta\psi)\frac{d}{d\delta}(\phi + \delta\psi, u)\rangle\Big]|_{\delta=0} \\
&- \lambda\Big[\Big(\frac{d}{d\delta}(\phi + \delta\psi), (\phi + \delta\psi)\Big) + \Big((\phi + \delta\psi), \frac{d}{d\delta}(\phi + \delta\psi)\Big)\Big]|_{\delta=0} \\
&= \Big[\langle (u, \psi)(\phi + \delta\psi, u) + (u, \phi + \delta\psi)(\psi, u)\rangle\Big]|_{\delta=0} \\
&- \lambda\Big[(\psi, \phi + \delta\psi) + (\phi + \delta\psi), \psi)\Big]|_{\delta=0} \\
&= \Big[\langle (u, \psi)(\phi, u) + (u, \phi)(\psi, u)\rangle\Big] - \lambda\Big[(\psi, \phi) + (\phi, \psi)\Big] \\
&= 2\Big[\langle (u, \psi)(\phi, u)\rangle - \lambda(\phi, \psi)\Big] = 0
\end{aligned} \tag{G.5}$$

The above quantity can be written as

$$\begin{aligned}
\langle \int_0^1 u(z,r)\psi(z,r)rdrdz \int_0^1 \phi(z^{'}, r^{'})u(z^{'}, r^{'})rdrdz^{'}\rangle - \lambda \int_0^1 \phi(z,r)\psi(z,r)rdrdz \quad = \\
\int_0^1 \Big[\int_0^1 \langle u(z,r)u(z^{'}, r^{'})\rangle \phi(z^{'}, r^{'})rdrdz^{'} - \lambda\phi(z,r)\Big]\psi(z,r)rdrdz = 0
\end{aligned} \tag{G.6}$$

Since ψ is an arbitrary variation, the above condition reduces to

$$\int_0^1 \langle u(z,r)u(z^{'}, r^{'})\rangle \phi(z^{'}, r^{'})rdrdz^{'} = \lambda\phi(z,r) \tag{G.7}$$

Thus the optimal basis is given by the eigenfunctions of the $\{\phi_j\}$ of the integral equation (7) whose kernel is the averaged autocorrelation function $R(z, r, z^{'}, r^{'}) \equiv \langle u(z,r)u(z^{'}, r^{'})\rangle$. They are called empirical eigenfuctions. The Hilbert-Schmidt theory shows that the eigenfunctions form a complete orthogognal set and the reconstruction of the field is given by

$$u \approx u_N = \sum_{k=1}^{N} a_k \phi^{(k)}(z,r)$$

Multiplying both sides by $\phi^{(k)}(z,r)$, integrating over the domain and using the fact that the $\phi^{(k)}$s are

mutually orthogonal, we obtain

$$a_k = (\phi^{(k)}, u)$$

The coefficients are uncorrelated and their mean square values are the eigenvalues themselves

$$\langle a^{(n)} a^{(m)} \rangle = \delta_{nm} \lambda^{(n)}$$

Hence the eigenvalues are all non-negative. The turbulent kinetic energy is the sum of the n eigenvalues.

$$E = \int \langle u_i u_i \rangle r dr dz = \sum_{n=1}^{\infty} \lambda^{(n)}$$

The above equation gives us the idea that the eigenmode corresponding to the largest eigenvalue will contribute the maximum to the total energy and that the contributions of the eigenmodes decrease with the corresponding decrease in the eigenvalue.

G.2 The Method of Snapshots

The method of snapshots (Sirovich (1991), Smith *et al.* (2005)) formulates the computation of POD modes as an $N_T \times N_T$ eigenvalue problem, where N_T is the total number of snapshots in the ensemble. The formulation is described for scalar functions $u_{(k)}$. Equation (7) can be written as

$$\frac{1}{N_T} \sum_{k=0}^{N_T} u_{(k)}(z,r) \int_{\Omega_x} u_{(k)}(z,r) u(z^{'}, r^{'}) \phi(z^{'}, r^{'}) r dr dz^{'} = \lambda \phi(z,r) \tag{G.8}$$

Define

$$c_j = \int_{\Omega_x} u_{(j)}(z^{'}, r^{'}) \phi(z^{'}, r^{'}) r dr dz^{'}$$

Then equation (8) can be written as

$$\frac{1}{N_T} \sum_{k=1}^{N_T} c_j u_{(j)}(z,r) = \lambda \phi(z,r) \tag{G.9}$$

ie. the eigenfunctions are expressed as linear combinations of the observations or snapshots. Multiplying both sides by $u_{(i)}$ and integrating yields

$$\frac{1}{N_T}\sum_{j=1}^{N_T} c_j \int_{\Omega_x} u_{(i)}(z,r)u_{(j)}(z,r)rdrdz = \lambda \int_{\Omega_x} u_{(i)}(z,r)\phi(z,r)rdrdz \tag{G.10}$$

Defining

$$a_{ij} = \int_{\Omega_x} u_{(i)}(z,r)u_{(j)}(z,r)rdrdz$$

equation (10) can be written in matrix form as

$$\begin{bmatrix} a_{11} & \dots & a_{1N_T} \\ \vdots & & \vdots \\ a_{N_T1} & \dots & a_{N_TN_T} \end{bmatrix} \begin{bmatrix} c_1 \\ \vdots \\ c_{N_T} \end{bmatrix} = \lambda \begin{bmatrix} c_1 \\ \vdots \\ c_{N_T} \end{bmatrix} \tag{G.11}$$

The eigenvectors of the above $N_T \times N_T$ matrix eigenvalue problem are denoted by $c^n = [c_1^n \dots c_{N_T}^n]^T$ and the eigenvalues by λ^n. From (9), it can be seen that the n^{th} eigenfunction of the original problem can be reconstructed from the coefficients c_j^n via

$$\phi^{(n)}(z,r) = \frac{1}{\lambda^{(n)}N_T}\sum_{j=1}^{N_T} c_j^n u_{(j)}(z,r) \tag{G.12}$$

or in matrix form,

$$\phi^{(n)}(z,r) = \frac{1}{\lambda^{(n)}N_T}[c_1^n \dots c_{N_T}^n] \begin{bmatrix} u_{(1)}(z,r) \\ \vdots \\ u_{N_T}(z,r) \end{bmatrix} \tag{G.13}$$

Fig. G.1 shows the reconstruction of the solution using 10, 25, 50 and 220 (all) modes for the pressure perturbation at a given radial location for the uncontrolled axisymmetric jet.

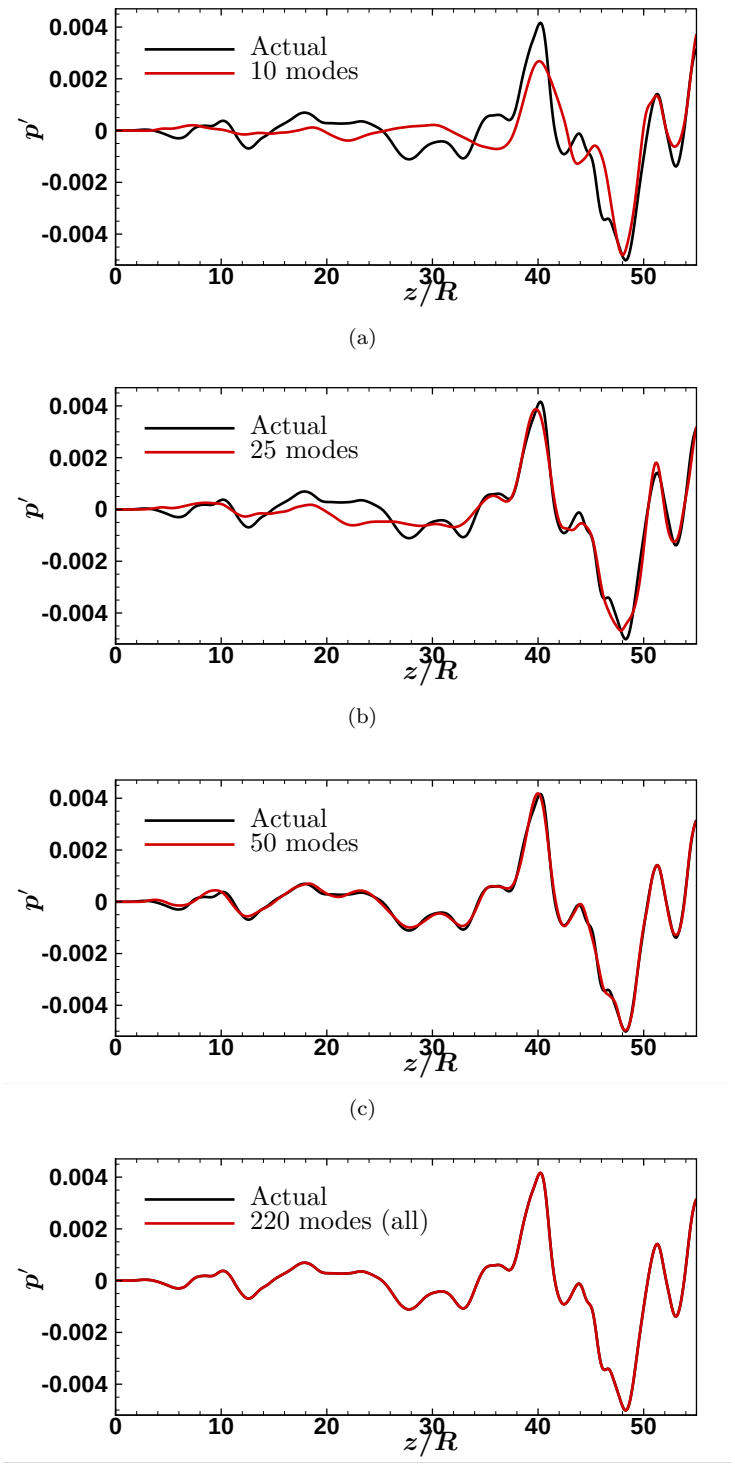

Figure G.1: Reconstruction of far-field pressure using POD modes (a) 10 modes (b) 25 modes (c) 50 modes (d) 220 modes (all).

References

Åkervik, E., Brandt, L., Henningson, D., Hœpffner, J., Marxen, O. & Schlatter, P. 2006 Steady solutions of the Navier–Stokes equations by selective frequency damping. *Physics of Fluids* **18**, 068102.

Amestoy, P., Duff, I., LExcellent, J. & Koster, J. 2001 Mumps: a general purpose distributed memory sparse solver. *Applied Parallel Computing. New Paradigms for HPC in Industry and Academia* pp. 121–130.

Amitay, M., Pitt, D. & Glezer, A. 2002 Separation control in duct flows. *Journal of Aircraft* **39** (4), 616–620.

Bagheri, S., Schlatter, P., Schmid, P. J. & Henningson, D. S. 2009 Global stability of a jet in crossflow. *Journal of Fluid Mechanics* **624** (9), 33–44.

Balakumar, P. 1998 Prediction of supersonic jet noise. In *36th AIAA Aerospace Sciences Meeting and Exhibit, AIAA Paper 98-1057*.

Balay, S., Brown, J., Buschelman, K., Eijkhout, V., Gropp, W. D., Kaushik, D., Knepley, M. G., McInnes, L. C., Smith, B. F. & Zhang, H. 2012*a* PETSc users manual. *Tech. Rep.* ANL-95/11 - Revision 3.3. Argonne National Laboratory.

Balay, S., Brown, J., Buschelman, K., Gropp, W. D., Kaushik, D., Knepley, M. G., McInnes, L. C., Smith, B. F. & Zhang, H. 2012*b* PETSc Web page. Http://www.mcs.anl.gov/petsc.

Balay, S., Gropp, W. D., McInnes, L. C. & Smith, B. F. 1997 Efficient management of parallelism in object oriented numerical software libraries. In *Modern Software Tools in Scientific Computing* (ed. E. Arge, A. M. Bruaset & H. P. Langtangen), pp. 163–202. Birkhäuser Press.

Bodony, D. 2010 Accuracy of the simultaneous-approximation-term boundary condition for time-dependent problems. *Journal of Scientific Computing* **43** (1), 118–133.

Bodony, D. J. 2005 Aeroacoustic prediction of turbulent free shear flows. PhD thesis, Stanford University.

Bodony, D. J. 2006 Analysis of sponge zones for computational fluid mechanics. *Journal of Computational Physics* **212**, 681–702.

Bodony, D. J. & Lele, S. K. 2005 On using large-eddy simulation for the prediction of noise from cold and heated turbulent jets. *Physics of Fluids (1994-present)* **17** (8), 085103.

Bodony, D. J. & Lele, S. K. 2008 Current status of jet noise predictions using large-eddy simulation. *AIAA Journal* **46** (2), 364–380.

Bowes, W., Rumpf, D., Bowler, D., Carnes, R. & Fratarangelo, P. 2009 Report on jet engine noise reduction. *URL: http://www. nrac. navy. mil/docs/2009_FINAL_Jet_Noise_Report_4-26-09. pdf* .

Brès, G. A. & Colonius, T. 2008 Three-dimensional instabilities in compressible flow over open cavities. *Journal of Fluid Mechanics* **599** (1), 309–339.

Briggs, R. 1964 Electron-stream interaction with plasma. Res. Monogr. no. 29. *MIT Press Cambridge, Mass* **24**, 88.

Brown, G. L., Roshko, A. *et al.* 1974 On density effects and large structure in turbulent mixing layers. *Journal of Fluid Mechanics* **64** (4), 775–816.

Cavalieri, A. V., Jordan, P., Agarwal, A. & Gervais, Y. 2011 Jittering wave-packet models for subsonic jet noise. *Journal of Sound and Vibration* **330** (18), 4474–4492.

Cavalieri, A. V., Rodríguez, D., Jordan, P., Colonius, T. & Gervais, Y. 2013 Wavepackets in the velocity field of turbulent jets. *Journal of Fluid Mechanics* **730**, 559–592.

Chandler, G. J., Juniper, M. P., Nichols, J. W. & Schmid, P. J. 2012 Adjoint algorithms for the Navier–Stokes equations in the low Mach number limit. *Journal of Computational Physics* **231** (4), 1900–1916.

Chen, K. K. & Rowley, C. W. 2011 h_2 optimal actuator and sensor placement in the linearised complex ginzburg-landau system. *Journal of Fluid Mechanics* **681**, 241–260.

Cheung, L. C., Bodony, D. J. & Lele, S. K. 2007 Noise radiation predictions from jet instability waves using a hybrid nonlinear PSE-acoustic analogy approach. In *Proceedings of the 13th AIAA/CEAS Aeroacoustics Conference (28th AIAA Aeroacoustics Conference)*.

Cheung, L. C. & Lele, S. K. 2009 The dynamics of nonlinear instability waves in laminar heated and unheated compressible mixing layers. *Physics of Fluids (1994-present)* **21** (9), 094103.

Chomaz, J. 2005 Global instabilities in spatially developing flows: non-normality and nonlinearity. *Annual Review of Fluid Mechanics* **37**, 357–392.

Chomaz, J., Huerre, P. & Redekopp, L. 1988 Bifurcations to local and global modes in spatially developing flows. *Physical Review Letters* **60** (1), 25–28.

Cohen, J. & Wygnanski, I. 1987 The evolution of instabilities in the axisymmetric jet. part 1. the linear growth of disturbances near the nozzle. *Journal of Fluid Mechanics* **176**, 191–219.

Colonius, T. 2004 Modeling artificial boundary conditions for compressible flow. *Annual Review of Fluid Mechanics* **36**, 315–345.

Crighton, D. & Gaster, M. 1976 Stability of slowly diverging jet flow. *Journal of Fluid Mechanics* **77** (2), 397–413.

Crow, S. C. & Champagne, F. 1971 Orderly structure in jet turbulence. *Journal of Fluid Mechanics* **48** (3), 547–591.

Eriksson, L. E. & Rizzi, A. 1985 Computer-aided analysis of the convergence to steady state of discrete approximations to the Euler equations. *Journal of Computational Physics* **57** (1), 90–128.

Freund, J. 1997 Proposed inflow/outflow boundary condition for direct computation of aerodynamic sound. *AIAA Journal* **35** (4), 740–742.

Freund, J., Lele, S. & Moin, P. 2000 Numerical simulation of a Mach 1.92 turbulent jet and its sound field. *AIAA Journal* **38** (11), 2023–2031.

Freund, J. B. 2001 Noise sources in a low-Reynolds-number turbulent jet at Mach 0.9. *Journal of Fluid Mechanics* **438**, 277–305.

Giannetti, F., Camarri, S. & Luchini, P. 2010 Structural sensitivity of the secondary instability in the wake of a circular cylinder. *Journal of Fluid Mechanics* **651** (1), 319–337.

Giannetti, F. & Luchini, P. 2007 Structural sensitivity of the first instability of the cylinder wake. *Journal of Fluid Mechanics* **581** (1), 167–197.

Goldstein, M. E. & Leib, S. 2005 The role of instability waves in predicting jet noise. *Journal of Fluid Mechanics* **525**, 37–72.

Greenough, J., Riley, J., Soestrisno, M. & Eberhardt, D. 1989 The effects of walls on a compressible mixing layer. *Rep./AIAA; N89-0372* .

Gudmundsson, K. & Colonius, T. 2009 Parabolized stability equation models for turbulent jets and their radiated sound. *AIAA paper* **3380**.

Han, S.-P. 1977 A globally convergent method for nonlinear programming. *Journal of Optimization Theory and Applications* **22** (3), 297–309.

Henningson, D. & Åkervik, E. 2008 The use of global modes to understand transition and perform flow control. *Physics of Fluids* **20**, 031302.

Hernandez, V., Roman, J., Tomas, A. & Vidal, V. 2007 Krylov-Schur methods in slepc. *Universitat Politecnica de Valencia, Technical Report STR-7* .

Hernandez, V., Roman, J. E. & Vidal, V. 2005 SLEPc: A scalable and flexible toolkit for the solution of eigenvalue problems. *ACM Transactions on Mathematical Software* **31** (3), 351–362.

Hicken, J. E. & Zingg, D. W. 2011 The role of dual consistency in functional accuracy: Error estimation and superconvergence. In *20th AIAA Computational Fluid Dynamics Conference, Honolulu, Hawaii, United States*.

Hill, D. C. 1992 A theoretical approach for analyzing the restabilization of wakes. In *AIAA Materials Specialist Conference-Coating Technology for Aerospace Systems*, , vol. 1.

Holmes, P., Lumley, J. L. & Berkooz, G. 1998 *Turbulence, coherent structures, dynamical systems and symmetry*. Cambridge university press.

Homsy, G. 1973 Global stability of time-dependent flows: impulsively heated or cooled fluid layers. *Journal of Fluid Mechanics* **60** (1), 129–139.

Huerre, P. & Monkewitz, P. A. 1990 Local and global instabilities in spatially developing flows. *Annual Review of Fluid Mechanics* **22** (1), 473–537.

Jackson, C. 1987 A finite-element study of the onset of vortex shedding in flow past variously shaped bodies. *Journal of Fluid Mechanics* **182** (1), 23–45.

Jordan, P. & Colonius, T. 2013 Wavepackets and turbulent jet noise. *Annual Review of Fluid Mechanics* **45**, 173–195.

Joseph, D. D. 1966 Nonlinear stability of the boussinesq equations by the method of energy. *Archive for Rational Mechanics and Analysis* **22** (3), 163–184.

Kawai, S., Shankar, S. K. & Lele, S. K. 2010 Assessment of localized artificial diffusivity scheme for large-eddy simulation of compressible turbulent flows. *Journal of Computational Physics* **229** (5), 1739–1762.

Kim, J., Bodony, D. J. & Freund, J. B. 2014 Adjoint-based control of loud events in a turbulent jet. *Journal of Fluid Mechanics* **741**, 28–59.

Kwong, A. H. & Dowling, A. P. 1994 Active boundary-layer control in diffusers. *AIAA journal* **32** (12), 2409–2414.

Laufer, J. & Yen, T.-C. 1983 Noise generation by a low-Mach-number jet. *Journal of Fluid Mechanics* **134**, 1–31.

Lehoucq, R., Sorensen, D. & Yang, C. 1997 ARPACK users' guide: Solution of large scale eigenvalue problems with implicitly restarted arnoldi methods. *Software Environ Tools* **6**.

Lewis, H. R. & Bellan, P. M. 1990 Physical constraints on the coefficients of fourier expansions in cylindrical coordinates. *Journal of Mathematical Physics* **31** (11), 2592–2596.

Lighthill, M. J. 1952 On sound generated aerodynamically. i. general theory. In *Proceedings of the Royal Society of London A: Mathematical, Physical and Engineering Sciences*, , vol. 211, pp. 564–587. The Royal Society.

Malik, M. 1990 Numerical methods for hypersonic boundary layer stability. *Journal of Computational Physics* **86** (2), 376–413.

Malik, M. & Chang, C.-L. 2000 Nonparallel and nonlinear stability of supersonic jet flow. *Computers & fluids* **29** (3), 327–365.

Marquet, O., Sipp, D. & Jacquin, L. 2008 Sensitivity analysis and passive control of cylinder flow. *Journal of Fluid Mechanics* **615**, 221.

Mattsson, K., Svärd, M. & Shoeybi, M. 2008 Stable and accurate schemes for the compressible Navier–Stokes equations. *Journal of Computational Physics* **227** (4), 2293–2316.

McLaughlin, D. K., Morrison, G. L. & Troutt, T. R. 1975 Experiments on the instability waves in a supersonic jet and their acoustic radiation. *Journal of Fluid Mechanics* **69** (1), 73–95.

Meliga, P. & Chomaz, J.-M. 2011 Global modes in a confined impinging jet: application to heat transfer and control. *Theoretical and Computational Fluid Dynamics* **25** (1-4), 179–193.

Meliga, P., Sipp, D. & Chomaz, J.-M. 2010 Open-loop control of compressible afterbody flows using adjoint methods. *Physics of Fluids* **22**, 054109.

Michalke, A. 1984 Survey on jet instability theory. *Prog. in Aero. Sci.* **21**, 159–199.

Moin, P., Squires, K., Cabot, W. & Lee, S. 1991 A dynamic subgrid-scale model for compressible turbulence and scalar transport. *Physics of Fluids A: Fluid Dynamics (1989-1993)* **3** (11), 2746–2757.

Moore, C. 1977 The role of shear-layer instability waves in jet exhaust noise. *Journal of Fluid Mechanics* **80** (2), 321–367.

Morrison, G. & McLaughlin, D. 1979 Noise generation by instabilities in low Reynolds number supersonic jets. *Journal of Sound and Vibration* **65** (2), 177–191.

Morrison, G. L. & McLaughlin, D. 1980 Instability process in low reynolds number supersonic jets. *AIAA Journal* **18** (7), 793–800.

Narayanan, S. & Banaszuk, A. 2003 Experimental study of a novel active separation control approach. *AIAA paper* **60**.

Nichols, J., Lele, S. & Moin, P. 2009 Global mode decomposition of supersonic jet noise. *Center for Turbulence Research Annual Research Briefs* .

Nichols, J. W. & Lele, S. K. 2011 Global modes and transient response of a cold supersonic jet. *Journal of Fluid Mechanics* **669**, 225–241.

Nicoll, W. B. & Ramaprian, B. 1970 Performance of conical diffusers with annular injection at inlet. *Journal of Basic Engineering* **92**, 827.

Nishi, M., Yoshida, K. & Morimitsu, K. 1998 Control of separation in a conical diffuser by vortex generator jets. *JSME International Journal, Series B, Fluids and Thermal Engineering* **41** (1), 233–238.

Oertel, H. 1979 Mach wave radiation of hot supersonic jets investigated by means of the shock tube and new optical techniques. In *Proc. 12th Int. Symp. on shock tubes and waves. Jerusalem*. DTIC Document.

Panickar, P. & Raman, G. 2009 Using linear stability analysis as a tool to evaluate jet and cavity flow control situations. *International Journal of Flow Control* **1** (1), 43–72.

Pierrehumbert, R. 1986 Universal short-wave instability of two-dimensional eddies in an inviscid fluid. *Physical Review Letters* **57**, 2157–2159.

Pierrehumbert, R. & Widnall, S. 1982 The two- and three-dimensional instabilities of a spatially periodic shear layer. *Journal of Fluid Mechanics* **114**, 59–82.

Piot, E., Casalis, G., Muller, F. & Bailly, C. 2006 Investigation of the PSE approach for subsonic and supersonic hot jets. Detailed comparisons with LES and linearized Euler equations results. *International Journal of Aeroacoustics* **5** (4), 361–393.

Pulliam, T. H. & Chaussee, D. 1981 A diagonal form of an implicit approximate-factorization algorithm. *Journal of Computational Physics* **39** (2), 347–363.

Qadri, U. A., Mistry, D. & Juniper, M. P. 2013 Structural sensitivity of spiral vortex breakdown. *Journal of Fluid Mechanics* **720**, 558–581.

Ragab, S. & Wu, J. 1989 Linear instabilities in two-dimensional compressible mixing layers. *Physics of Fluids A: Fluid Dynamics* **1**, 957.

Rao, D. 1971 A method of flow stabilisation with high pressure recovery in short, conical diffusers. *The Aeronautical Journal* **75**, 336–339.

Reddy, B. & Voyé, H. 1988 Finite element analysis of the stability of fluid motions. *Journal of Computational Physics* **79** (1), 92–112.

Reneau, L. R., Johnston, J. & Kline, S. J. 1967 Performance and design of straight, two-dimensional diffusers. *Journal of Basic Engineering* **89**, 141.

Rodríguez Álvarez, D. & Theofilis, V. 2010 Structural changes of laminar separation bubbles induced by global linear instability. *Journal of Fluid Mechanics* **655**, 280–305.

Salgado, A. M. & Sandham, N. D. 2007 Viscous instability of a compressible round jet. *Tech. Rep.* ISVR Report No. AFM-07/1. Southampton University.

Samanta, A. & Freund, J. B. 2008 Finite-wavelength scattering of incident vorticity and acoustic waves at a shrouded-jet exit. *Journal of Fluid Mechanics* **612**, 407–438.

Samanta, A. & Freund, J. B. 2015 A model supersonic buried-nozzle jet: instability and acoustic wave scattering and the far-field sound. *Journal of Fluid Mechanics* **778**.

Samimy, M., Kim, J., Kastner, J., Adamovich, I. & Utkin, Y. 2007 Active control of high-speed and high-reynolds-number jets using plasma actuators. *Journal of Fluid Mechanics* **578** (1), 305–30.

Samimy, M., Zaman, K. & Reeder, M. 1993 Effect of tabs on the flow and noise field of an axisymmetric jet. *AIAA Journal* **31** (4), 609–619.

Sandham, N. 1989 A numerical investigation of the compressible mixing layer. PhD thesis, Stanford University.

Schmid, P. J. & Henningson, D. S. 2000 *Stability and transition in shear flows*. Springer-Verlag, Berlin.

Schmidt, O., Towne, A., Colonius, T., Jordan, P., Jaunet, V., Cavalieri, A. V. & Brès, G. A. 2016 Super-and multi-directive acoustic radiation by linear global modes of a turbulent jet. In *22nd AIAA/CEAS Aeroacoustics Conference*, p. 2808.

Seifert, A., Darabi, A. & Wyganski, I. 1996 Delay of airfoil stall by periodic excitation. *Journal of Aircraft* **33** (4), 691–698.

Sinha, A., Rodríguez, D., Brès, G. A. & Colonius, T. 2014 Wavepacket models for supersonic jet noise. *Journal of Fluid Mechanics* **742**, 71–95.

Sipp, D., Marquet, O., Meliga, P. & Barbagallo, A. 2010 Dynamics and control of global instabilities in open-flows: a linearized approach. *Applied Mechanics Reviews* **63** (3), 30801.

Sirovich, L. 1991 Analysis of turbulent flows by means of the empirical eigenfunctions. *Fluid Dynamics Research* **8** (1-4), 85.

Smith, T. R., Moehlis, J. & Holmes, P. 2005 Low-dimensional modelling of turbulence using the proper orthogonal decomposition: a tutorial. *Nonlinear Dynamics* **41** (1-3), 275–307.

Strand, B. 1994 Summation by parts for finite difference approximations for d/dx. *Journal of Computational Physics* **110** (1), 47–67.

Suzuki, T., Colonius, T. & Pirozzoli, S. 2004 Vortex shedding in a two-dimensional diffuser: theory and simulation of separation control by periodic mass injection. *Journal of Fluid Mechanics* **520**, 187–213.

Svärd, M., Carpenter, M. & Nordström, J. 2007 A stable high-order finite difference scheme for the compressible Navier–Stokes equations, far-field boundary conditions. *Journal of Computational Physics* **225** (1), 1020–1038.

Svärd, M. & Nordström, J. 2008 A stable high-order finite difference scheme for the compressible Navier–Stokes equations: no-slip wall boundary conditions. *Journal of Computational Physics* **227** (10), 4805–4824.

Tam, C. & Burton, D. 1984 Sound generated by instability waves of supersonic flows. part 1. two-dimensional mixing layers. *Journal of Fluid Mechanics* **138**, 249–272.

Tam, C. & Morris, P. 1985 Tone excited jets, part v: A theoretical model and comparison with experiment. *Journal of Sound and Vibration* **102** (1), 119–151.

Tam, C. K. 1971 Directional acoustic radiation from a supersonic jet generated by shear layer instability. *Journal of Fluid Mechanics* **46** (4), 757–768.

Tam, C. K. & Chen, P. 1994 Turbulent mixing noise from supersonic jets. *AIAA Journal* **32** (9), 1774–1780.

Tam, C. K. & Hu, F. Q. 1989 On the three families of instability waves of high-speed jets. *Journal of Fluid Mechanics* **201**, 447–483.

Tennant, J. 1973 A subsonic diffuser with moving walls for boundary-layer control. *AIAA Journal* **11** (2), 240–242.

Tezuka, A. & Suzuki, K. 2006 Three-dimensional global linear stability analysis of flow around a spheroid. *AIAA journal* **44** (8), 1697–1708.

Theofilis, V. 2011 Global linear instability. *Annual Review of Fluid Mechanics* **43**, 319–352.

Troutt, T. & McLaughlin, D. 1982 Experiments on the flow and acoustic properties of a moderate-reynolds-number supersonic jet. *Journal of Fluid Mechanics* **116**, 123–156.

Vinokur, M. 1974 Conservation equations of gasdynamics in curvilinear coordinate systems. *Journal of Computational Physics* **14** (2), 105–125.

Vishnampet, R., Bodony, D. J. & Freund, J. B. 2015 A practical discrete-adjoint method for high-fidelity compressible turbulence simulations. *Journal of Computational Physics* **285**, 173–192.

Wang, M., Freund, J. B. & Lele, S. K. 2006 Computational prediction of flow-generated sound. *Annual Review of Fluid Mechanics* **38**, 483–512.

Wei, M. & Freund, J. B. 2006 A noise-controlled free shear flow. *Journal of Fluid Mechanics* **546**, 123–152.

Welsh, M. 1976 Flow control in wide-angled conical diffusers. *Journal of Fluids Engineering* **98**, 728.

Yen, C. & Messersmith, N. 1999 The use of compressible parabolized stability equations for prediction of jet instabilities and noise. *AIAA Paper* **1859**.

Zebib, A. 1987 Stability of viscous flow past a circular cylinder. *Journal of Engineering Mathematics* **21** (2), 155–165.